

Spring 2017

An Investigation into the Potential Benefits of Distributed Electric Propulsion on Small UAVS at Low Reynolds Numbers

Engin Baris
Old Dominion University

Follow this and additional works at: https://digitalcommons.odu.edu/mae_etds

 Part of the [Propulsion and Power Commons](#)

Recommended Citation

Baris, Engin. "An Investigation into the Potential Benefits of Distributed Electric Propulsion on Small UAVS at Low Reynolds Numbers" (2017). Master of Science (MS), thesis, Mechanical & Aerospace Engineering, Old Dominion University, DOI: 10.25777/t6qk-cr93
https://digitalcommons.odu.edu/mae_etds/24

This Thesis is brought to you for free and open access by the Mechanical & Aerospace Engineering at ODU Digital Commons. It has been accepted for inclusion in Mechanical & Aerospace Engineering Theses & Dissertations by an authorized administrator of ODU Digital Commons. For more information, please contact digitalcommons@odu.edu.

AN INVESTIGATION INTO THE POTENTIAL BENEFITS OF DISTRIBUTED
ELECTRIC PROPULSION ON SMALL UAVs AT LOW REYNOLDS NUMBERS

by

Engin Baris
B.S. June 2012, Sakarya University

A Thesis Submitted to the Faculty of
Old Dominion University in Partial Fulfillment of the
Requirements for the Degree of

MASTER OF SCIENCE

MECHANICAL AND AEROSPACE ENGINEERING

OLD DOMINION UNIVERSITY
May 2017

Approved by:

Drew Landman (Director)

Colin P. Britcher (Member)

Thomas A. Alberts (Member)

ABSTRACT

AN INVESTIGATION INTO THE POTENTIAL BENEFITS OF DISTRIBUTED ELECTRIC PROPULSION ON SMALL UAVs AT LOW REYNOLDS NUMBERS

Engin Baris
Old Dominion University, 2017
Director: Dr. Drew Landman

Distributed electric propulsion systems benefit from the inherent scale independence of electric propulsion. This property allows the designer to place multiple small electric motors along the wing of an aircraft instead of using a single or several internal combustion motors with gear boxes or other power train components. Aircraft operating at low Reynolds numbers are ideal candidates for benefiting from increased local flow velocities as provided by distributed propulsion systems.

In this study, a distributed electric propulsion system made up of eight motor/propellers was integrated into the leading edge of a small fixed wing-body model to investigate the expected improvements on the aerodynamics available to small UAVs operating at low Reynolds numbers. Wind tunnel tests featuring a Design of Experiments (DOE) methodology were used for aerodynamic characterization. Experiments were performed in four modes: all-propellers-on, wing-tip-propellers-alone-on, wing-alone mode, and two-inboard-propellers-on-alone mode. In addition, the all-propeller-on, wing-alone, and a single-tractor configuration were analyzed using VSPAERO, a vortex lattice code, to make comparisons between these different configurations. Results show that the distributed propulsion system has higher normal force, endurance, and range features, despite a potential weight penalty.

Copyright, 2017, by Engin Baris, All Rights Reserved.

This thesis is dedicated to my wife, who has always supported me.

ACKNOWLEDGEMENTS

There are many people who have contributed to the successful completion of this thesis. I would like to extend my gratitude to my advisor, Dr. Drew Landman, for providing invaluable guidance and endless support during the research. I also extend many thanks to my committee members, Dr. Colin Britcher and Dr. Thomas Alberts. I would also like to thank Brian Duvall and Omer Faruk Keskin. Finally, I am very thankful to the Turkish Military Academy for granting me this opportunity.

NOMENCLATURE

A	Axial Force
A-o-A	Angle of Attack
α_c	Corrected Angle of Attack
ANOVA	Analysis of Variance
β	Regression Coefficient
b	Regression Coefficient Vector
b_r	Systematic Standard Uncertainty
c	Wing Chord Length
C	Wind Tunnel Cross Sectional Area
C_A	Axial Force Coefficient
C_D	Drag Coefficient
C_{Du}	Uncorrected Drag Coefficient
C_{ij}	Diagonal Elements of Hat Matrix
C_L	Lift Coefficient
C_{Lw}	Wing Lift Coefficient
C_N	Normal Force Coefficient
C_T	Thrust Coefficient
CAD	Computer Aided Design
CCD	Central Composite Design
D	Drag Force
D_{prop}	Propeller Diameter
DOE	Design-of-Experiments

δ	Boundary Correction Factor
e	Residual
ESC	Electronic Speed Controller
$\epsilon_{sb,w}$	Wing Solid Blockage Correction Factor
$\epsilon_{sb,b}$	Body Solid Blockage Correction Factor
ϵ_{wb}	Wake Blockage Correction Factor
ϵ_T	Total Blockage Correction Factor
F_0	F-Test Statistic
FCD	Face-Centered Design
g	Acceleration due to Gravity (m/s^2)
H	Hat Matrix
H_0	Null Hypothesis
H_1	Alternate Hypothesis
η	Efficiency
J	Advance Ratio
k	Percent Charge of Batteries
K_1	Wing Shape Factor
K_3	Body shape Factor
L	Lift Force
L/D	Lift to Drag Ratio
L1	Left Motor 1
L2	Left Motor 2
L3	Left Motor 3

L4	Left Motor 4
m	Number of Factor Levels
MS	Mean Square
n	Sample Size
n_{prop}	Propeller revolution per second value
N	Normal Force
OFAT	One Factor at A Time
p	Number of Model Parameters
ΔP	Pressure Difference
P_{atm}	Atmospheric Pressure
PRESS	Prediction Error of Sum of Squares
q	Dynamic Pressure
q_A	Uncorrected Dynamic Pressure
q_c	Corrected Dynamic Pressure
R	Gas Constant of Air (J/kgK)
R^2	Coefficient of Determination
R^2_{adj}	Adjusted Coefficient of Determination
R^2_{pred}	Predicted Coefficient of Determination
Re	Reynolds Number
RPM	Revolutions Per Minute
RPS	Revolutions Per Second
RSM	Response Surface Methodology
R1	Right Motor 1

R2	Right Motor 2
R3	Right Motor 2
R4	Right Motor 4
ρ	Density (kg/m ³)
S _{ref}	Reference Wing Area
SS	Sum of Squares
s _r	Random Standard Uncertainty
σ^2	Error Variance
t	T-statistic
T	Temperature (K)
τ_1	Wind Tunnel Test Section Shape Factor
τ_3	Boundary Induced Up-wash Correction Factor
u	Battery Energy Density (J/m ³)
U _r	Overall Uncertainty
UAV	Unmanned Air Vehicle
V	Free Stream Velocity
V _A	Uncorrected Free Stream Velocity
V _c	Corrected Free Stream Velocity
VTOL	Vertical Take-Off or Landing
W	Total Model Weight
W _{bat}	Battery Weight
X	Model Matrix
x ₀	Design Point

y Response Matrix
 μ Dynamic Viscosity (kg/ms)

TABLE OF CONTENTS

	Page
LIST OF TABLES	xiii
LIST OF FIGURES	xv
Chapter	
1. INTRODUCTION	1
1.1 OVERVIEW	1
1.2 OBJECTIVE	2
1.3 PROBLEM STATEMENT	4
2. LITERATURE REVIEW	6
2.1 DISTRIBUTED PROPULSION DEFINITIONS AND CONCEPTS.....	6
2.2 EXPERIMENTAL STUDIES	14
3. EXPERIMENTAL SETUP AND DESIGN	16
3.1 WIND TUNNEL FACILITIES	16
3.2 MODEL DESIGN.....	17
3.3 MODEL BUILDING	21
3.4 FORCE BALANCE.....	25
3.5 MODEL SUPPORT AND DEVICES	26
3.6 TESTING PROCEDURE	28
3.7 MEASUREMENT UNCERTAINTIES.....	30
4. METHODOLOGY	35
4.1 OVERVIEW	35
4.2 TEST MATRIX DESIGN.....	36
5. ANALYSIS OF RESULTS	41
5.1 ANALYSIS OF VARIANCE (ANOVA).....	41
5.2 ALL-PROPELLERS-ON MODE.....	47
5.3 WING-ALONE MODE.....	61
5.4 WING-TIP-PROPELLERS-ALONE MODE.....	68
5.5 WING-TIP-PROPELLERS-ALONE AND TWO-INBOARD-PROPELLERS- ALONE COMPARISON.....	78
5.6 SINGLE-TRACTOR MODE.....	80

	Page
6. TRADE STUDY	84
7. CONCLUSIONS	91
REFERENCES	93
APPENDICES	98
A. MODEL ASSEMBLY TECHNICAL DRAWING	98
B. 2044A FORCE BALANCE SPECIFICATIONS	99
C. ALL-PROPELLERS-ON MODE ACTUAL TEXT MATRIX.....	100
D. WING-ALONE MODE ACTUAL TEXT MATRIX.....	103
E. WING-TIP-PROPELLERS-ALONE MODE ACTUAL TEXT MATRIX	104
F. WING-TIP-PROPELLERS-ALONE AND TWO-INBOARD-PROPELLERS- ALONE MODE ACTUAL TEXT MATRIX	106
G. WIND TUNNEL DATA BOUNDARY CORRECTIONS	107
VITA.....	109

LIST OF TABLES

Table	Page
1. Systematic uncertainties of velocity measurement components.....	31
2. Overall uncertainty of wind tunnel speed.....	32
3. Systematic uncertainties of balance measurement components.....	33
4. Overall uncertainty of force coefficients.....	34
5. Factors and factor limits for all-propellers-on mode.....	47
6. ANOVA for all-propellers-on C_N	48
7. Fit statistics for all-propellers-on C_N	48
8. Model term coefficients for all-propellers-on C_N	51
9. Prediction capability of the all-propellers-on C_N model.....	55
10. ANOVA for all-propellers-on C_A	56
11. Fit Statistics for all-propellers-on C_A	56
12. Model Term Coefficients for all-propellers-on C_A	58
13. Prediction capability of all-propellers-on C_A model.....	61
14. Factors and factor limits for wing-alone mode.....	61
15. ANOVA for wing-alone C_N	62
16. Fit statistics for wing-alone C_N	62
17. Model term coefficients for wing-alone C_N	64
18. Prediction capability of the wing-alone C_N model.....	65
19. ANOVA for wing-alone C_A	65
20. Fit Statistics for wing-alone C_A	65
21. Model term coefficients for wing-alone C_A	67

Table	Page
22. Prediction capability of the wing-alone C_A model	68
23. Factors and factor limits for wingtip-alone mode.....	68
24. ANOVA for wing-tip-propellers-alone C_N	69
25. Fit Statistics for wing-tip-propellers-alone C_N	69
26. Model term coefficients for wing-tip-propellers-alone C_N	71
27. Prediction capability of the wing-tip-propellers-alone C_N	73
28. ANOVA for wing-tip-propellers-alone C_A	74
29. Fit Statistics for wing-tip-propellers-alone C_A	74
30. Model term coefficients for wing-tip-propellers-alone C_A	76
31. Prediction capability of the wing-tip-propellers-alone C_A model.....	78
32. C_N increment for take-off.....	84
33. C_N increment for cruise.....	84
34. Distributed propulsion total weight	85
35. Single-tractor propulsion total weight	85
36. Overall efficiency.....	89

LIST OF FIGURES

Figure	Page
1. Electric propulsion from a marketing perspective	3
2. Cirrus SR22 and LEAPTech aircraft comparison.....	8
3. LEAPTech experimental testbed	8
4. Tecnam P2006T aircraft and SCEPTOR design.....	9
5. Existing aircraft and new design concepts.....	10
6. VTOL and cruise configurations of Joby S2	11
7. GL-10 50% scale aircraft with 10.5 ft wingspan	12
8. 20% subscale and full scale of LightningStrike.....	13
9. Schematic and prototype of PW-4	13
10. Load cell assembly.....	14
11. Cross flow fan tunnel set up and cross flow fan	15
12. Old Dominion University Low Speed Wind Tunnel	16
13. GWS 4.0 x 2.5 propeller	18
14. GWS 4.0 x 2.5 propeller thrust coefficient data	19
15. SD 7037 airfoil.....	20
16. SD 7037 airfoil XFOIL analysis results.....	20
17. Small UAV CAD model.....	21
18. Blue foam wing core, strut, rod and fiberglass	22
19. Vacuum process	22
20. Drilling of the motor holes.....	23
21. Motor mountings along the leading edge.....	23

Figure	Page
22. Bottom side of the wing (a) without motor mounting (b) with motor mounting.....	24
23. Fuselage and aluminum bulkhead before nose covering and sanding process.....	25
24. Small UAV model.....	25
25. Balance block diagram (Philips, 2016).....	26
26. Model and support system in test section	27
27. RPM recording setup	28
28. Reference angle (a) angle of attack (b) roll angle.....	29
29. A full factorial design for two factors.....	37
30. (a) CCD and (b) FCD for two factors	38
31. Nested FCD for two factors	39
32. One-half fraction of three factors (a) principle (b) alternate fraction	40
33. Motor name convention and symmetry	47
34. (a) Normality (b) Independence (c) Constant variance for all-propellers-on C_N	50
35. Response surface for all-propellers-on C_N at minimum RPM level	52
36. Response surface all-propellers-on C_N at maximum RPM level	52
37. C_N as a function of angle of attack and velocity for all-propellers-on mode.....	53
38. C_N as a function of angle of attack and L3 for all-propellers-on mode	54
39. C_N as a function of angle of attack and L4 for all-propellers-on mode	54
40. (a) Normality (b) Independence (c) Constant variance for all-propellers-on C_A	57
41. Response surface for all-propellers-on C_A at minimum RPM.....	59
42. Response surface for all-propellers-on C_A at maximum RPM	59
43. C_A as a function of velocity and L1 for all-propellers-on mode.....	60

44. (a) Normality (b) Independence (c) Constant variance for wing-alone C_N	63
45. Response surface for wing-alone C_N	64
46. (a) Normality (b) Independence (c) constant variance for wing-alone C_A	66
47. Response surface for wing-alone C_A	67
48. (a) Normality (b) Independence (c) Constant variance for wing-tip-propellers C_N	70
49. Response surface for wing-tip-propellers-alone C_N at minimum RPM	71
50. Response surface for wing-tip-propellers-alone C_N at maximum RPM	72
51. C_N as a function of velocity and angle of attack for wingtip-propellers-alone mode	73
52. (a) Normality (b) Independence (c) Constant variance for wing-tip-propellers C_A	75
53. Response surface for wing-tip-propellers-alone C_A at zero angle of attack	76
54. Response surface for wing-tip-propellers-alone C_A at eight angle of attack`	77
55. C_A as a function of velocity and L1 and R1 for wing-tip-propellers-alone mode	78
56. C_D vs C_L^2	79
57. Induced drag difference between two-inboard and wingtip propellers mode	80
58. VSPAERO models (a) distributed propulsion (b) wing-alone	81
59. Distributed propulsion VSPAERO and experimental results	81
60. Wing-alone VSPAERO and experimental results	82
61. VSPAERO single-tractor	83
62. Experimental and VSPAERO results for wing-alone and single-tractor	83
63. Weight effect on take-off configurations	86
64. Weight effect on cruise configurations	86
65. L/D Re = 76500	88
66. L/D Re = 86070	88

67. L/D Re = 95630	89
68. Range	90
69. Endurance	90

CHAPTER 1

INTRODUCTION

1.1 Overview

Recently, new aircraft propulsion concepts have been introduced in an effort to increase efficiency. General aviation, commercial aviation, and Unmanned Air Vehicles (UAV) may all benefit from these new technological developments. The primary aim of future aircraft designs is meeting environmental goals within desired flight conditions. Therefore, air transportation research mainly focuses on: new generation multidisciplinary propulsion technologies, noise reduction, reduced fuel consumption, safety and reliability, and optimized aircraft design. Distributed propulsion is one current trend in aviation that embodies the future focus.

The main idea behind distributed propulsion is dividing up thrust to multiple propulsive components for short take-off and landing, noise reduction, and reducing the energy consumption to increase flight range (Gohardani, Doulgeris, & Singh, 2011). Although this system has a historical background, it has not been preferred by designers until recent years because reciprocating or turbine engines were used for initial distributed propulsion system applications. These combustion-based engines were not practical, due to several disadvantages.

Scale dependency is the biggest disadvantage and arises from the complexity of structures such as gear boxes and other power train components. Additionally, when scaled to small sizes under certain conditions, power to weight ratio, efficiency, and reliability were reduced significantly (Moore & Fredericks, 2014). Noise pollution, high emission values, high maintenance costs, and power reduction at high altitudes are other problems to tackle for reciprocating and turbine engines. All of these disadvantages, plus recent advances in brushless

electric motor and battery design, have driven researchers to focus on distributed electric propulsion systems.

The marriage of distributed propulsion with electric propulsion opens a new era for aircraft design concepts. Electric motor structure scales without a significant loss of efficiency. Consequently, many small size electric motors can easily be put in required places on aircraft (Moore & Fredericks, 2014; Stoll, Bevirt, Moore, Fredericks, & Borer, 2014). Another significant advantage is the short response time to control commands which has an important contribution to safety and reliability. Additionally, decreased energy usage, noise reduction, ride quality, reduced operation costs, resulting reduced wing area, zero emissions, and high efficiency while changing altitudes and temperatures are all potential gains of distributed electric propulsion.

1.2 Objective

Despite the advantages of distributed electric propulsion, current battery technology restricts the application area of this system. Therefore, initial design implementations of electric propulsion technology will likely only be for general aviation aircraft and for unmanned air vehicles in the near future. Figure 1 shows the way ahead for electric propulsion, from a marketing perspective.

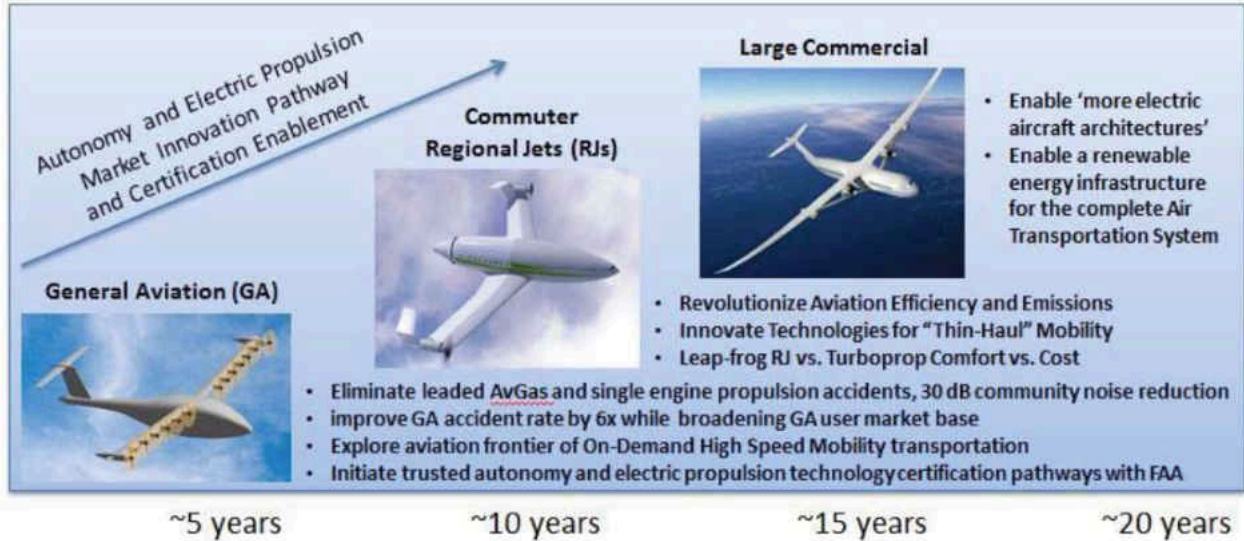


Figure 1. Electric propulsion from a marketing perspective (Moore et al., 2013)

Due to the short history of distributed electric propulsion systems, there are many facets left to investigate its benefits and effects on aviation. NASA Leading Edge Asynchronous Propellers Technology (LEAPTech) (Stoll, 2015), Joby S2 (Stoll, Bevirt, Pei, & Stilson, 2014), and NASA Greased Lightning – 10 (GL-10) (Rothhaar et al., 2014) aircraft are recent conceptual distributed electric propulsion aircraft flying prototypes for general aviation and unmanned air vehicle systems. However, they are still in the development phase.

Based on the progress provided above, the objective of this study is to explore the potential benefits of distributed propulsion on the aerodynamics of small unmanned air vehicles at low Reynolds numbers through wind tunnel tests using the Design of Experiments for aerodynamic characterization. In addition, comparison through analytical calculations and vortex lattice methods are performed.

1.3 Problem Statement

A fixed wing UAV wing-body model was considered for this study. A survey of existing UAVs and the constraints of available wind tunnel facilities drove the design and size of the model. Under these considerations, a wing was built with a 34-inch span and 5.5-inch chord length. This wing size and the availability of a 50 amp DC power supply drove the distributed propulsion concept to use eight motors and 4-inch diameter propellers along the leading edge of the wing. RPM values were chosen between 10000 and 13000 to avoid the windmill condition at free-stream velocities of 8-10 m/s. Additionally, a simple fuselage was built to provide a connection between the wing and force balance. The free-stream velocities give a chord-based Reynolds number range of 76500 to 95650, representative of small UAV operations.

Several configurations were chosen to investigate the effects on the measured normal force coefficient (C_N) and axial force coefficient (C_A):

- Powering all motors simultaneously, called *all-propellers-on*, was used to observe increased L/D due to reduction in tip vortices and increased momentum in the boundary layer
- The wing alone with no propulsion and props removed, called *wing-alone mode*, was used for baseline comparisons
- Wing tip props powered only, called *wingtip-propellers-alone-on*, for looking at the potential induced drag reduction while powering the UAV in cruise
- Two inboard props powered only, called *two-inboard-propellers-alone-on*, used for comparison to the *wingtip only* case.

Lastly, all-propeller-on, wing-alone, and an additional single-tractor configuration were analyzed using VSPAERO, a vortex lattice code, to make comparisons between these different

configurations. Thrust coefficient (C_T) equality was assumed for this comparison between a single tractor propeller and the distributed propulsion.

CHAPTER 2

LITERATURE REVIEW

2.1 Distributed Propulsion Definitions and Concepts

Making a specific definition of distributed propulsion systems with existing descriptions cannot be sufficient to cover all applications of this system, due to its wide range of configurations. However, some classification can be performed for general identification. Sehra and Whitlow (2004) tried to classify the distributed propulsion applications into three main categories: distributed engines, common core multi-fans, and distributed exhaust. Nevertheless, this definition does not include the required number of propulsion units to describe propulsion systems as a distributed propulsion system (Gohardani, 2013).

Another definition was published by the National Research Council (2006). This definition is based on simply using many distributed small electric thrusters, propulsors, or mini gas turbine engines, instead of large engines.

Ko's (2003) doctoral dissertation drew attention to NASA's distinction between the distributed propulsion and the distributed exhaust concepts. Replacing large engines with smaller engines implies distributed propulsion, and distributing the exhaust across a large area implies distributed exhaust applications. Therefore, four, six and eight engine design configurations were used in Ko's (2003) study to understand the benefits of distributed propulsion concepts.

Gohardani (2013) also mentioned the perception between distributed propulsion and the number of smaller engines. Still, there is a lack of consensus in the literature to explain distributed propulsion with an exact number of small propulsive units.

Distributed propulsion definition of Schetz, Hosder, Dippold, and Walker (2010) emphasized the distributed exhaust concept instead of mentioning a specific number of small engines. Schetz's research model redistributed the thrust along the thick trailing edges of the wing.

In light of these selected definitions, a propulsion concept can be divided into two main streams: a small number of larger engines replaced with a large number of smaller engines, and thrust redistribution across an area or space (Gohardani, 2013).

2.1.1 General Aviation Configurations

Although battery energy density is a barrier for fully electric aircraft, synergistic evaluation of total efficiency for aircraft and propulsion system coupling decreases the level of this disadvantage (Moore & Fredericks, 2014). A synergistic approach covers all system factor comparisons with each other, instead of considering a one-factor comparison between two concepts. For instance, noise reduction, low energy costs, zero emissions, high reliability and safety, high engine efficiency, and scale-free and improved aerodynamic efficiency characteristics are many advantages, despite the battery constraint. Current progress in battery technology illustrates that sufficient energy density may be available within five years for feasible general aircraft configurations, when based on historical battery progress (Moore & Fredericks, 2014). Therefore, recent research has started to focus on designing new electrical aircraft concepts to maximize aerodynamic and environmental benefits. Distributed electric propulsion designs will be considered within this context.

LEAPTech is a pioneer configuration for a distributed electric propulsion systems. It has eighteen small propellers placed along the span. These propellers increase the local dynamic

pressure over the wing during take-off and landing. This enables the aircraft to lower its stall speeds and use reduced wing area without the need for multi-element high-lift systems. Reduced wing area provides cruise drag reduction and improves ride quality. Additionally, the low tip speeds of the propellers reduce noise (Stoll, 2015). Figure 2 illustrates computer-based solid models of the LEAPTech configuration and Cirrus SR22, a current general aviation production aircraft. The experimental setup used to evaluate the LEAPTech concept is shown in Figure 3.

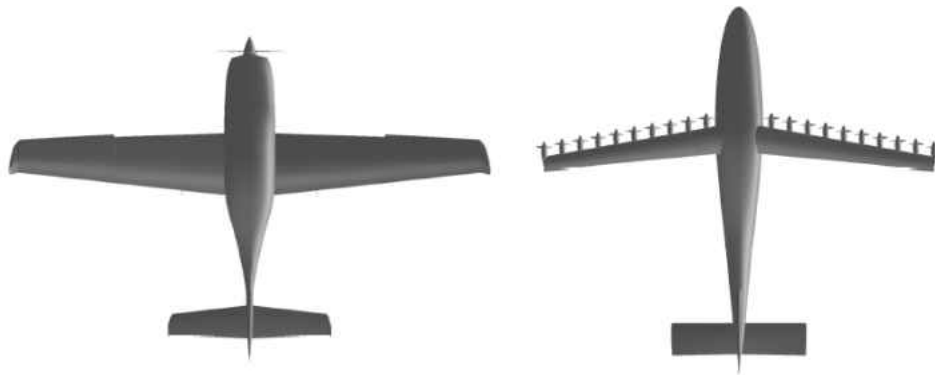


Figure 2. Cirrus SR22 and LEAPTech aircraft comparison (Stoll, 2015)



Figure 3. LEAPTech experimental testbed (Stoll, 2015)

The LEAPTech project created a foundation for NASA's Scalable Convergent Electric Propulsion Technology Operations Research (SCEPTOR) program (Borer et al., 2016). The goal

of the program is to design a fully electric distributed propulsion general aviation aircraft which shows up to fivefold predicted efficiency improvement in the cruise mode (Borer et al., 2016; Dubois et al., 2016). After evaluation of baseline airframe selection factors (e.g. useful load, installed power, effect of stock engines, wing, and fixtures removal on location of center of gravity etc.), the Tecnam P2006T model was selected to apply a distributed electric propulsion system to demonstrate purely the gains of this propulsion system approach (Borer et al., 2016). Tecnam P2006T aircraft and SCEPTOR Design are illustrated in Figure 4.



Figure 4. Tecnam P2006T aircraft and SCEPTOR design (Dubois et al., 2016; Moore et al., 2014)

SCEPTOR includes twelve small high-lift propellers and two larger wingtip propellers. The small high-lift propellers are used for flow acceleration over the wing (increased dynamic pressure) at take-off and landing. Wingtip propellers are the primary propulsors for the cruise mode. They benefit from the wingtip vortex and increase cruise efficiency, which means that less propulsive power is required for a given flight velocity (Borer et al., 2016).

Another distributed electric propulsion aircraft concept design study was conducted for the thin haul commercial aviation market (Stoll & Mikic, 2016). This class of aircraft has short route missions with around ten passengers (e.g. Cessna 402C, Tecnam P2012). Three different

configurations, including conventional, 3-motor and high-lift props, were considered to be optimized and then were compared with existing aircraft, as shown in Figure 5. In the designs, a battery was considered for short missions and range extenders for long missions. Computational results illustrated significant energy cost reduction again for distributed electric propulsion. However, the battery power to weight ratio still needed to be improved (Stoll & Mikic, 2016).

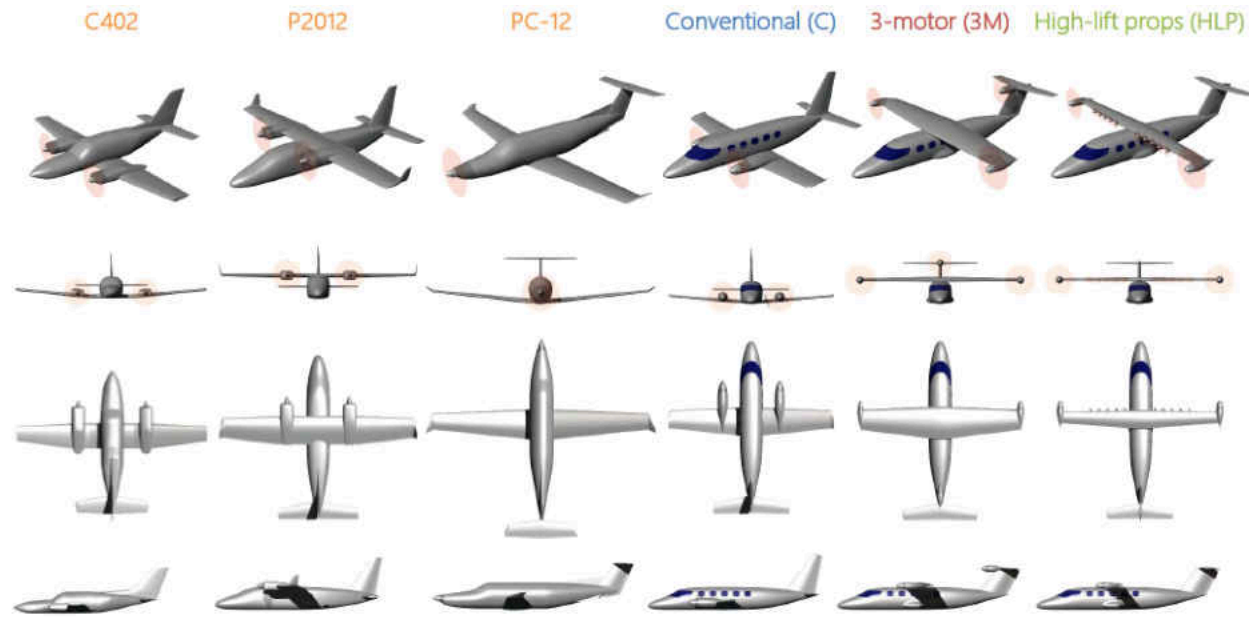


Figure 5. Existing aircraft and new design concepts (Stoll & Mikic, 2016)

The Joby S2 is a two-seat vertical take-off and landing application of distributed electric propulsion for personal air vehicles. This concept was designed for short to medium distances where speed, noise, efficiency, and safety are of concern. It has eight tilting motors along the wing and four tilting motors at the V-tail. These propellers are used during take-off and landing. A pair of the wingtip propellers are used for cruise mode. Other propellers are folded for drag reduction in cruise mode (Stoll et al., 2014). Figure 6 shows take-off, landing, and cruise mode configurations of the Joby S2 aircraft.

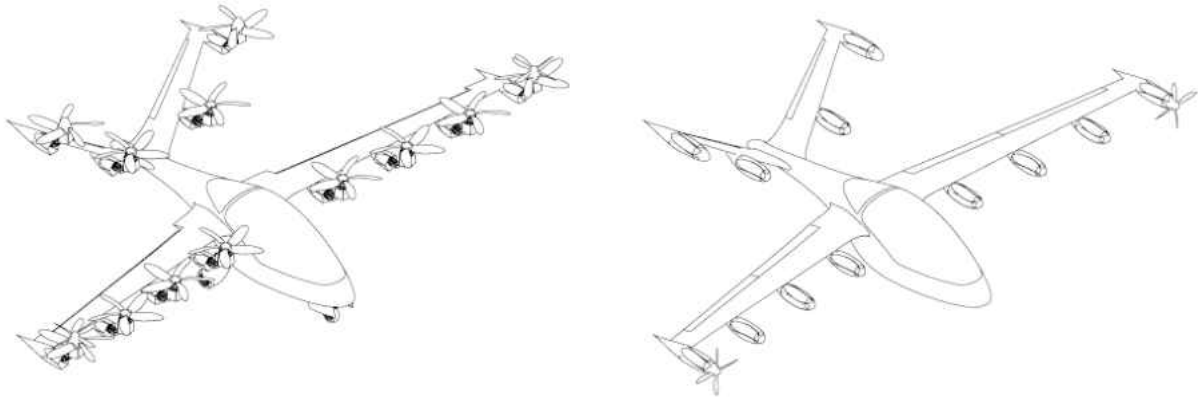


Figure 6. VTOL and cruise configurations of Joby S2 (Stoll et al., 2014)

2.1.2 Unmanned Air Vehicle Configurations

UAVs have become an indispensable necessity for aviation in recent years. They undertake important missions, such as search and rescue, fire control, reconnaissance, combat, aerial photography, and mapping. However, distributed electric propulsion technology has no widespread use in UAV applications at present. Gohardani (2013) demonstrated this conclusion with searching 624 UAVs in Jane's Unmanned Aerial Vehicle database ("Jane's All The World's Aircraft Homepage," 2016). Only 2.6% of the UAVs used distributed propulsion technology. Therefore, there is a large area of study to explore the effects of distributed propulsion systems on UAVs.

The UAV concept of distributed electric propulsion technology can be clearly seen on the GL-10 Greased Lightning long endurance VTOL aircraft. Foldable propellers were distributed throughout the wingspan. Tilt wing and tilt horizontal stabilizer were used, instead of the tilt motor employed on the Joby S2 aircraft. The concept is a combination of tilt wing aircraft and distributed electric propulsion. Therefore, flight control and flight test feasibility are the primary challenges, rather than the design of the aircraft configuration (Rothhaar et al., 2014).

Nevertheless, the flight control challenge was successfully completed in flight tests, which

showed transition from hover to wing-borne flight, and then back to hover again. After this success, research has been focused on a demonstration of the aerodynamic efficiency of this concept, which is four times more efficient in cruise than a helicopter (Barnstorff, 2015). New airframe design freedom was provided again by the scale-free advantage of electric motors.



Figure 7. GL-10 50% scale aircraft with 10.5 ft wingspan (Rothhaar et al., 2014)

Although VTOL aircraft have improved maneuverability, the speed of VTOL UAVs needs to improve, in order to become competitive with fixed wing configurations and because long mission times increase the vulnerability to enemy attack during military operations (Bagai, 2016). For this reason, the Defense Advanced Research Projects Agency (DARPA) signed a contract with Aurora Flight Sciences to enhance the top speed of VTOL UAV aircraft to 300kt – 400kt without increasing design complexity and reducing aerodynamic efficiency. In order to meet the requirements and to overcome the issues at hand, a distributed hybrid-electric propulsion system was selected by Aurora Flight Sciences. For the first phase of the project, they developed a 20% subscale vehicle model of the LightningStrike VTOL X-Plane. The model has distributed ducted fans along the tilt wing and canard (Sheller, 2016a). Flight tests were completed successfully with a subscale model. Therefore, the second phase of the project has

been started by the Aurora team to design a full scale unmanned LightningStrike. Figure 8 illustrates the subscale and the full scale design of LightningStrike.



Figure 8. 20% subscale and full scale of LightningStrike (Sheller, 2016a, 2016b)

The Propulsive Wing is an example of a distributed exhaust application of distributed propulsion systems (Kummer, 2010). A cross-flow fan was integrated along the trailing edge of a wing. This concept claims to improve the payload capacity three times, and the internal payload volume ten times, over the conventional systems for a given span. Additionally, propulsive wing aerial vehicles have shorter distances for take-off and landing (extreme high lift capability), low noise, and a high level of safety of user, due to the elimination of external rotational parts. The PW-4 unmanned prototype, which uses a distributed exhaust concept, is completed and the model is still in a flight test program at the time of this writing. Similarly, the cross-flow fan integration studies can be seen for commercial aircraft (Perry, Ansell, Kerho, Ananda, & D’Urso, 2016). A schematic of a propulsive wing and PW-4 prototype is shown in Figure 9.

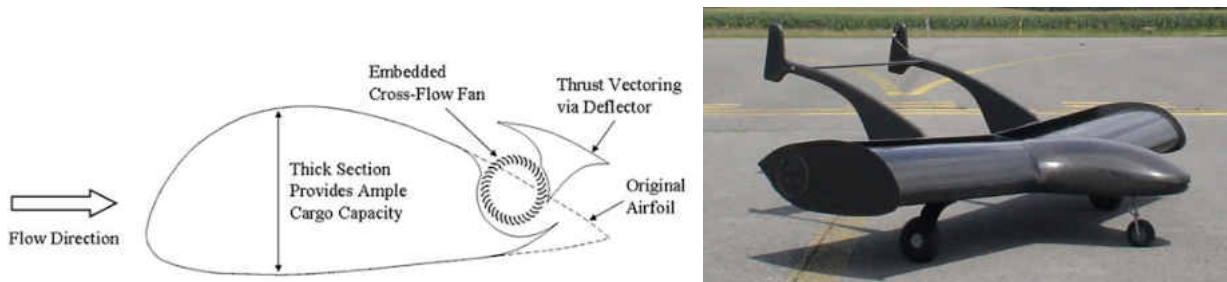


Figure 9. Schematic and prototype of PW-4 (Kummer, 2010)

2.2 Experimental Studies

Full scale LEAPTech experimental studies were performed on a specially modified truck testbed, as shown in Figure 3 (Stoll, 2015). Vertical force, axial force, side force, and pitching moment were measured by a custom force balance with seven load cells as depicted in Figure 10. The experimental data was compared to STAR-CCM+, FUND3D RUNS, and VSPAREO code solutions. Although distributed propulsion systems are a complex problem for computational studies, the computational aerodynamic performance results differed from experimental results by only approximately 10%. Also, the results and analytical predictions showed that the desired design $C_{L,max}$ value of 4.3 would be exceeded. This provides lower cruise drag and improved ride quality.

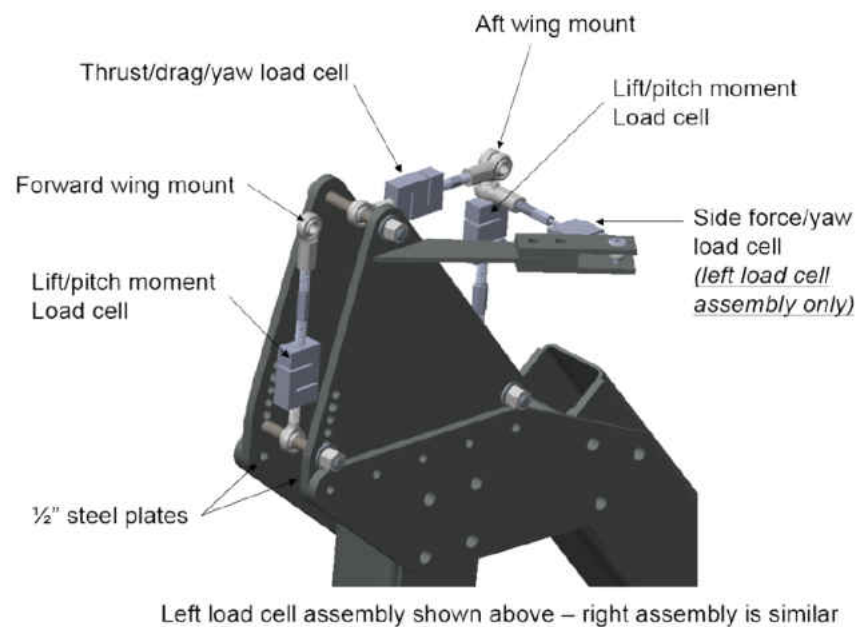


Figure 10. Load cell assembly (Stoll, 2015)

In a study by Murphy and Landman (2015), wind tunnel tests were conducted for the GL-10 unmanned air vehicle in the NASA Langley 12-Foot Low Speed Wind Tunnel. Design of

Experiments and Response Surface Methods were used to reduce test time and to get robust statistical regression models. Exploratory experiments were performed initially to understand the general characteristics of the aircraft. Other experiments were categorized in accordance with four modes of flight (cruise, loiter, transition and hover) for aerodynamic characterization of the GL-10. General regression models were created for all force and moment coefficients in all modes using up to 23 factors.

Transonic propulsive wing application of a distributed exhaust system underwent wind tunnel experiments at the University of Illinois in the 5x5 Supersonic Tunnel facility (Perry et al., 2016). The aim of the research was to design a new propulsive wing concept to meet the efficiency goals of the NASA generation N+3 aircraft. Trailing edge distributed cross-flow fans were used to provide suction/blowing for the airfoil as shown Figure 11. Experimental data illustrated that cross-flow fans could be effectively used for a transonic flow. Eventually, the propulsive wing concept was applied to the Boeing SUGAR (Subsonic Ultra Green Aircraft Research). Results show that 11.8% fuel reduction is achievable for this baseline aircraft with a propulsive wing.

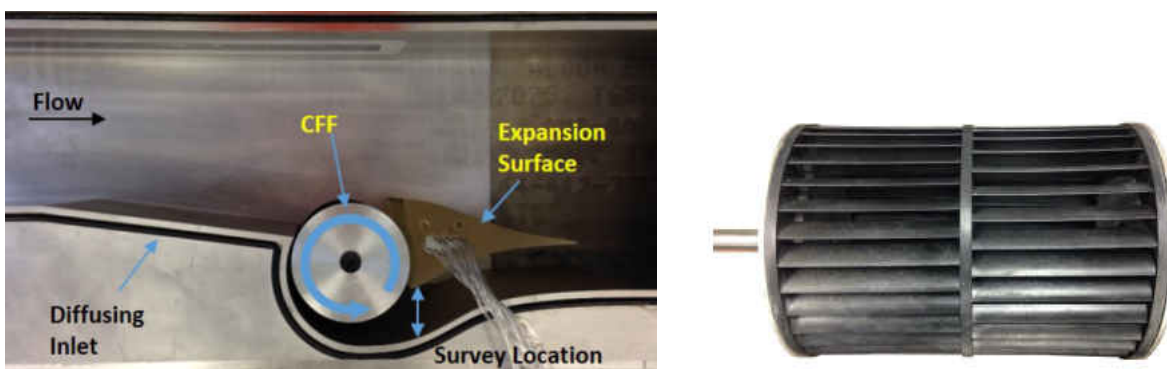


Figure 11. Cross flow fan tunnel set up and cross flow fan

CHAPTER 3

EXPERIMENTAL SETUP AND DESIGN

3.1 Wind Tunnel Facilities

The Old Dominion University Low-Speed Wind Tunnel (ODU LSWT) is an atmospheric closed return tunnel equipped with a 93 kW electric motor. The tunnel has high speed and low speed test sections measuring 0.91 x 1.22 meters and 2.13 x 2.44 meters respectively, as seen below in Figure 12. The high speed test section is 2.43 meters long and has a top speed of 55 m/s. The low speed test section is 2.13 meters long and has a top speed of 12 m/s. The tunnel and model positioning systems are computer controlled using LABVIEW software. Pressure probes, pressure transducers, multiple force balances, particle image velocimetry, and hot wire anemometry are other capabilities of the ODU LSWT.

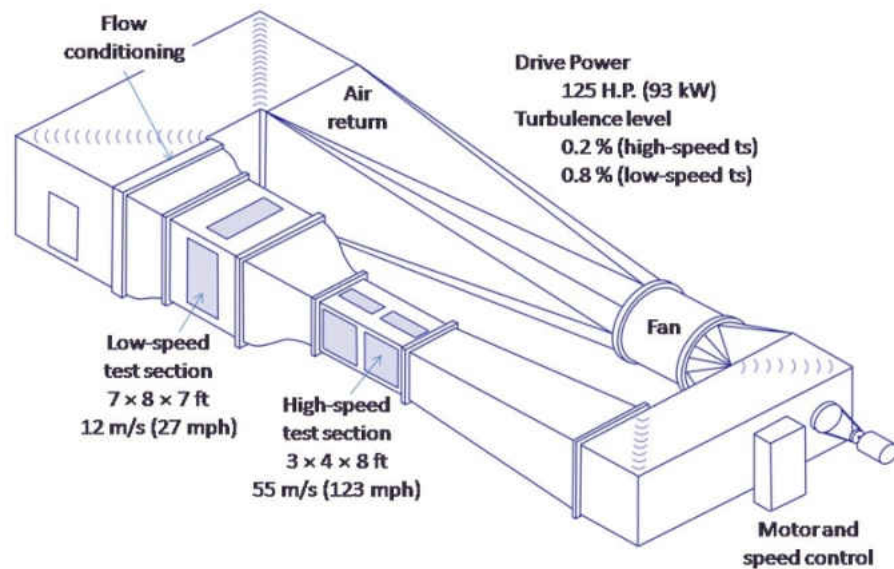


Figure 12. Old Dominion University Low Speed Wind Tunnel

3.2 Model Design

The design of the fixed wing UAV was based on existing UAVs, available power, and wind tunnel test facility limits. These limits were wing span limits due to boundary effects, force limits due to the balance, free stream speed limits, and propeller choices. The allowable maximum wing span for the wind tunnel test section was 38-inches (Barlow, Rae, & Pope, 1999). Therefore, a 34-inch wing span was determined for wind tunnel testing using available propellers. Balance force limits were considered for propeller and motor selection and determination of the model total weight. These balance moment center load limits were 70 lbs. for normal force and 15 lbs. for axial force. A detailed explanation of the force balance is given in an appendix.

An 8 propeller wing configuration was planned for the distributed propulsion system due to the wing span and power restriction. So, the maximum propeller diameter was chosen as 4 inches, when wingspan and propeller numbers were considered. Accordingly, a two blade GWS 4.0 x 2.5 propeller was selected from the University of Illinois at Champaign Urbana Propeller Data Base (Deters, Ananda, & Selig, 2014) as seen in Figure 17. The value of 4.0 indicates propeller diameter and 2.5 indicates propeller pitch. Also, a Medusa MR-012-030-4000 brushless motor was used for the tests due to size, power output, and historical wind tunnel test data with the GWS 4.0 x 2.5 propeller (Deters et al., 2014).

A 5.5-inch chord length was determined for appropriate installation of the brushless in-runner electric motors in the wing. Two types of motor mountings (nacelles) were designed for the wing-tip and inboard motor locations and were 3D printed from ABS material.

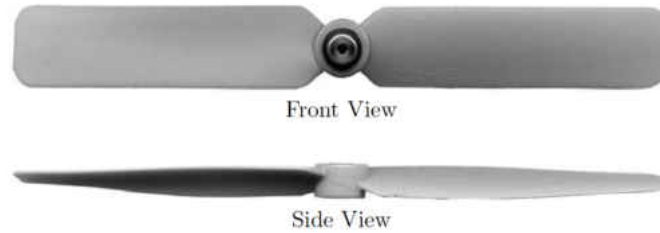


Figure 13. GWS 4.0 x 2.5 propeller (Deters & Selig, 2008)

RPM and wind tunnel free stream velocity ranges were defined from historical C_T and advance ratio (J) data of the GWS 4.0 x 2.5 propeller to avoid the windmill condition (Deters et al., 2014). The plot is shown in Figure 14 for various propeller chord based Reynolds numbers. Zero thrust coefficient determined the windmill case. Therefore, a 0.62 advance ratio value was chosen for calculations and equation (1) was used to calculate the maximum tunnel velocity. In equation (1), V is tunnel free stream velocity, n_{prop} is the RPS value, and D_{prop} is propeller diameter. The velocity range was identified between 8 m/s and 10 m/s. Also, RPM range was determined between 10000 and 13000. Additionally, the wing chord length based Re number range was computed between 76500 and 95650 by using equation (2). In equation (2) ρ is air density, μ is dynamic viscosity, c is wing chord length, and V is tunnel velocity.

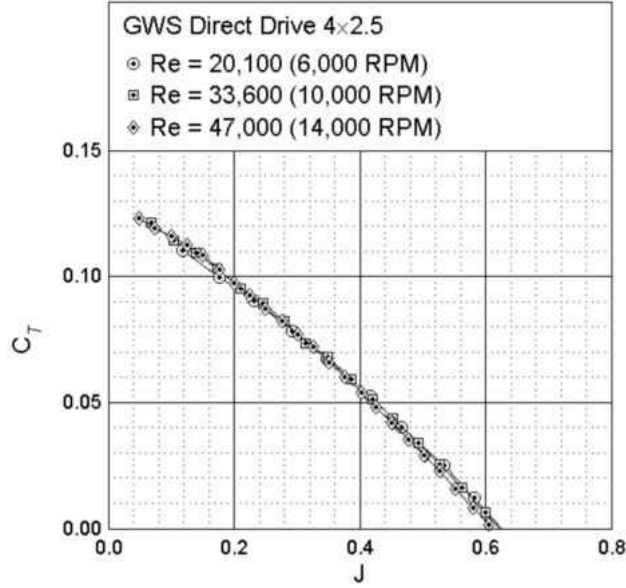


Figure 14. GWS 4.0 x 2.5 propeller thrust coefficient data (Deters et al., 2014)

$$J = \frac{V}{n_{prop} D_{prop}} \quad (1)$$

$$Re = \frac{\rho V c}{\mu} \quad (2)$$

The direction of the inboard propellers, which are clockwise and counter clockwise, were arranged in sequence based on wing tip-mounted propeller directions. The benefit of the leading edge mounted wing tip propellers is reducing induced drag when their rotation is opposite of the wing tip vortices (Miranda & Brennan, 1986). Therefore, outward rotating directions were chosen for wing tip propellers.

In keeping with the goal of representing a UAV operating at a low Reynolds number, a SD7037 airfoil was selected from the Low Speed Airfoil Data (Lyon, Broeren, Giguere,

Gopalarathnam, & Selig, 1997) library as representative. The SD7037 airfoil is shown in Figure 15. The boundary layer trips were not used.

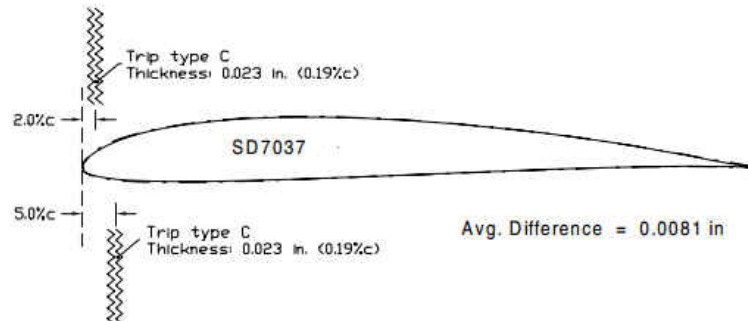


Figure 15. SD 7037 airfoil

The angle of attack range was chosen in a pre-stall region where the lift curve slope was relatively linear (Lyon et al., 1997). Hence, a 0–8 degree range was selected for angle of attack. Additionally, XFOIL analysis results for operating Reynolds numbers that are between 76000 and 96000 is shown below. The final assembled model CAD design is shown in Figure 17. Also, a detailed technical drawing of model assembly is given in the appendix.

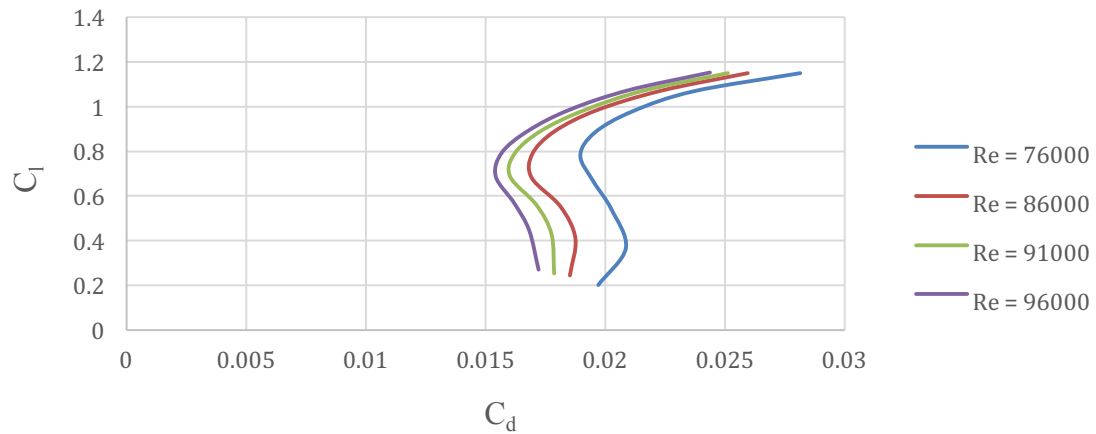


Figure 16. SD 7037 airfoil XFOIL analysis results

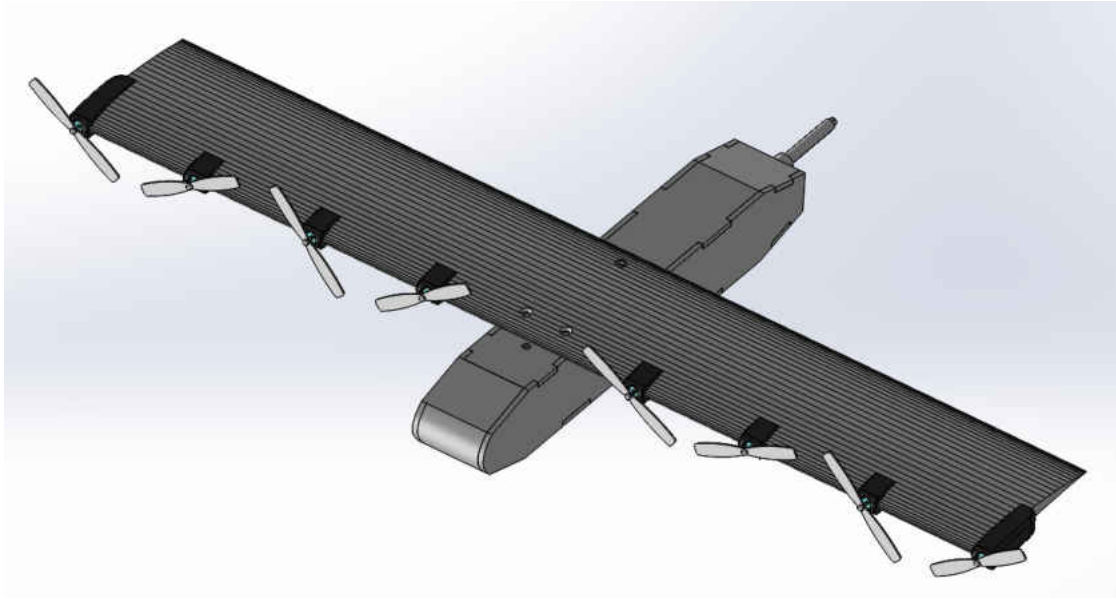


Figure 17. Small UAV CAD model

3.3 Model Building

The model utilized in the wind tunnel was hand fabricated in three manufacturing steps: wing building, simple fuselage building, and painting and final finish.

A hot wire cut blue foam core was used for wing construction. Also, a one-piece spruce spar was inserted into the wing along the wingspan and a thin carbon fiber strip was added to stiffen the trailing edge. The wing was next covered with fiberglass and resin as shown in Figure 18. West System 105 epoxy resin and West System 206 slow hardener were used for the covering operation.



Figure 18. Blue foam wing core, strut, rod and fiberglass

The fiberglass-covered wing was put in a vacuum bag and the vacuum pump provided 24 hours of equal pressure distribution along the wing for the epoxy curing process. Figure 19 illustrates this process.



Figure 19. Vacuum process

Afterwards, 8 equidistant motor mount holes were drilled throughout the leading edge. The vertical direction of the wing was adjusted with a spirit level, as seen in Figure 20.

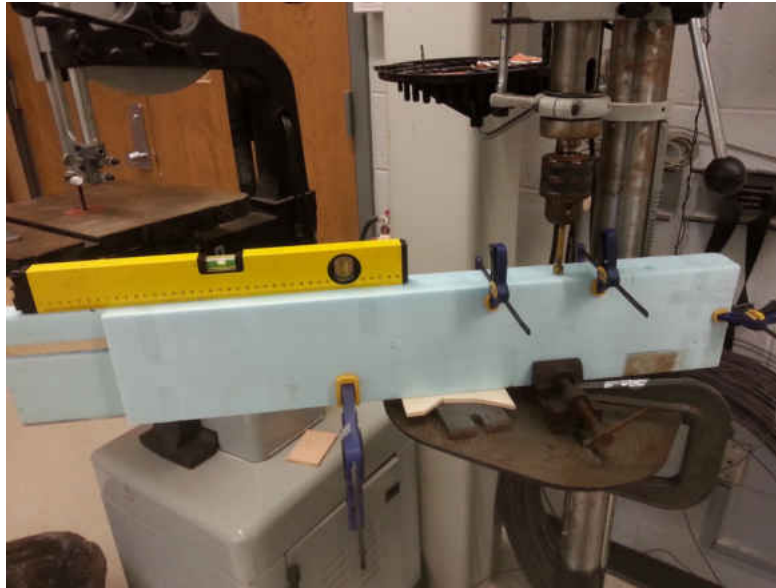


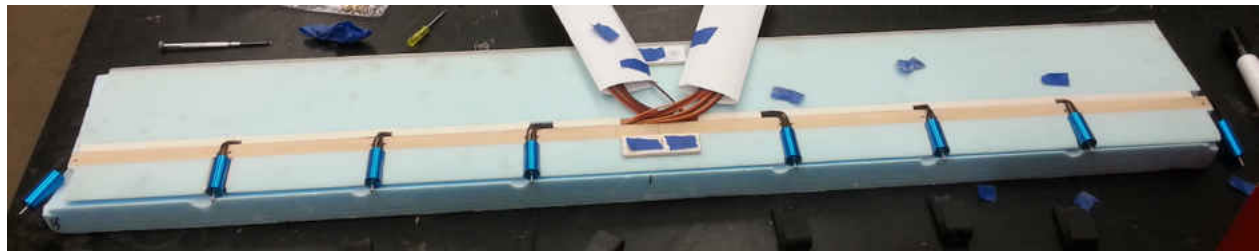
Figure 20. Drilling of the motor holes

Furthermore, eight motor mounts were produced with a 3D printing manufacturing technique from ABS material. These motor mounts were used to lock the motors in the leading edge holes, as shown in Figure 21.

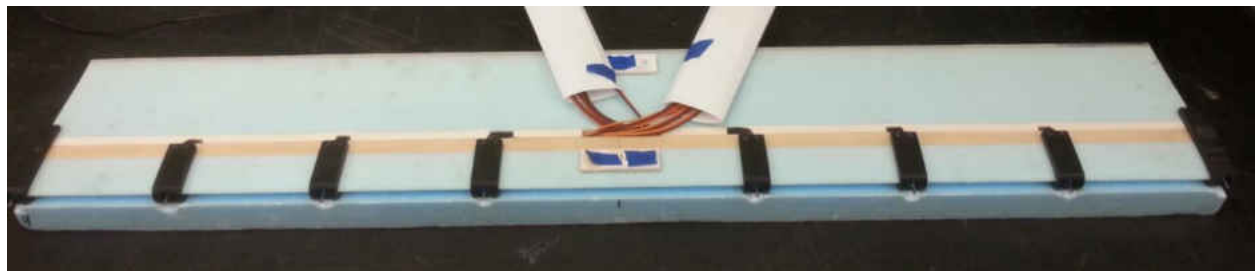


Figure 21. Motor mountings along the leading edge

Afterward, motors and motor mounts were assembled to the wing, which is illustrated in Figure 22.



(a)



(b)

Figure 22. Bottom side of the wing (a) without motor mounting (b) with motor mounting

A simple fuselage was built from plywood and balsa wood to provide an interface between the balance and wing. All parts were assembled using epoxy. The gaps between the parts were filled with body filler and the entire fuselage was sanded smooth. The wing was attached to the fuselage with three screws. An aluminum machine bulkhead was placed in the fuselage to support the metric end of the balance. The fuselage and bulkhead are shown in Figure 23.



Figure 23. Fuselage and aluminum bulkhead before nose covering and sanding process

Finally, the wing, fuselage, and motor mounts were painted with filler and sandable primer. The wing was coated and sanded four times until it met the desired roughness. The painted and assembled small UAV model is illustrated in Figure 24.



Figure 24. Small UAV model

3.4 Force Balance

A NASA 2044a force balance was used for wind tunnel testing. It is a 6 degree of freedom strain gage based internal balance. The metric end of the balance was inserted into the model aluminum bulkhead and was fixed by a dowel pin from the top of the fuselage. The moment center of the balance was placed at the quarter chord of the wing. The balance block

diagram between electrical connections and National Instruments data acquisition system components is shown in Figure 25 (Philips, 2016). To reduce the electrical noise on the balance signal lines, low pass filters were installed on each channel. The balance force and moment ranges and other specifications are given in the appendix.

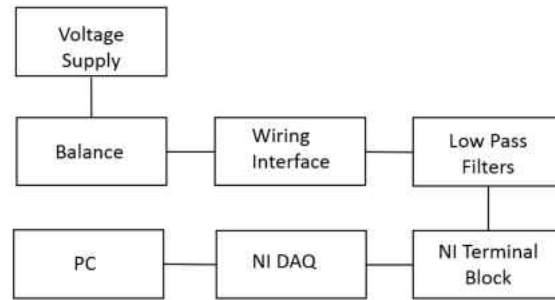


Figure 25. Balance block diagram (Philips, 2016)

3.5 Model Support and Devices

An existing twin lead screw model support system was used for wind tunnel testing. This system has full automation, remote pitch, and roll control capabilities. The model pitch position was adjusted with two sliders on lead screws. This slide positioning system kept the model on the tunnel centerline while pitching. The roll position was held constant for this study. The angle of attack adjustment and measurements were done by a high precision inclinometer. The picture of the overall assembly for the twin lead screw model support system is shown in Figure 26.

H-KING 10A electronic speed controllers were used for each Medusa MR-012-030-4000 brushless motor. To set the rotational speed of the motors, the speed controllers were connected to a Pololu Mini Maestro 12 Channel USB Servo Controller board. This servo controller has individual speed and acceleration control for each channel. The ESCs and servo controller were placed outside of the test section.

Propeller RPM measurements were recorded with a Hangar-9 micro digital tachometer. An LED light source was used, opposite the side of the optical tachometer, to read the correct RPM value. The tachometer was attached on the wing for motor calibration. This setup is illustrated in Figure 27.



Figure 26. Model and support system in test section

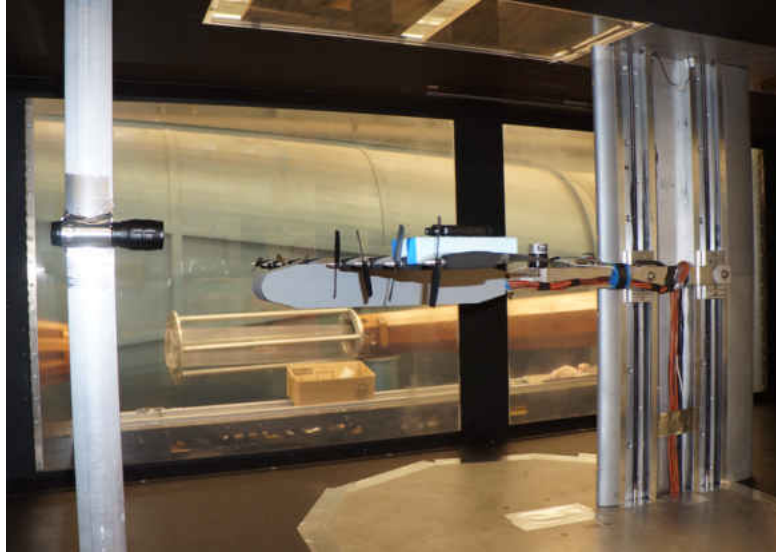


Figure 27. RPM recording setup

3.6 Testing Procedure

To reach thermal equilibrium for stable measurements, the balance and all the other electronic equipment were powered for at least 8 hours before beginning testing (Philips, 2016). The adjustment of the reference zero-degree angle of attack and zero degree roll angle were done by spirit level, as illustrated in Figure 28. Then, zero reference slide positions were saved.

An existing LabVIEW software program was used to control the model support and wind tunnel and to monitor the balance (Philips, 2016). The motor speed control was the only addition to the LabVIEW software.

A tare was taken before beginning testing for each case (all-propellers on, wing-alone, wing-tip propellers-alone etc.). The test matrix had tunnel velocity, angle of attack, and propeller RPM factors. Also, a randomized test matrix was created using design of experiments methodology, which is discussed in detail in Chapter 4. The tests were begun with the tunnel starting. As soon as tunnel velocity reached the desired condition, the angle of attack adjustment

was done by the twin lead screw mechanism, and the motors were run with determined RPM levels. When these three factor values matched the test matrix values, the data was taken over a 15 second sample time. After data recording, the model was sent to zero angle of attack and zero RPM level. This process was repeated over the entire test matrix.



(a)



(b)

Figure 28. Reference angle (a) angle of attack (b) roll angle

3.7 Measurement Uncertainties

Experimental measurements include uncertainties in both the input variables and responses. Generally, uncertainty has two types of error sources, called systematic standard uncertainties and random standard uncertainties (Coleman & Steele, 2009). Instrument accuracy in the form of a bias is accounted for using the systematic standard uncertainties. Random standard uncertainties are related to standard errors of the measured responses (results). In general, where the result r is a function of several variables,

$$r = r(X_1, X_2, \dots, X_j) \quad (3)$$

combined standard uncertainty (u_r) is defined by (Coleman & Steele, 2009),

$$u_r = (b_r^2 + s_r^2)^{1/2} \quad (4)$$

With the Taylor Series Method, where the systematic standard uncertainty of the result, b_r is defined by,

$$b_r^2 = \left(\frac{\partial r}{\partial X_1}\right)^2 b_{X_1}^2 + \left(\frac{\partial r}{\partial X_2}\right)^2 b_{X_2}^2 + \dots + \left(\frac{\partial r}{\partial X_j}\right)^2 b_{X_j}^2 + \dots + 2\left(\frac{\partial r}{\partial X_i}\right)\left(\frac{\partial r}{\partial X_k}\right) b_{X_i} b_{X_k} + \dots \quad (5)$$

and the random standard uncertainty of the result, s_r is defined by,

$$s_r^2 = \frac{S^2}{n} \quad (6)$$

The error distribution of r usually shows a Gaussian distribution (supported by the Central Limit Theorem) which allows use of the t distribution to obtain a confidence level for the overall uncertainty, as seen in equation 7.

$$U_r = t_{\%} u_r \quad (7)$$

where the $\pm U_r$ band around r will include the true value of result for the chosen level of confidence. Most engineering and scientific applications consider $t=2$ for an approximate 95%

confidence level and assume there are no correlated random errors³¹. Therefore, equation (7) is redefined by,

$$U_{95} = 2(b_r^2 + s_r^2)^{1/2} \quad (8)$$

3.7.1 Wind Tunnel Velocity Uncertainty Analysis

The Taylor Series approach to uncertainty propagation was applied to assess the uncertainty associated with wind tunnel velocity measurements. Wind tunnel velocity is a function of the static pressure differential, atmospheric pressure and fluid temperature, as seen in equation (9). Related derivatives for uncertainty analysis are given in equations (10)-(12).

$$V = \sqrt{\frac{2\Delta P}{\frac{P_{atm}}{RT}}} \quad (9)$$

$$\frac{\partial V}{\partial \Delta P} = \frac{\sqrt{2}}{2} \frac{RT}{\sqrt{\Delta P R T P_{atm}}} \quad (10)$$

$$\frac{\partial V}{\partial P_{atm}} = -\frac{\sqrt{2}}{2} \frac{\Delta P R T}{\sqrt{\Delta P R T P_{atm}^3}} \quad (11)$$

$$\frac{\partial V}{\partial T} = \frac{\sqrt{2}}{2} \frac{\Delta P R}{\sqrt{\Delta P R T P_{atm}}} \quad (12)$$

The systematic uncertainties of each measurement variable are given in Table 1.

Component	Uncertainty
Differential Pressure	±0.01% Full Scale
Temperature	±0.1 deg. C
Barometric Pressure	±0.01% of Reading

Table 1. Systematic uncertainties of velocity measurement components

The random uncertainty component for velocity was calculated using the standard error from replicated measurements of velocity. For this study, overall uncertainty in the estimations of wind tunnel velocities for nominal wind tunnel speeds of 9 m/s, atmospheric pressure of 101506 Pa, and tunnel fluid temperature of 294K were calculated and are shown in Table 2.

Component	Calculated Value
9 m/s	
s_r	± 0.0111 m/s
b_r	± 0.0346 m/s
U_{95}	± 0.0727 m/s

Table 2. Overall uncertainty of wind tunnel speed

3.7.2 Normal and Axial Force Coefficients Uncertainty Analysis

The normal force coefficient is a function of normal force and static differential pressure (dynamic pressure), as seen equation (13). Applying the Taylor Series approach, related derivatives for uncertainty analysis are given in (14)-(15).

$$C_N = \frac{N}{\frac{1}{2} \rho V^2 S_{ref}} = \frac{N}{\frac{1}{2} \frac{P_{atm}}{RT} \frac{2\Delta P}{P_{atm}} S_{ref}} = \frac{N}{\Delta P S_{ref}} \quad (13)$$

$$\frac{\partial C_N}{\partial N} = \frac{1}{\Delta P S_{ref}} \quad (14)$$

$$\frac{\partial C_N}{\partial \Delta P} = -\frac{N}{\Delta P^2 S_{ref}} \quad (15)$$

Axial force coefficient is function of axial force and static differential pressure as seen in equation (16). Applying the Taylor Series approach, related derivatives for uncertainty analysis are given in (17)-(18).

$$C_A = \frac{A}{\frac{1}{2} \rho V^2 S_{ref}} = \frac{A}{\frac{1}{2} \frac{P_{atm}}{RT} \frac{2\Delta P}{P_{atm}} S_{ref}} = \frac{A}{\Delta P S_{ref}} \quad (16)$$

$$\frac{\partial C_A}{\partial A} = \frac{1}{\Delta P S_{ref}} \quad (17)$$

$$\frac{\partial C_A}{\partial \Delta P} = -\frac{A}{\Delta P^2 S_{ref}} \quad (18)$$

The uncertainties of each measurement variable are given in Table 3.

Component	Uncertainty
Balance Normal Force	±0.05%
Balance Axial Force	±0.10%

Table 3. Systematic uncertainties of balance measurement components

For this study, overall uncertainty for nominal normal force of 3.832 N and nominal axial force of -1.641 N are shown in Table 4, which is based on the nominal tunnel speed of 9 m/s, atmospheric pressure of 101506 Pa and wing reference area of 0.120 m².

Component	Calculated Value
$C_N = 0.6549$	
s_r	± 0.0006
b_r	± 0.00007
U_{95}	± 0.0012
$C_A = -0.2806$	
s_r	± 0.0003
b_r	± 0.0002
U_{95}	± 0.00007

Table 4. Overall uncertainty of force coefficients

CHAPTER 4

METHODOLOGY

4.1 Overview

Design of experiments (DOE) methodology was used in this study even though one factor at a time (OFAT) was the traditional testing approach. OFAT testing allows only one factor to change while all other factors remain unchanged. Error sources (system errors and precision errors) cannot be separated from each other, and significant contributions of factor interaction terms (simultaneous factor changes cause interaction terms) on the response cannot be reliably determined with regression models; only main factor effects can be readily characterized. Due to these disadvantages of the OFAT procedure, the aerospace community has started to use DOE methodology in recent years.

The origin of the DOE methodology came from the study field of agriculture, with the work of Ronald A. Fisher (1935). The methodology was expanded to response surface methodology (RSM) by Box and Wilson (1951) for industrial applications in 1950s. Recently, computer programs have been developed for DOE and RSM; these make it simple to analyze complex designs. The goal of the DOE methodology is to create statistically rigorous regression models that predict the response with minimized prediction error. In other words, it determines the effect of input factors on process and response with their simultaneous changes. DOE has three main principles for experimental design: randomization, replication, and blocking (Montgomery, 2013).

Randomization is the cornerstone of the statistical methods and it applies to both run order and experimental factor level choices. It also assists in averaging out the unknown and

uncontrolled extraneous factor effects. The randomization is supplied by using computer based random number generators.

Randomized, repeated runs of factor combinations are defined as replication. These allow the researcher to obtain an estimate of pure systematic experimental noise, independent from model fitting.

Blocking is an experiment design technique used to improve the precision with which comparisons among the factors of interest are made. Blocking reduces or eliminates the variability transmitted from known but uncontrollable nuisance factors, that is, factors that may influence the experimental response but are not directly of interest to the experiment.

In addition, orthogonality is addressed along with these three main DOE principles (Myers, Montgomery, & Anderson-Cook, 2009). Orthogonality in an experimental design is one that minimizes the variances and uncorrelated orthogonal regressors to improve the parameter estimates.

RSM is a subset of DOE. It is a useful combination of statistical and mathematical techniques for process development, improvement, and optimization. In general, RSM is classified into three main categories in industrial experimentation: mapping a response surface over a particular region of interest, optimization of the responses, and selection of the operating conditions to achieve specifications or customer requirements (Myers et al., 2009).

4.2 Test Matrix Design

The fundamental classical experiment design in DOE is the 2-level factorial design. A factorial design allows all factor levels to be changed simultaneously for all possible combinations. Each factor has two levels (high and low limits). A first order plus interaction

regression model can be developed with a factorial design. A full factorial design with center points for two factors is shown below in Figure 29. The center points provide a means to test for the need for quadratic model terms. Also, pure error calculation and scaled prediction variance reduction is afforded by center point replicates in DOE/RSM. The regression model representation of the factorial experiment with main effects and two factor interactions is shown in equation (19).

$$y = B_0 + \sum_i B_i x_i + \sum_{i \neq j} B_{ij} x_i x_j + \dots + \varepsilon \quad i = 1, 2, \dots, k \quad (19)$$

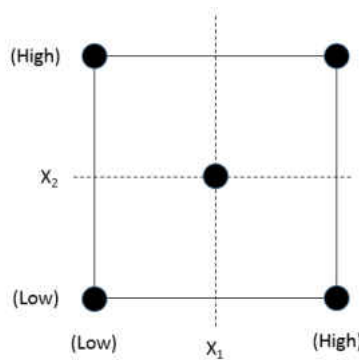


Figure 29. A full factorial design for two factors

y is the response, B's are the fitted regression coefficients, x's are independent variables (factors) and the ε is a random error term. This first order model can represent some mild curvature in the response function through the interaction terms. However, pure second order terms (quadratic effects) are usually required for curvature representation in the response function particularly for aircraft aerodynamic characterization. Therefore, a second order response surface model must be considered, as seen in equation (20).

$$y = B_0 + \sum_i B_i x_i + \sum_i B_{ii} x_i^2 + \sum_{i \neq j} B_{ij} x_i x_j + \varepsilon \quad i = 1, 2, \dots, k \quad (20)$$

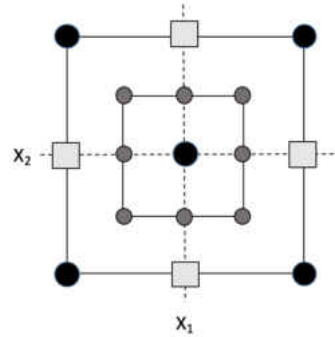


Figure 31. Nested FCD for two factors

Also, these designs can be fractionated if the experimenter can make some logical assumptions about omitting high order interaction terms (Montgomery, 2013). This reduces run numbers in the experiment. The one-half fraction factorial design and the alternate fraction of three factors (a, b, c) are illustrated in Figure 32.

In this experimental study, a full nested FCD response surface method with center points was selected for the wing-alone and wing-tip-propellers-alone-on configurations. A fractionated (minimum-run Resolution V) nested FCD design with center points was selected for the all-propellers-on configuration. Resolution is a degree measurement of confounded or aliased regression terms. Main effects or two factor interactions are not aliased with any other main effects or two factor interactions in resolution V design, meaning they may be uniquely estimated (Myers et al., 2009).

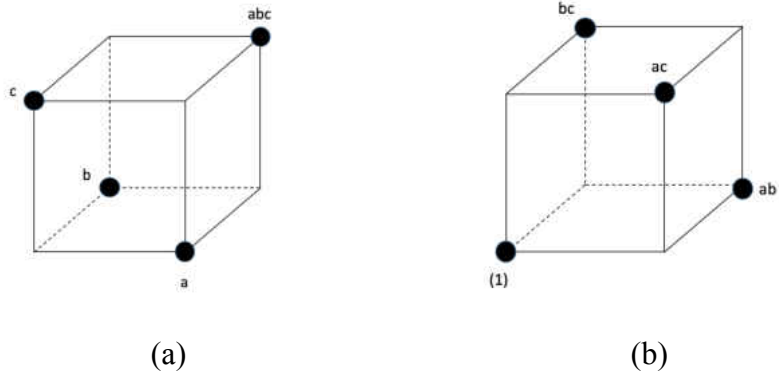


Figure 32. One-half fraction of three factors (a) principle (b) alternate fraction

Actual test matrix designs are shown in the Appendix for all configurations.

CHAPTER 5

ANALYSIS OF RESULTS

5.1 Analysis of Variance (ANOVA)

In this study, the test matrix design and collected data analysis were accomplished with the help of Design Expert™ software. ANOVA is used to evaluate regression model term significance and error. Generally, a multiple linear regression model is used to fit a response surface as illustrated in equation (20) in Section 4.2 and the ordinary least squares fitting method is used to estimate the regression coefficients in the model (Myers et al., 2009). Therefore, the model can be written in matrix notation as seen in equation (21),

$$y = X\beta + \varepsilon \quad (21)$$

where y is an $n \times 1$ vector of observations, X is an $n \times p$ model matrix, β is a $p \times 1$ vector of the regression coefficients, and ε is an $n \times 1$ vector of random errors. Then, the least square estimator of regression coefficients (β) is calculated, as shown in equation (22), to develop the regression model (Myers et al., 2009).

$$\beta = (X'X)^{-1} X'y \quad (22)$$

Hence, the fitted regression model becomes:

$$\hat{y} = X\beta + \varepsilon \quad (23)$$

If there is a linear relationship between the response variable and a subset of the regressor variables, then the model is significant (Myers et al., 2009). An ANOVA determines this relationship with hypothesis testing as seen below.

$$H_0 = \beta_1 = \beta_2 = \dots = \beta_k = 0$$

$$H_1 = \beta_j \neq 0 \text{ for at least one } j \quad (24)$$

The rejected null hypothesis implies that at least one of the regressor variables contributes significantly to the model. This test procedure starts by noting the relationship of the total variability (sum of squares) to that explained by the model and that due to error (25).

$$SS_T = SS_R + SS_E \quad (25)$$

SS_T is a total sum of squares which represents total variability in the observations, SS_R is a regression sum of squares which represents variability related to the regression model and SS_E is an error sum of squares which represents variability related to the residual error (Montgomery, 2013). The formulas for calculating these terms are illustrated in the equations below and are found in any regression text:

$$SS_T = y'y - \frac{\left(\sum_{i=1}^n y_i\right)^2}{n} \quad (26)$$

$$SS_R = b'X'y - \frac{\left(\sum_{i=1}^n y_i\right)^2}{n} \quad (27)$$

$$SS_E = y'y - b'X'y \quad (28)$$

Then, overall variance can be estimated by calculating mean square values in equations (29) and (30) (Montgomery, 2013).

$$MS_E = \frac{SS_E}{n - k - p} \quad (29)$$

$$MS_R = \frac{SS_R}{k} \quad (30)$$

In equations (30) and (31), n is the total number of observations, k is the total number of regression variables included in the model, and p is the number of parameters. The mean squares are variance quantities. Finally, the acceptance or rejection of the null hypothesis is determined using the F_0 test statistic for equality of variances, as shown in equation (31).

$$F_0 = \frac{MS_R}{MS_E} \quad (31)$$

To reject the null hypothesis (model is significant), F_0 must be greater than $F_{\alpha, k, n-k-1}$ (F_{critical}). The α is a determined significance level where $1 - \alpha$ is the desired confidence. Although the F test provides information about the significance of the overall model, it cannot give any knowledge about the significant level of any given term. Therefore, each term in the model is tested individually versus error.

Furthermore, the SS_E term is composed of two terms: lack of fit (SS_{LOF}) and pure error (SS_{PE}). Lack of fit implies how well the regression model fits the experimental observations and pure error quantifies the error in repeated experimental measurements.

$$SS_{LOF} = SS_E + SS_{PE} \quad (32)$$

Mean squares are calculated for lack of fit testing, as seen in equation (33) and (34),

$$MS_{LOF} = \frac{SS_{LOF}}{(m - p)} \quad (33)$$

$$MS_{PE} = \frac{SS_{PE}}{(n - m)} \quad (34)$$

where $m-p$ is degrees of freedom for SS_{LOF} , p is the number of model parameters, and there are $n-m$ degrees of freedom for SS_{PE} . Detailed calculations can be seen in Myers et al. (2009).

Similarly, the F_0 test statistic is applied for lack of fit testing, as shown in equation (35).

$$F_0 = \frac{MS_{LOF}}{MS_{PE}} \quad (35)$$

If F_0 is greater than $F_{\alpha, m-p, n-m}$, then lack of fit is significant. In general, this is not a desired situation. However, in some cases where noise levels are very low (wind tunnel testing), lack of fit can be significant while the model is significant and fit is acceptable. Thus, another family of fit statistics (R^2 family) must be considered to draw a complete conclusion about the goodness of the fit.

Residual diagnostics are used to determine the validation of error distribution assumptions: normality, independence, and constant variance (Montgomery, 2013). The residuals (e) are the difference between the measured response (y) and the predicted response (\hat{y}).

$$e = y - \hat{y} \quad (36)$$

A normal probability plot of residuals is used for checking the normality assumption. If the residuals resemble a straight line, the normality assumption is valid. In addition, a plot of residuals in time sequence is used for verifying the independence assumption. If the residuals have a structureless distribution, the independence assumption is valid. Lastly, plotting the residuals versus fitted values and factor levels for the constant variance assumption is checked. If the residuals are bounded and have no cone or barrel shape, the constant variance assumption is verified³⁵.

The R^2 family (R^2 , R^2_{adj} , R^2_{pred}) allows an assessment of the model quality. R^2 represents the total variability in the response that is explained by the model (Montgomery, 2013). The R^2 value range is between zero and one (100%). In general, 95% or greater values of R^2 are desired for wind tunnel experimentation. However, this statistic always increases when either significant

or insignificant terms are added to model. Thus, the R^2_{adj} statistic can be considered for better estimation of the model's variability explanation related with observed response because the R^2_{adj} value decreases when insignificant terms are added to the regression model (Montgomery, 2013). The computation of these statistics is shown in equations (37) and (38).

$$R^2 = \frac{SS_R}{SS_T} = 1 - \frac{SS_E}{SS_T} \quad (37)$$

$$R^2_{adj} = 1 - \frac{n-1}{n-p} (1 - R^2) \quad (38)$$

In addition to the model fit statistics above, a prediction error sum of squares (PRESS) and R^2_{pred} can be used to examine predictive capability of the regression model for future observations (Montgomery, 2013). The computation of PRESS is based on residual error (e) and diagonal elements of the hat matrix (H). H maps the vector of observed values into a vector of fitted values as seen in equation (39) (Myers et al., 2009).

$$H = X(X'X)^{-1}X' \quad (39)$$

$$PRESS = \sum_{i=1}^n \left(\frac{e_i}{1-h_{ii}} \right)^2 \quad (40)$$

R^2_{pred} is calculated with using PRESS value, as shown in equation (41). The R^2_{pred} values range is between zero and one. The value of R^2_{pred} is desired to be close to one to explain the variability in predicting new observations.

$$R^2_{Pred} = 1 - \frac{PRESS}{SS_{Total}} \quad (41)$$

A confidence interval (C.I.) can be identified for individual regression coefficients, mean response, and the prediction of future responses (Myers et al., 2009). The 100(1- α)% confidence interval for individual regression coefficients is illustrated below in equation (42).

$$b_j - t_{\alpha/2, n-p} \sqrt{\hat{\sigma}^2 C_{jj}} \leq \beta_j \leq b_j + t_{\alpha/2, n-p} \sqrt{\hat{\sigma}^2 C_{jj}} \quad (42)$$

The b_j is the predicted regression coefficient, β_j is the true value for the regression coefficient, C_{jj} is the diagonal element of the $(X'X)^{-1}$ matrix, $1-\alpha$ is the confidence level, n is the number of observations, $t_{\alpha/2, n-p}$ is the t statistic, σ is the error variance, and p is the number of model parameters (Montgomery, 2013).

Similarly, the 100(1- α)% confidence interval for the mean response is shown below.

$$\hat{y}(x_0) - t_{\alpha/2, n-p} \sqrt{\hat{\sigma} x_0' (X'X)^{-1} x_0} \leq \mu_{y(x_0)} \leq \hat{y}(x_0) + t_{\alpha/2, n-p} \sqrt{\hat{\sigma} x_0' (X'X)^{-1} x_0} \quad (43)$$

$\mu_{y(x_0)}$ is the actual mean response, $y(x_0)$ is the estimated mean response at the design point x_0 , X is the model matrix, $1-\alpha$ is the confidence level, n is the number of observations, $t_{\alpha/2, n-p}$ is the t statistic, σ is the error variance, and p is the number of model parameters.

Finally, the 100(1- α)% confidence interval for the prediction of future observations (prediction interval) is given in equation (44) (Myers et al., 2009).

$$\hat{y}(x_0) - t_{\alpha/2, n-p} \sqrt{\hat{\sigma}(1 + x_0' (X'X)^{-1} x_0)} \leq \mu_{y(x_0)} \leq \hat{y}(x_0) + t_{\alpha/2, n-p} \sqrt{\hat{\sigma}(1 + x_0' (X'X)^{-1} x_0)} \quad (44)$$

The additional σ^2 term is due to the variability of observations around the predicted mean at that location (Myers et al., 2009).

5.2 All-Propellers-On Mode

The all-propellers-on configuration has six factors (angle of attack, velocity, motor-1, motor-2, motor-3, motor-4) instead of ten factors. This is because the symmetry assumption was made for the motors, as seen in Figure 33. Matched motors were set to identical RPM.

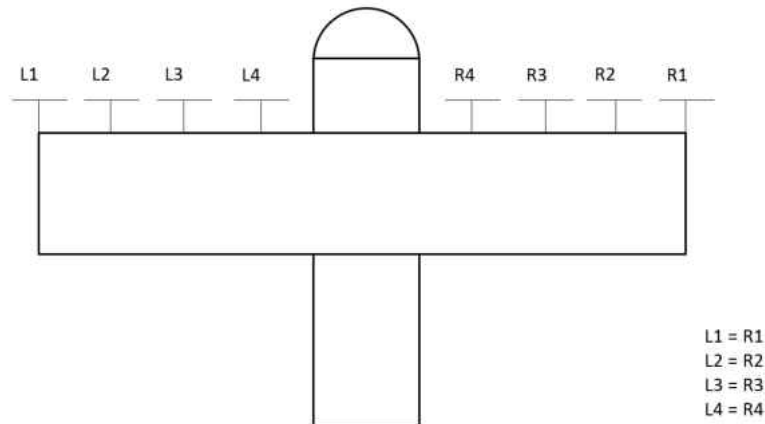


Figure 33. Motor name convention and symmetry

Factors and factor limits are shown in Table 5 for the all-propellers-on mode.

Factors		Low Limit	High Limit
A-o-A	Angle of attack (degree)	0	8
V	Velocity (m/s)	8	10
L1	Left Motor 1 (RPM)	10000	13000
L2	Left Motor 2 (RPM)	10000	13000
L3	Left Motor 3 (RPM)	10000	13000
L4	Left Motor 4 (RPM)	10000	13000

Table 5. Factors and factor limits for all-propellers-on mode

5.2.1 Normal Force Coefficient

A second order quadratic model was considered in this case to predict normal force coefficient as a function of six factors. ANOVA was used to determine significant and

insignificant model terms for building the final response model. The model included only significant terms. This reduction was made by the P-value approach. Due to the choice of $\alpha = 0.05$ (95% confidence), $P < 0.05$ indicates significance. A reduced second order polynomial model was identified by the ANOVA, as shown in Table 6.

Source	Sum of Squares	df	Mean Square	F Value	p-value Prob > F
Block	1.003E-003	1	1.003E-003		
Model	4.49	12	0.37	15827.77	< 0.0001
A-A-o-A	4.35	1	4.35	1.842E+005	< 0.0001
B-Velocity	0.046	1	0.046	1952.40	< 0.0001
C-L1	5.658E-003	1	5.658E-003	239.59	< 0.0001
D-L2	1.831E-003	1	1.831E-003	77.52	< 0.0001
E-L3	4.668E-003	1	4.668E-003	197.64	< 0.0001
F-L4	4.360E-003	1	4.360E-003	184.63	< 0.0001
AB	7.239E-003	1	7.239E-003	306.50	< 0.0001
AC	1.008E-004	1	1.008E-004	4.27	0.0428
AD	9.773E-005	1	9.773E-005	4.14	0.0460
AE	4.861E-004	1	4.861E-004	20.58	< 0.0001
AF	1.302E-003	1	1.302E-003	55.13	< 0.0001
E ²	4.505E-004	1	4.505E-004	19.08	< 0.0001
Residual	1.535E-003	65	2.362E-005		
Lack of Fit	1.467E-003	56	2.620E-005	3.47	0.0246
Pure Error	6.789E-005	9	7.543E-006		
Cor Total	4.49	78			

Table 6. ANOVA for all-propellers-on C_N

The fit statistics were used for examining model fit and prediction capabilities. The desired values for R^2 statistics is one or close to one as discussed in Section 5.1. The results indicate that the model described and predicted 99% of variability in the response due to changing the factors, as seen in Table 7.

Std. Dev.	4.860E-003	R-Squared	0.9997
Mean	0.66	Adj R-Squared	0.9996
C.V. %	0.74	Pred R-Squared	0.9994
PRESS	2.731E-003	Adeq Precision	456.395

Table 7. Fit statistics for all-propellers-on C_N

To check the normality, independence, and constant variance assumptions, residual diagnostics were used. The normal probability plot of the residuals for the developed model is shown in Figure 34 (a). In this plot, all residuals lie along a straight line representing a normal distribution due to transformed axes. This illustrates that all residuals were normally distributed and the normality assumption was validated. Figure 34 (b) shows a plot of residuals versus run order that was used to identify independence of the responses from time. The plot oscillates randomly around zero with no trend. Thus, the independence assumption is valid. Lastly, a plot of residuals versus predicted values is shown in Figure 34 (c) for checking the constant variance assumption. The plot has no cone or barrel shape and is well bounded within normal limits; therefore, the constant variance assumption is satisfied.

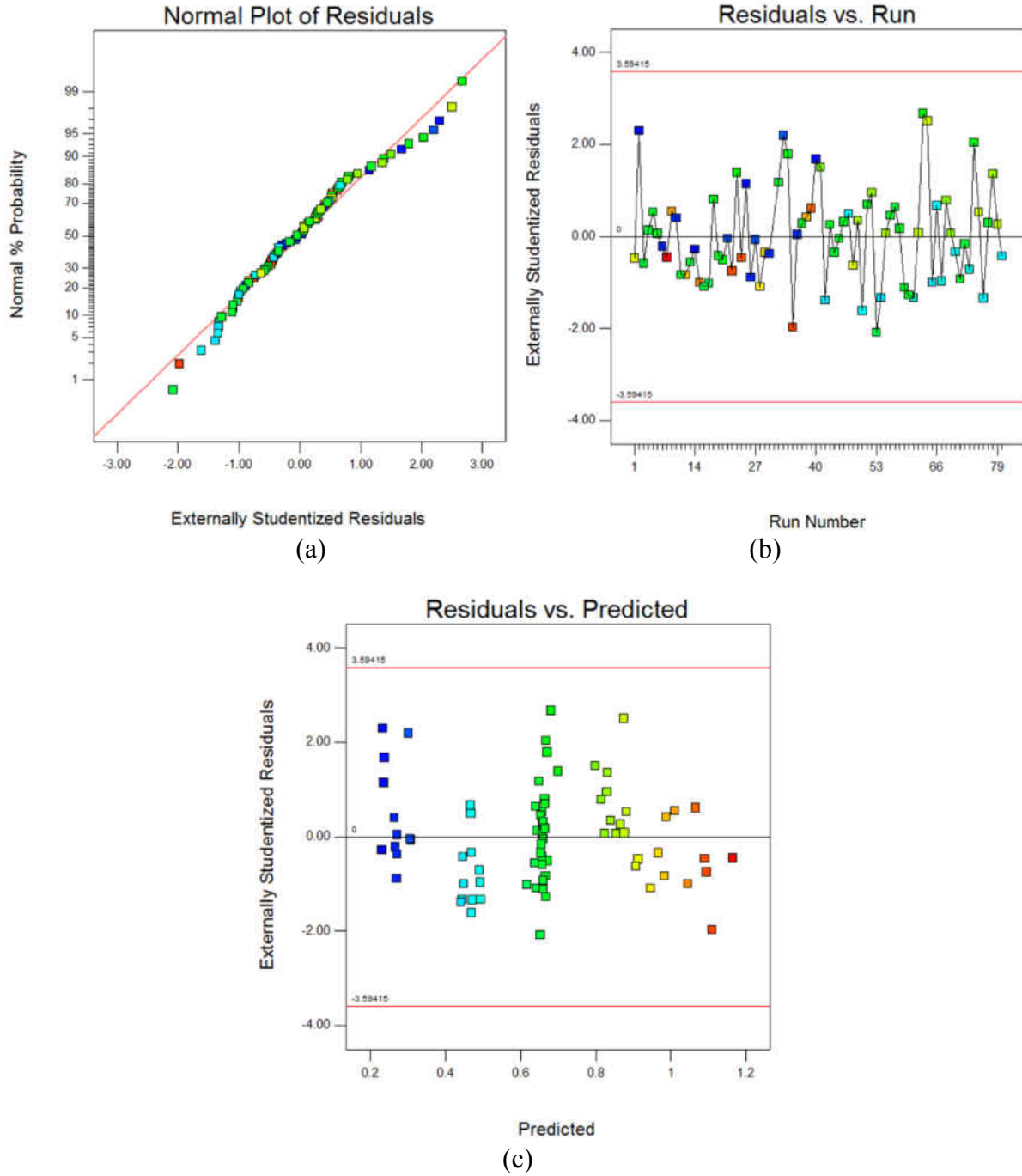


Figure 34. (a) Normality (b) Independence (c) Constant variance for all-propellers-on C_N

The model term coefficients for the second order response surface are illustrated in Table 8.

Factor	Coefficient Estimate
Intercept	-0.16660
A-A-o-A	0.10608
B-Velocity	-0.022784
C-L1	8.20235E-006
D-L2	4.05705E-006
E-L3	7.52859E-005
F-L4	3.22497E-006
AB	-4.65124E-003
AC	3.65923E-007
AD	3.60294E-007
AE	8.03548E-007
AF	1.31506E-006
E ²	-3.03135E-009

Table 8. Model term coefficients for all-propellers-on C_N

The final equation in terms of actual factors is given.

$$\begin{aligned}
C_N = & -0.16660 + 0.10608 * A - 0.022784 * B + 8.20235 * 10^{-6} * C + 4.05705 * 10^{-6} * D + 7.52859 * 10^{-5} \\
& * E + 3.22497 * 10^{-6} * F - 4.65124 * 10^{-3} * A * B + 3.65923 * 10^{-7} * A * C + 3.60294 * 10^{-7} * A * D \\
& + 8.03548 * 10^{-7} * A * E + 1.31506 * 10^{-6} * A * F - 3.03135 * 10^{-9} * E^2
\end{aligned} \tag{45}$$

The response surface plots for minimum and maximum RPM levels (10000-13000) are shown in Figures 35 and 36. These surface plots visualize the responses to help understand the characterization process. The normal force coefficient (C_N) is seen as a weak function of velocity and as expected, a strong function of angle-of-attack.

Design-Expert® Software
 Factor Coding: Actual
 CN
 ● Design points below predicted value
 1.16271
 0.229535
 X1 = A: A-o-A
 X2 = B: Velocity
 Actual Factors
 C: L1 = 10000
 D: L2 = 10000
 E: L3 = 10000
 F: L4 = 10000

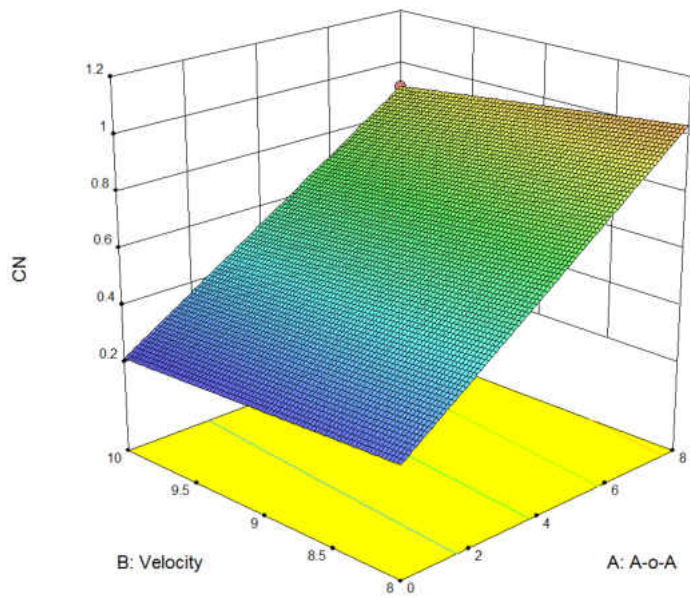


Figure 35. Response surface for all-propellers-on C_N at minimum RPM level

Design-Expert® Software
 Factor Coding: Actual
 CN
 ● Design points below predicted value
 1.16271
 0.229535
 X1 = A: A-o-A
 X2 = B: Velocity
 Actual Factors
 C: L1 = 13000
 D: L2 = 13000
 E: L3 = 13000
 F: L4 = 13000

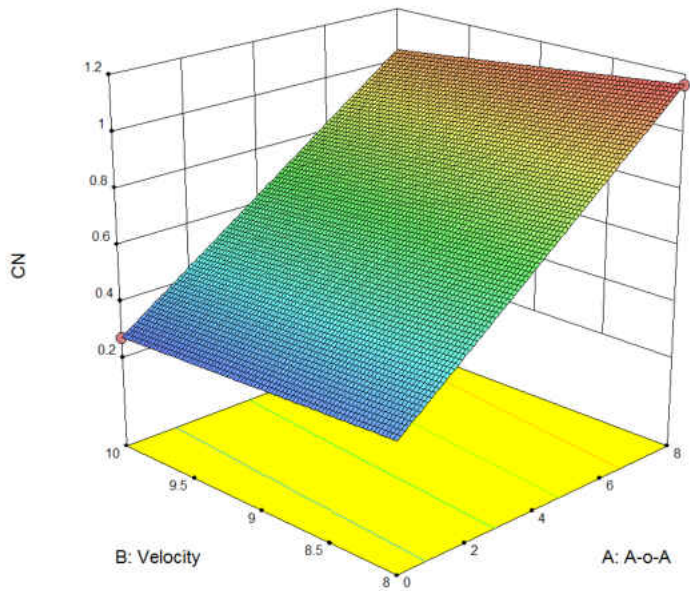


Figure 36. Response surface all-propellers-on C_N at maximum RPM level

A two-factor interaction plot for AB, AE and AF is presented in Figures 37, 38 and 39. The AB interaction term represents the normal force versus angle of attack for a velocity range between 8 – 10 m/s at highest RPM. Also, AE and AF interaction terms represent the normal force versus angle of attack for L3 and L4 RPM ranges between 10000 – 13000 at the lowest velocity. The plots of these interactions are not parallel, so they contribute to the final model significantly, although the latter two interactions are weak, as seen in the p-values.

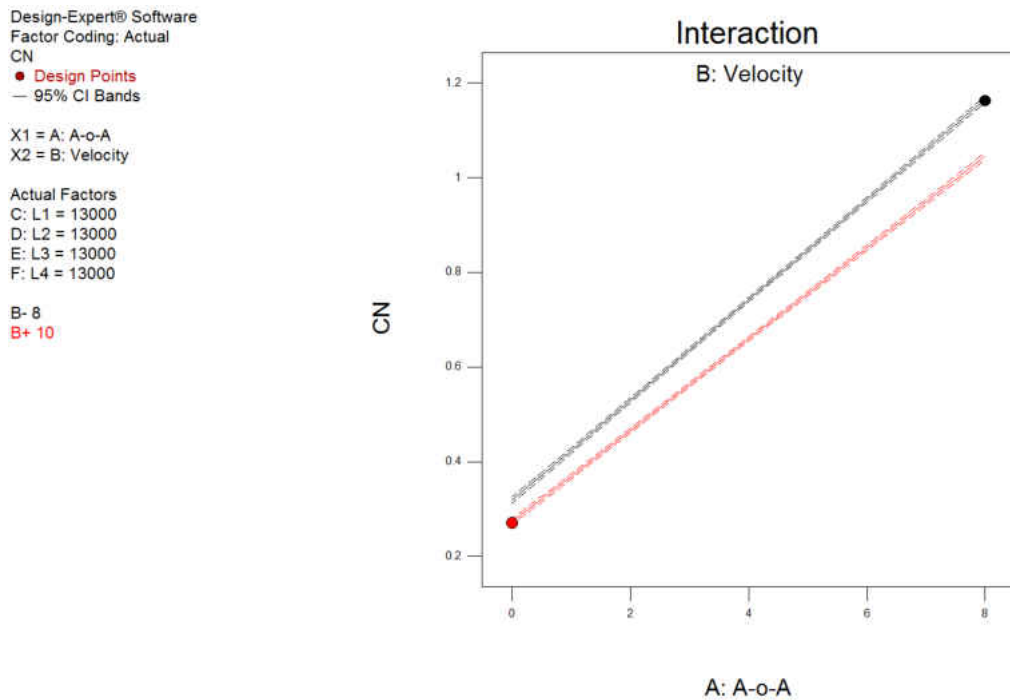


Figure 37. C_N as a function of angle of attack and velocity for all-propellers-on mode

Design-Expert® Software
Factor Coding: Actual
CN

● Design Points
— 95% CI Bands

X1 = A: A-o-A
X2 = E: L3

Actual Factors
B: Velocity = 8
C: L1 = 13000
D: L2 = 13000
F: L4 = 13000

E- 10000
E+ 13000

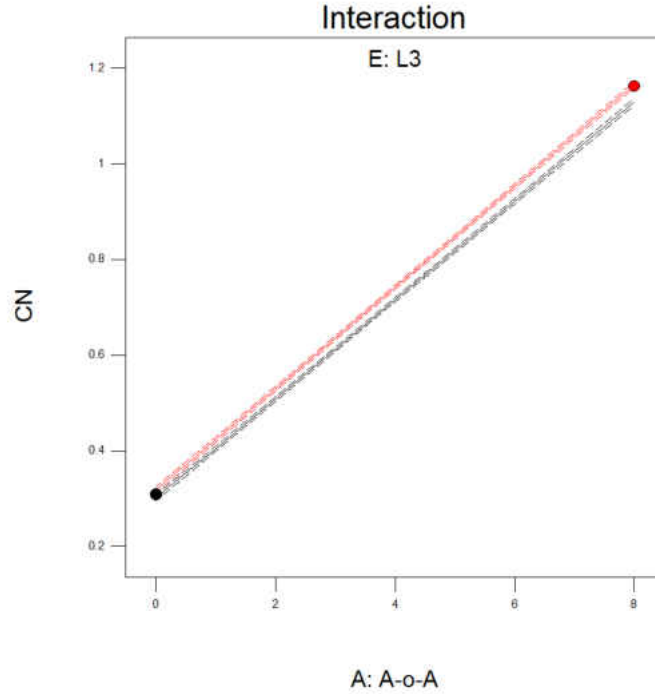


Figure 38. C_N as a function of angle of attack and L3 for all-propellers-on mode

Design-Expert® Software
Factor Coding: Actual
CN

● Design Points
— 95% CI Bands

X1 = A: A-o-A
X2 = F: L4

Actual Factors
B: Velocity = 8
C: L1 = 13000
D: L2 = 13000
E: L3 = 13000

F- 10000
F+ 13000

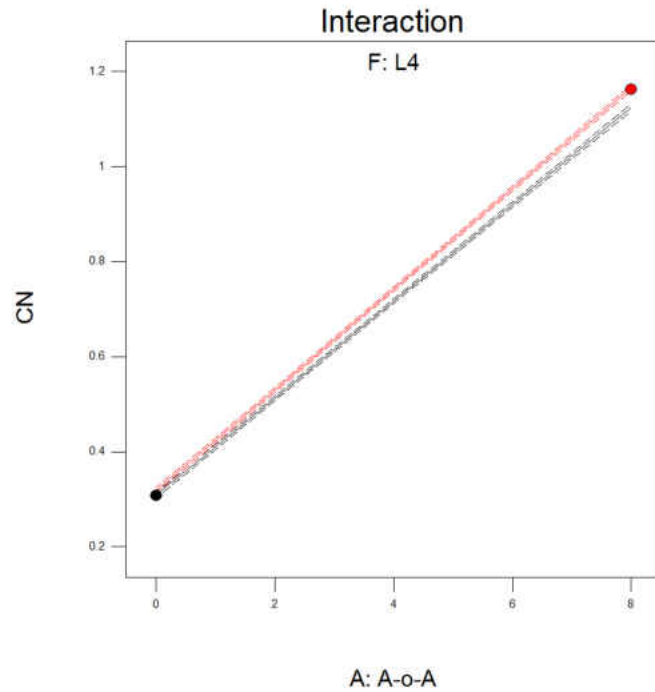


Figure 39. C_N as a function of angle of attack and L4 for all-propellers-on mode

To conclude that the response surface adequately models the observed data, normal force coefficient was measured at confirmation points. These confirmation points were independent of design point locations and help to make an assessment of the prediction capability of the model. The results of the confirmation point measurements are shown in Table 9. Measured and predicted normal force coefficients and the 95% prediction interval are shown in the table. All confirmation point results fell into a 95% prediction interval. Thus, the model adequately represents the observed data.

Run		95%PI Low	Predicted	Measured	95%PI High
1	C _N	0.481	0.491	0.485	0.501
2		0.793	0.804	0.810	0.814
3		0.593	0.604	0.614	0.614
4		0.753	0.763	0.773	0.773
5		0.885	0.896	0.905	0.907
6		0.285	0.296	0.302	0.306
7		0.410	0.421	0.426	0.431

Table 9. Prediction capability of the all-propellers-on C_N model

5.2.2 Axial Force Coefficient

A second order quadratic model was considered in this case to predict axial force coefficient as a function of six factors. The reduced second order polynomial model was identified as significant by ANOVA using the same procedure as described in section 5.2.1. The ANOVA results are provided in Table 10.

Source	Sum of Squares	df	Mean Square	F Value	p-value Prob > F
Block	3.749E-003	1	3.749E-003		
Model	0.77	19	0.040	2306.66	< 0.0001
A-A-o-A	0.049	1	0.049	2786.88	< 0.0001
B-Velocity	0.44	1	0.44	25057.81	< 0.0001
C-L1	0.035	1	0.035	1998.27	< 0.0001
D-L2	0.021	1	0.021	1199.48	< 0.0001
E-L3	0.026	1	0.026	1486.99	< 0.0001
F-L4	0.031	1	0.031	1787.34	< 0.0001
AB	3.171E-004	1	3.171E-004	18.11	< 0.0001
AE	1.125E-004	1	1.125E-004	6.42	0.0140
AF	1.996E-004	1	1.996E-004	11.40	0.0013
BC	2.757E-003	1	2.757E-003	157.46	< 0.0001
BD	5.193E-004	1	5.193E-004	29.65	< 0.0001
BE	8.455E-004	1	8.455E-004	48.28	< 0.0001
BF	7.971E-004	1	7.971E-004	45.52	< 0.0001
CE	1.010E-004	1	1.010E-004	5.77	0.0196
CF	7.611E-005	1	7.611E-005	4.35	0.0415
DE	1.353E-004	1	1.353E-004	7.72	0.0073
EF	2.912E-004	1	2.912E-004	16.63	0.0001
A ²	1.121E-003	1	1.121E-003	64.01	< 0.0001
B ²	2.225E-003	1	2.225E-003	127.07	< 0.0001
Residual	1.016E-003	58	1.751E-005		
Lack of Fit	8.773E-004	49	1.790E-005	1.16	0.4329
Pure Error	1.384E-004	9	1.538E-005		
Cor Total	0.77	78			
Block	3.749E-003	1	3.749E-003		

Table 10. ANOVA for all-propellers-on C_A

The fit statistics are seen in Table 11 and completely support the regression model.

Std. Dev.	4.185E-003	R-Squared	0.9987
Mean	-0.30	Adj R-Squared	0.9982
C.V. %	1.39	Pred R-Squared	0.9973
PRESS	2.108E-003	Adeq Precision	267.359

Table 11. Fit Statistics for all-propellers-on C_A

Normality, independence and constant variance assumptions were validated as described in section 5.2.1. A normal probability plot of the residuals for the developed model is shown in Figure 40 (a). Figure 40 (b) shows a plot of residuals versus run order that was used to validate

independence. Lastly, a plot of residuals versus predicted values is shown in Figure 40 (c) for checking the constant variance assumption. All residual diagnostic plots are seen as acceptable.

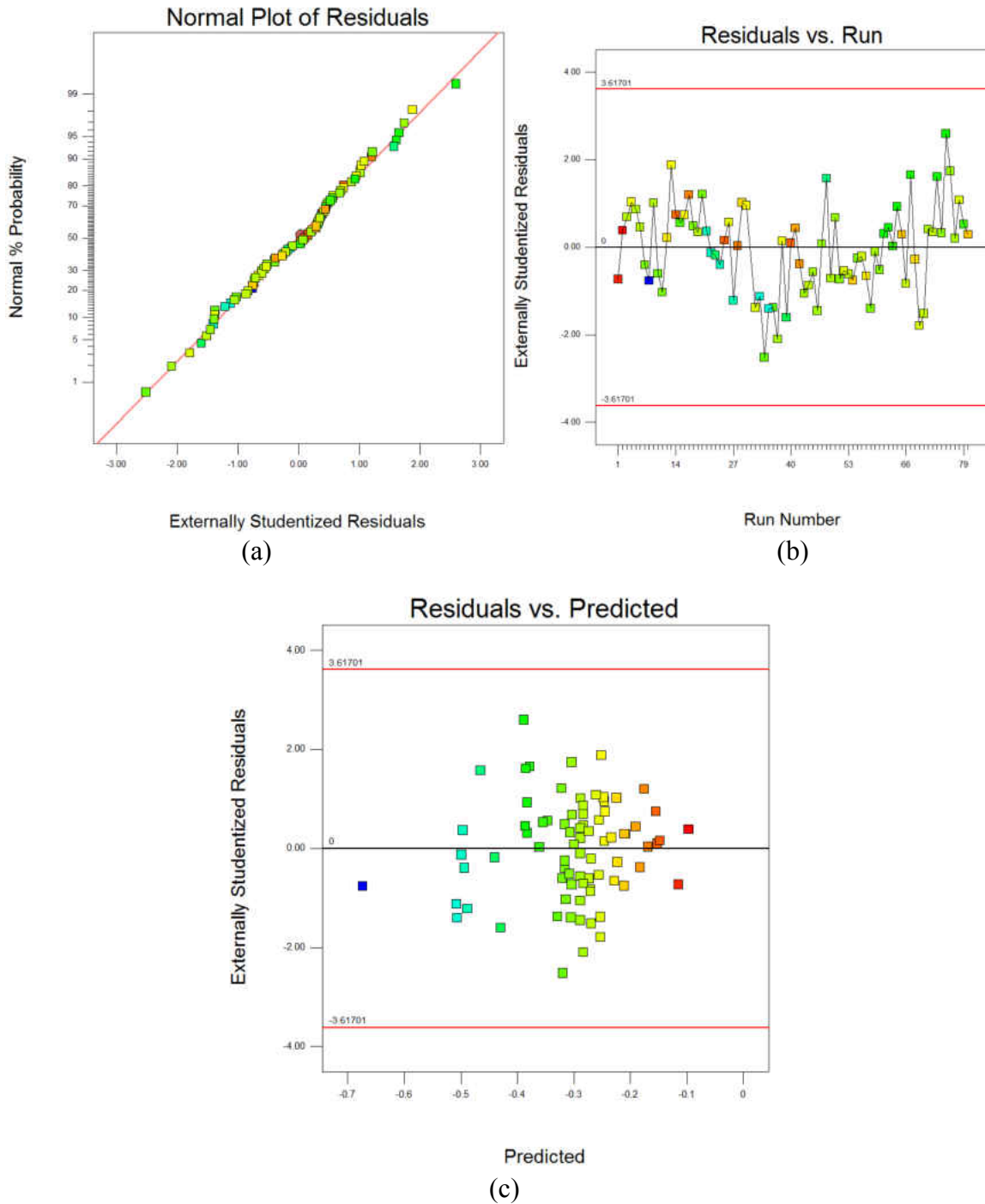


Figure 40. (a) Normality (b) Independence (c) Constant variance for all-propellers-on C_A

The model term coefficients for the second order response surface are given in Table 12.

Factor	Coefficient Estimate
Intercept	0.11683
A-A-o-A	-1.01054E-003
B-Velocity	0.33421
C-L1	-9.95128E-005
D-L2	-6.61061E-005
E-L3	-1.04246E-004
F-L4	-6.93875E-005
AB	1.02190E-003
AE	-4.05693E-007
AF	-5.48548E-007
BC	8.03554E-006
BD	3.54175E-006
BE	4.33477E-006
BF	4.25708E-006
CE	1.02516E-009
CF	-9.03277E-010
DE	1.20507E-009
EF	1.71531E-009
A ²	-1.07932E-003
B ²	-0.024332

Table 12. Model Term Coefficients for all-propellers-on C_A

The final equation in terms of actual factors is given.

$$\begin{aligned}
 C_A = & 0.11683 - 1.01054 * 10^{-3} * A + 0.33421 * B - 9.95128 * 10^{-5} * C - 6.61061 * 10^{-5} * D - 1.04246 * 10^{-4} \\
 & * E - 6.93875 * 10^{-5} * F + 1.02190 * 10^{-3} * A * B - 4.05693 * 10^{-7} * A * E - 5.48548 * 10^{-7} * A * F \\
 & + 8.03554 * 10^{-6} * B * C + 3.54175 * 10^{-6} * B * D + 4.33477 * 10^{-6} * B * E + 4.25708 * 10^{-6} * B * F \\
 & + 1.02516 * 10^{-9} * C * E - 9.03277 * 10^{-10} * C * F + 1.20507 * 10^{-9} * D * E + 1.71531 * 10^{-9} * E * F \\
 & - 1.07932 * 10^{-3} * A^2 - 0.024332 * B^2
 \end{aligned} \tag{46}$$

The response surface plots for minimum and maximum RPM levels (10000-13000) were shown in Figures 41 and 42.

Design-Expert® Software
 Factor Coding: Actual
 Ca
 ● Design points above predicted value
 -0.0958695
 -0.675712
 X1 = A: A-o-A
 X2 = B: Velocity
 Actual Factors
 C: L1 = 10000
 D: L2 = 10000
 E: L3 = 10000
 F: L4 = 10000

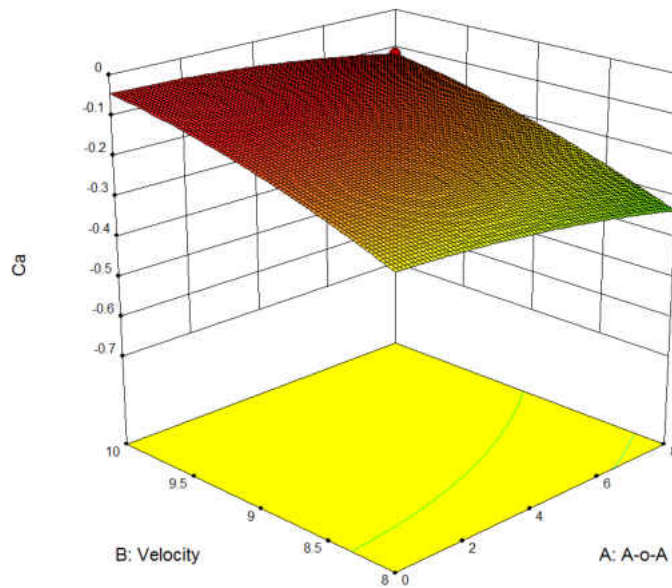


Figure 41. Response surface for all-propellers-on C_A at minimum RPM

Design-Expert® Software
 Factor Coding: Actual
 Ca
 ● Design points above predicted value
 -0.0958695
 -0.675712
 X1 = A: A-o-A
 X2 = B: Velocity
 Actual Factors
 C: L1 = 13000
 D: L2 = 13000
 E: L3 = 13000
 F: L4 = 13000

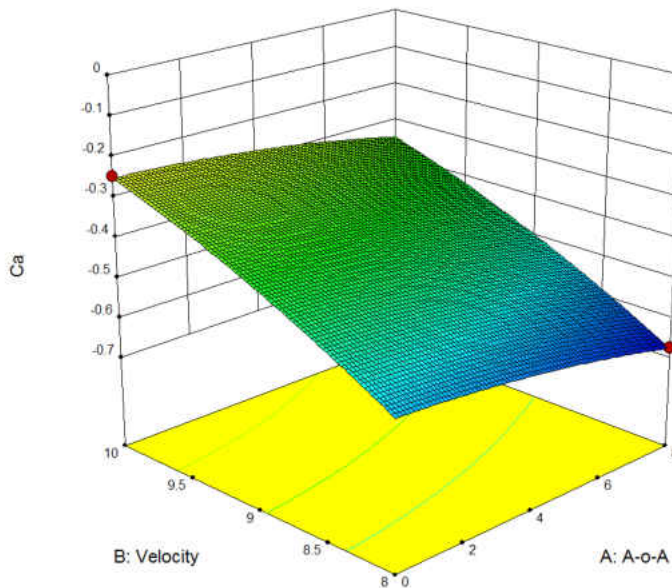


Figure 42. Response surface for all-propellers-on C_A at maximum RPM

A two-factor interaction graph for C_A is shown below. The BC interaction term represents the Velocity x RPM interaction. Figure 43 shows axial force versus velocity for a L1 RPM range between 10000 – 13000, while other RPM levels are at the maximum level. This result shows that L1 had a more significant effect on axial force at low velocity versus high. This is felt to be due to reduction in induced drag, which coincided with a reduction on total drag; hence, in the axial force.

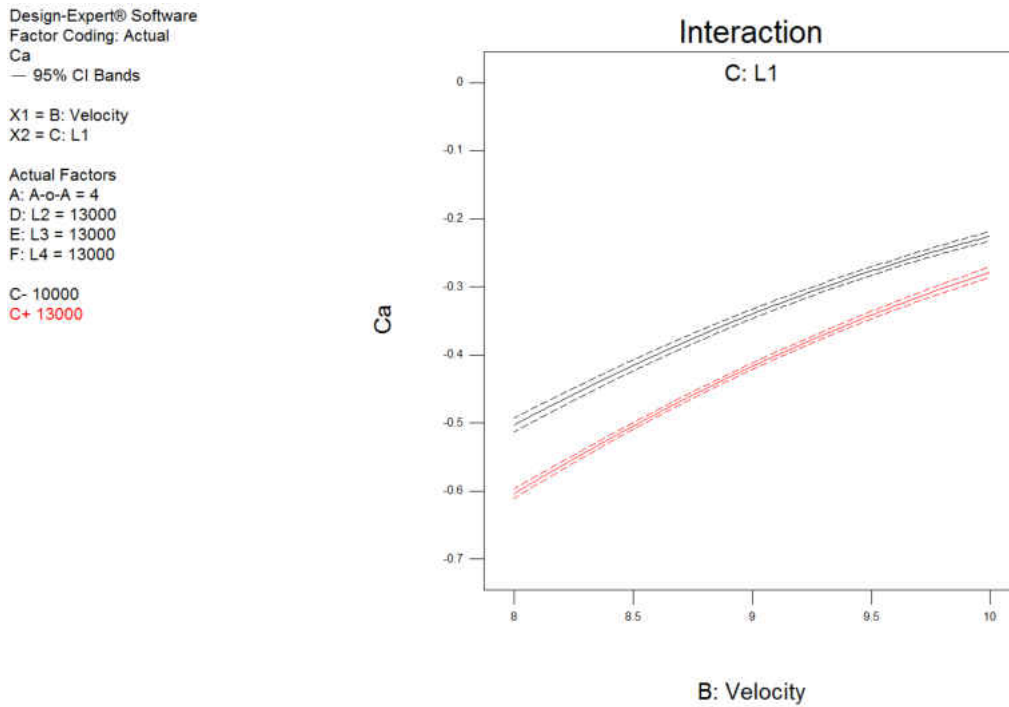


Figure 43. C_A as a function of velocity and L1 for all-propellers-on mode

Confirmation point measurements are shown in Table 13. All confirmation point results fell into the 95% prediction interval. Thus, the regression model adequately represents the observed data.

Run		95%PI Low	Predicted	Measured	95%PI High
1	C _A	-0.408	-0.399	-0.405	-0.390
2		-0.232	-0.222	-0.224	-0.211
3		-0.460	-0.450	-0.453	-0.440
4		-0.328	-0.320	-0.322	-0.311
5		-0.248	-0.237	-0.236	-0.227
6		-0.413	-0.403	-0.399	-0.393
7		-0.146	-0.136	-0.129	-0.126

Table 13. Prediction capability of all-propellers-on C_A model

5.3 Wing-Along Mode

Wing-alone mode has two factors are shown in the table below.

Factors		Low Limit	High Limit
A-o-A	Angle of attack (degree)	0	8
V	Velocity (m/s)	8	10

Table 14. Factors and factor limits for wing-alone mode

5.3.1 Normal Force Coefficient

A second order quadratic model was considered in this case to predict the normal force coefficient as a function angle of attack. ANOVA was used to determine significant and insignificant model terms for building a final response model. The model included only significant terms. This reduction was again made by the P-value approach. The ANOVA results are provided in Table 15.

Source	Sum of Squares	df	Mean Square	F Value	p-value Prob > F
Block	1.704E-004	1	1.704E-004		
Model	0.73	2	0.37	23945.49	< 0.0001
A-A-o-A	0.73	1	0.73	47824.79	< 0.0001
A ²	1.012E-003	1	1.012E-003	66.20	< 0.0001
Residual	3.362E-004	22	1.528E-005		
Lack of Fit	2.075E-004	14	1.482E-005	0.92	0.5738
Pure Error	1.287E-004	8	1.609E-005		
Cor Total	0.73	25			

Table 15. ANOVA for wing-alone C_N

The fit statistics values for R² are shown in Table 16.

Std. Dev.	3.909E-003	R-Squared	0.9995
Mean	0.57	Adj R-Squared	0.9995
C.V. %	0.68	Pred R-Squared	0.9993
PRESS	5.094E-004	Adeq Precision	407.176

Table 16. Fit statistics for wing-alone C_N

Figure 44 summarizes the residual diagnostics, no problems were found.

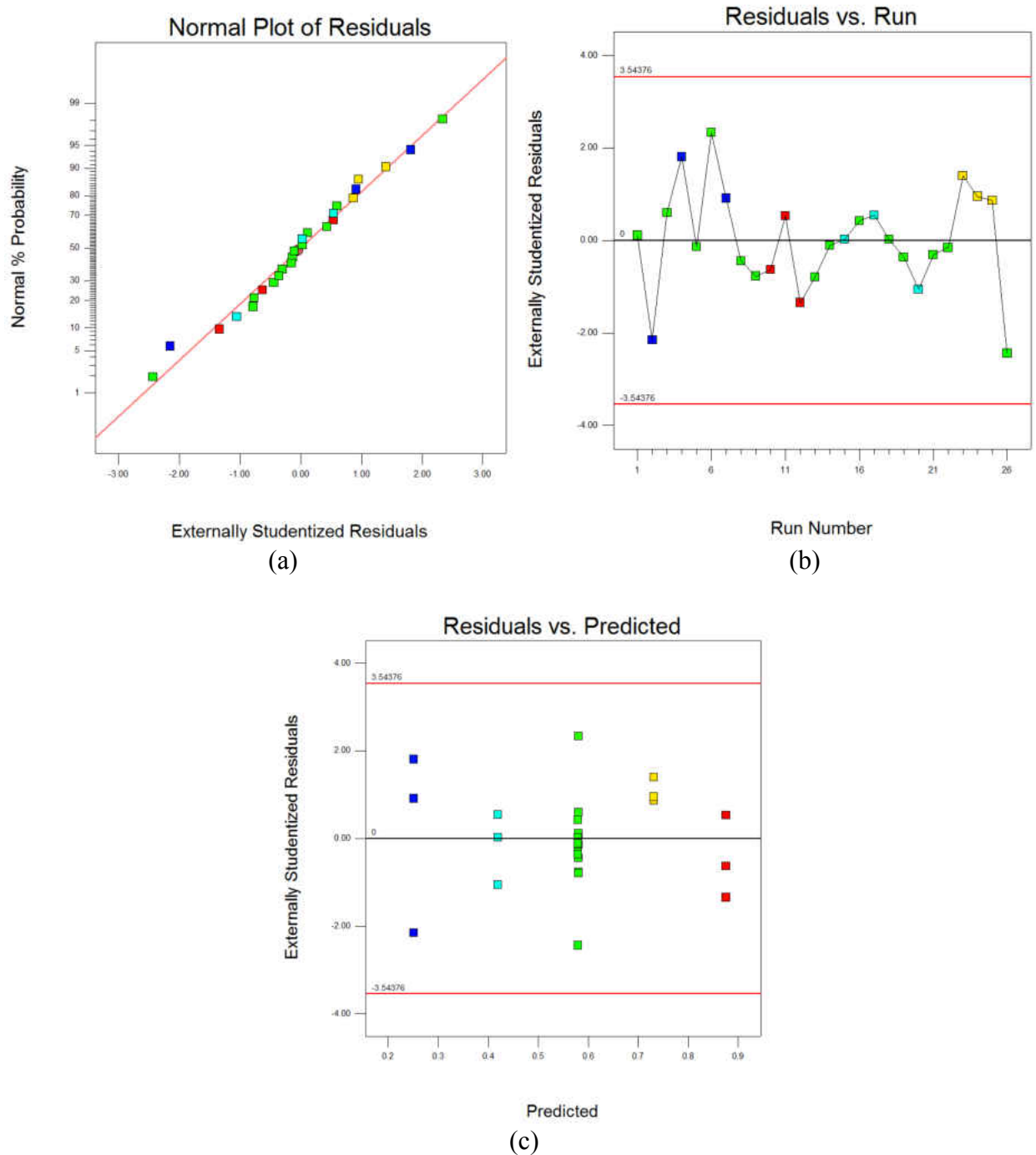


Figure 44. (a) Normality (b) Independence (c) Constant variance for wing-alone C_N

The model term coefficients for the second order response surface are illustrated in Table 17.

Factor	Coefficient Estimate
Intercept	0.25060
A-A-o-A	0.086625
A ²	-1.07294E-003

Table 17. Model term coefficients for wing-alone C_N

Therefore, the final equation, in terms of actual factors, is given.

$$C_N = 0.25060 + 0.086625 * A - 1.07294 * 10^{-3} * A^2 \quad (47)$$

The response surface plot is shown in Figure 45.

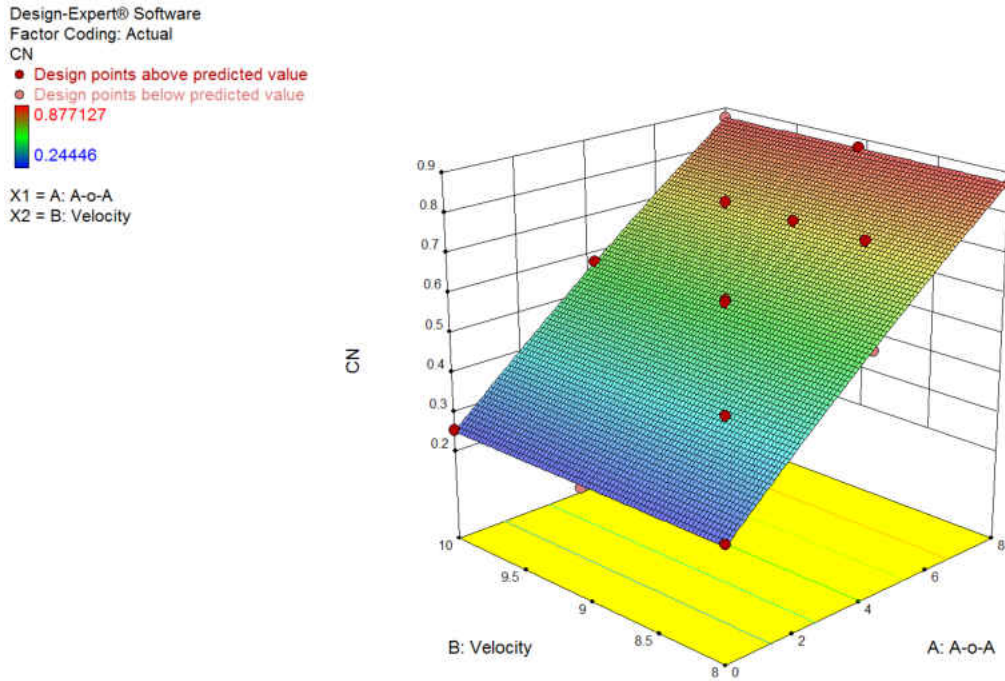


Figure 45. Response surface for wing-alone C_N

There is no interaction term for wing alone C_N . C_N is just a function of angle of attack.

The results of the confirmation point measurements are shown in Table 18. All confirmation point results fell into a 95% prediction interval. Thus, model adequately represents the observed data.

Run		95%PI Low	Predicted	Measured	95%PI High
1	C _N	0.492	0.500	0.499	0.509
2		0.648	0.656	0.665	0.665
3		0.648	0.656	0.658	0.665

Table 18. Prediction capability of the wing-alone C_N model

5.3.2 Axial Force Coefficient

A second order quadratic model was considered in this case to predict axial force coefficient as a function of two factors, angle of attack and velocity. ANOVA was used to determine significant and insignificant model terms for building the response model. The ANOVA results are provided in Table 19.

Source	Sum of Squares	df	Mean Square	F Value	p-value Prob > F
Block	2.973E-005	1	2.973E-005		
Model	0.011	3	3.753E-003	1445.28	< 0.0001
A-A-o-A	0.011	1	0.011	4097.33	< 0.0001
B-Velocity	1.352E-005	1	1.352E-005	5.21	0.0331
A ²	6.057E-004	1	6.057E-004	233.30	< 0.0001
Residual	5.452E-005	21	2.596E-006		
Lack of Fit	2.857E-005	13	2.198E-006	0.68	0.7442
Pure Error	2.595E-005	8	3.244E-006		
Cor Total	0.011	25			

Table 19. ANOVA for wing-alone C_A

The fit statistics are shown in Table 20.

Std. Dev.	1.611E-003	R-Squared	0.9952
Mean	0.012	Adj R-Squared	0.9945
C.V. %	13.84	Pred R-Squared	0.9930
PRESS	7.865E-005	Adeq Precision	110.398

Table 20. Fit Statistics for wing-alone C_A

The normality, independence and constant variance assumptions were validated as shown in Figure 46. All assumptions were validated.

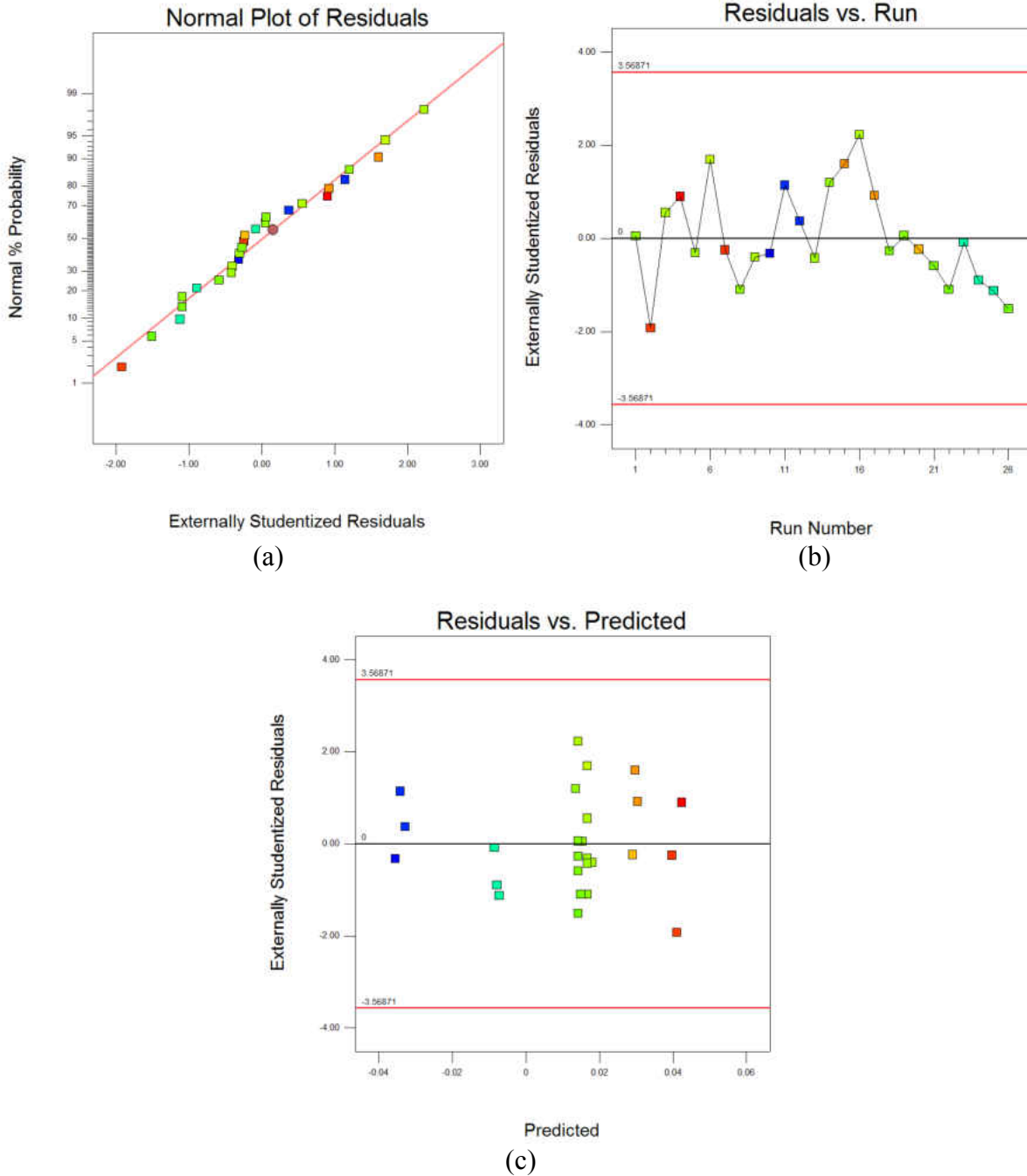


Figure 46. (a) Normality (b) Independence (c) constant variance for wing-alone C_A

The model term coefficients for the second order response surface is illustrated in Table 21.

Factor	Coefficient Estimate
Intercept	0.051931
A-A-o-A	-2.77360E-003
B-Velocity	-1.34242E-003
A ²	-8.30249E-004

Table 21. Model term coefficients for wing-alone C_A

The final equation in terms of actual factors is given.

$$C_A = 0.051931 - 2.77360 * 10^{-3} * A - 1.34242 * 10^{-3} * B - 8.30249 * 10^{-4} * A^2 \quad (48)$$

The response surface plot is shown in Figure 47.

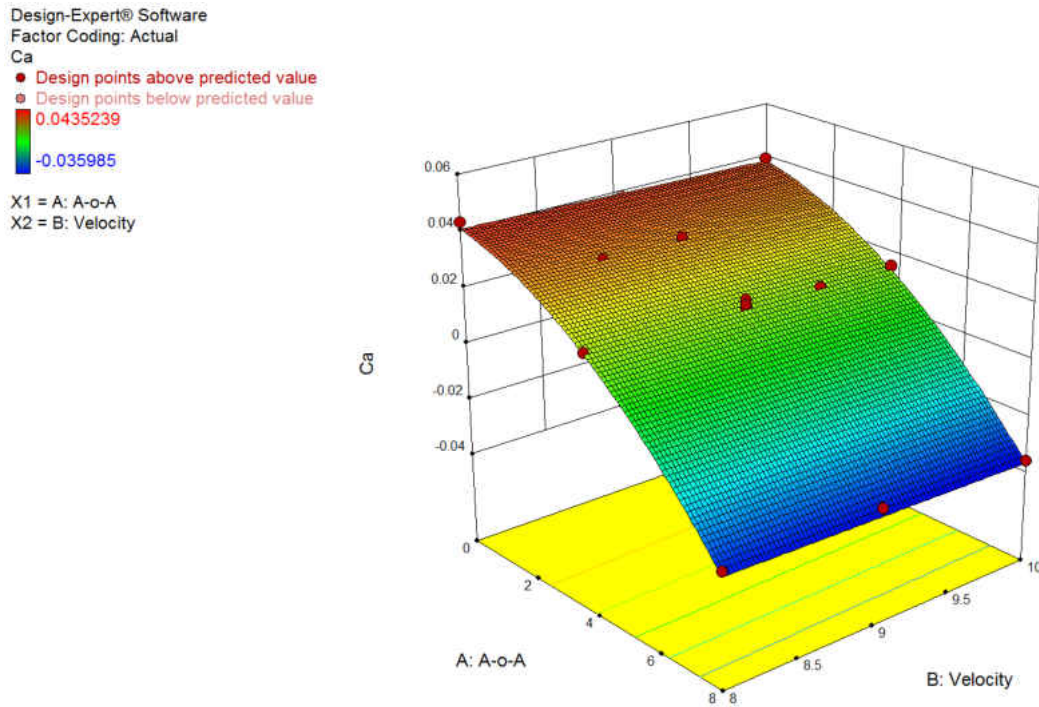


Figure 47. Response surface for wing-alone C_A

There is no interaction term for wing-alone C_A . C_A is a just a function of angle of attack.

The results of the confirmation point measurements are shown in Table 22. All confirmation point results fell into a 95% prediction interval. Thus, model adequately represents the observed data.

Run		95%PI Low	Predicted	Measured	95%PI High
1	C _A	0.021	0.025	0.021	0.029
2		0.0002	0.003	0.002	0.007
3		0.001	0.004	0.003	0.008

Table 22. Prediction capability of the wing-alone C_A model

5.4 Wing-Tip-Propellers-Alone Mode

Wingtip-propellers-alone mode has three factors, as seen in Table 23.

Factors		Low Limit	High Limit
A-o-A	Angle of attack (degree)	0	8
V	Velocity (m/s)	8	10
L1	Left Motor 1 (RPM)	10000	13000

Table 23. Factors and factor limits for wingtip-alone mode

5.4.1 Normal Force Coefficient

Again, a reduced second order polynomial model was identified as significant by ANOVA. The ANOVA results are provided in Table 24.

Source	Sum of Squares	df	Mean Square	F Value	p-value Prob > F
Block	1.952E-004	1	1.952E-004		
Model	1.36	5	0.27	4435.93	< 0.0001
A-A-o-A	1.36	1	1.36	22098.14	< 0.0001
B-Velocity	1.041E-003	1	1.041E-003	16.94	0.0002
C-L1	2.653E-003	1	2.653E-003	43.19	< 0.0001
AB	3.465E-004	1	3.465E-004	5.64	0.0235
A ²	9.669E-004	1	9.669E-004	15.74	0.0004
Residual	2.027E-003	33	6.143E-005		
Lack of Fit	1.569E-003	23	6.823E-005	1.49	0.2608
Pure Error	4.580E-004	10	4.580E-005		
Cor Total	1.36	39			

Table 24. ANOVA for wing-tip-propellers-alone C_N

The fit statistics results indicated that the model describes and can predict over 99% of the variability in the response due to factor changes, as seen in Table 25.

Std. Dev.	7.838E-003	R-Squared	0.9985
Mean	0.60	Adj R-Squared	0.9983
C.V. %	1.31	Pred R-Squared	0.9973
PRESS	3.626E-003	Adeq Precision	215.469

Table 25. Fit Statistics for wing-tip-propellers-alone C_N

Residual diagnostics for the developed regression model are shown in Figure 48. No problems were found.

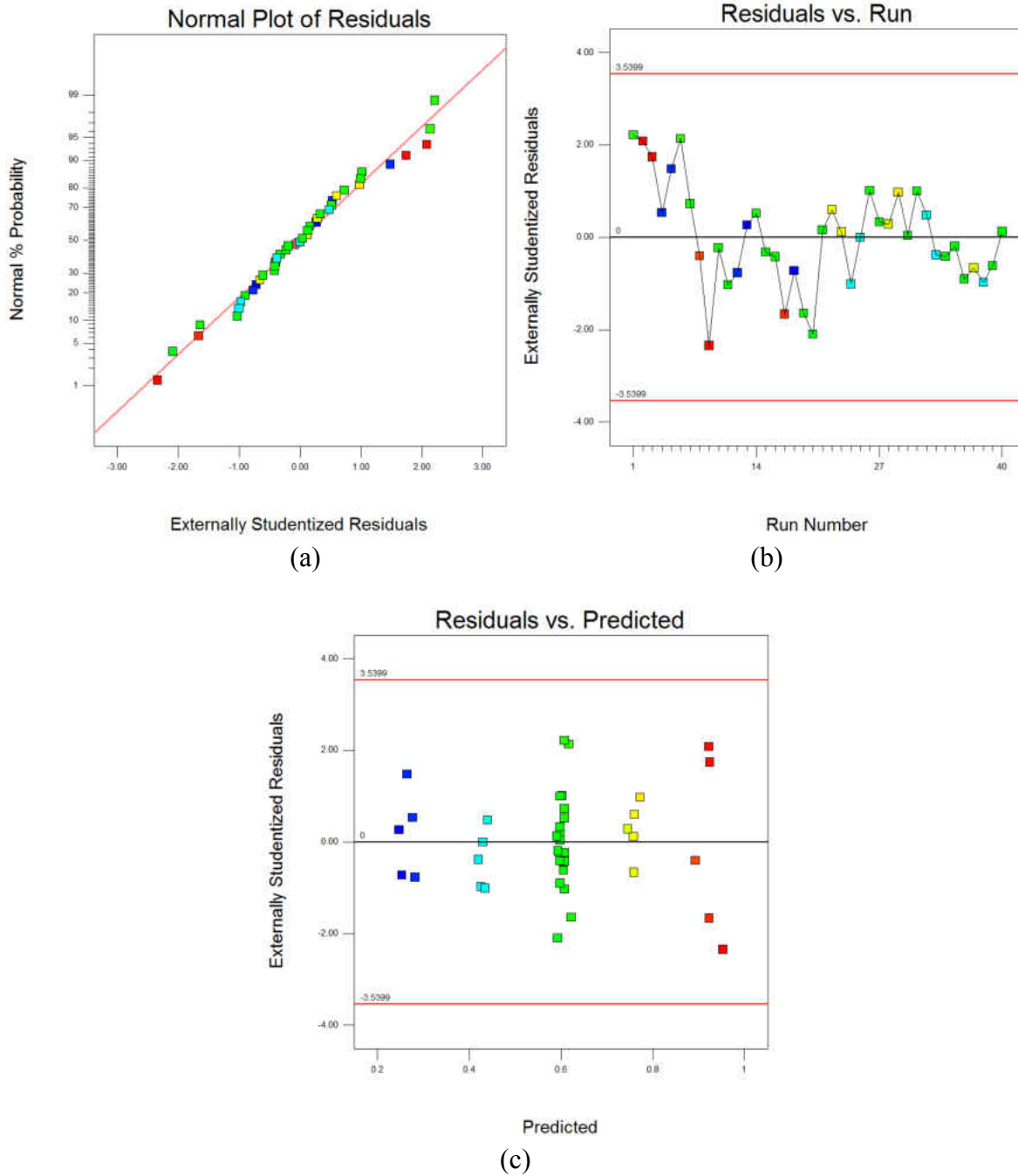


Figure 48. (a) Normality (b) Independence (c) Constant variance for wing-tip-propellers C_N

The model term coefficients for the second order response surface is illustrated in the table below.

Factor	Coefficient Estimate
Intercept	0.17265
A-A-o-A	0.10350
B-Velocity	-2.73947E-003
C-L1 and R1	9.71212E-006
AB	-1.59610E-003
A ²	-8.43165E-004

Table 26. Model term coefficients for wing-tip-propellers-alone C_N

The final equation in terms of actual factors is given.

$$C_N = 0.17265 + 0.10350 * A - 2.73947 * 10^{-3} * B + 9.71212 * 10^{-6} * C - 1.59610 * 10^{-3} * A * B - 8.43165 * 10^{-4} * A^2 \quad (49)$$

The response surface plots for minimum and maximum RPM levels (10000-13000) are shown in Figures 49 and 50.

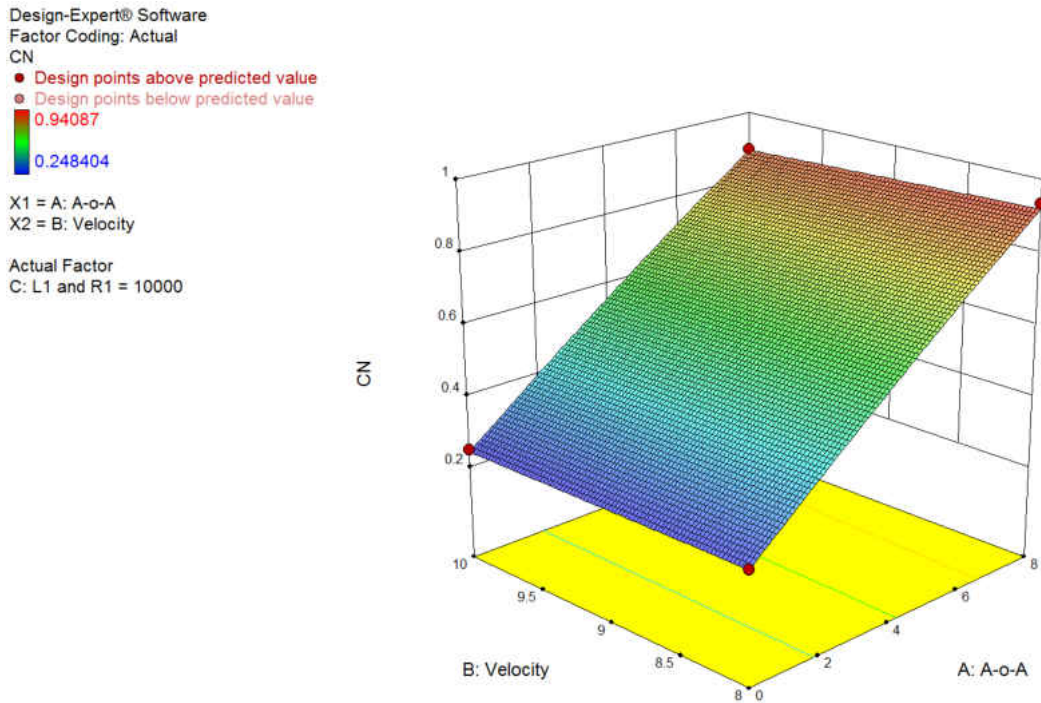


Figure 49. Response surface for wing-tip-propellers-alone C_N at minimum RPM

Design-Expert® Software
 Factor Coding: Actual
 CN
 ● Design points above predicted value
 ● Design points below predicted value
 0.94087
 0.248404
 X1 = A: A-o-A
 X2 = B: Velocity
 Actual Factor
 C: L1 and R1 = 13000

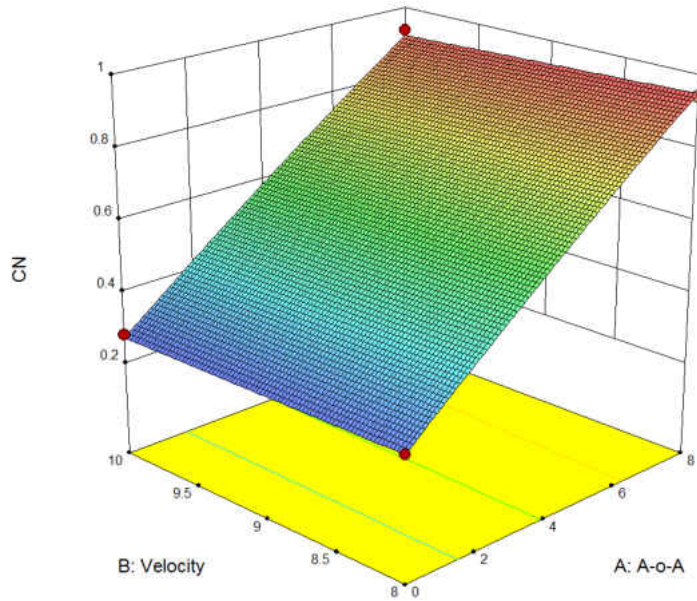


Figure 50. Response surface for wing-tip-propellers-alone C_N at maximum RPM

Angle of attack and velocity are the only interaction terms for the wing-tip-propellers-alone C_N , as seen in Figure 51.

Design-Expert® Software
 Factor Coding: Actual
 CN
 ● Design Points
 — 95% CI Bands
 X1 = A: A-o-A
 X2 = B: Velocity
 Actual Factor
 C: L1 and R1 = 13000
 B- 8
 B+ 10

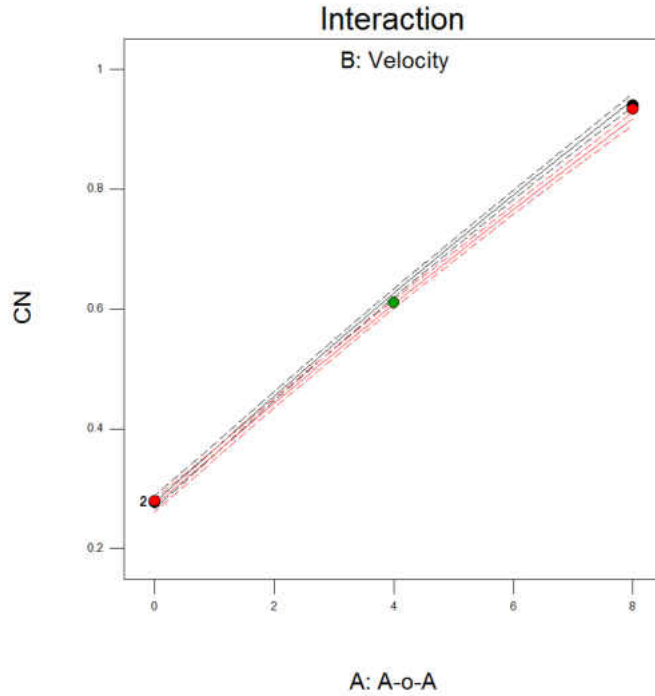


Figure 51. C_N as a function of velocity and angle of attack for wingtip-propellers-alone mode

The results of the confirmation point measurements are shown in Table 27. All confirmation point results fell into a 95% prediction interval. Thus, the model adequately represents the observed data.

Run		95%PI Low	Predicted	Measured	95%PI High
1	C _N	0.419	0.436	0.424	0.453
2		0.734	0.751	0.753	0.768
3		0.524	0.541	0.535	0.559
4		0.667	0.684	0.681	0.700
5		0.810	0.828	0.829	0.846
6		0.250	0.269	0.254	0.288

Table 27. Prediction capability of the wing-tip-propellers-alone C_N

5.4.2 Axial Force Coefficient

A second order quadratic model was considered in this case to predict the axial force coefficient as a function of three factors, angle of attack, velocity, and tip motor rpm. The ANOVA results are provided in Table 28.

Source	Sum of Squares	df	Mean Square	F Value	p-value Prob > F
Block	6.191E-004	1	6.191E-004		
Model	0.055	6	9.122E-003	1510.35	< 0.0001
A-A-o-A	0.020	1	0.020	3265.32	< 0.0001
B-Velocity	0.013	1	0.013	2131.57	< 0.0001
C-L1	0.020	1	0.020	3284.61	< 0.0001
BC	7.002E-004	1	7.002E-004	115.93	< 0.0001
A ²	6.676E-004	1	6.676E-004	110.55	< 0.0001
B ²	7.926E-005	1	7.926E-005	13.12	0.0010
Residual	1.933E-004	32	6.039E-006		
Lack of Fit	1.834E-004	22	8.335E-006	8.42	0.0007
Pure Error	9.903E-006	10	9.903E-007		
Cor Total	0.056	39			

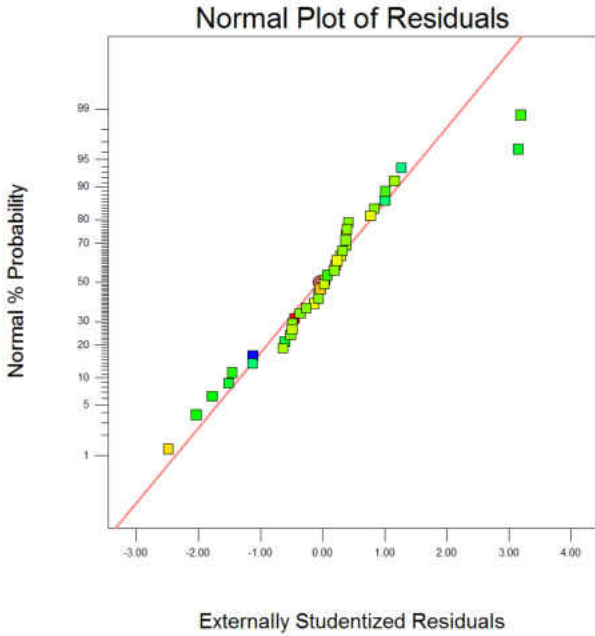
Table 28. ANOVA for wing-tip-propellers-alone C_A

The fit statistics are seen in Table 29.

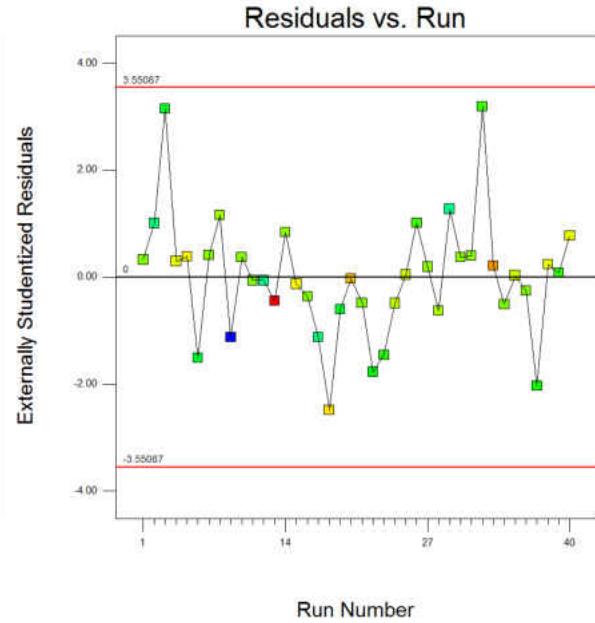
Std. Dev.	2.458E-003	R-Squared	0.9965
Mean	-0.062	Adj R-Squared	0.9958
C.V. %	3.99	Pred R-Squared	0.9930
PRESS	3.839E-004	Adeq Precision	203.174

Table 29. Fit Statistics for wing-tip-propellers-alone C_A

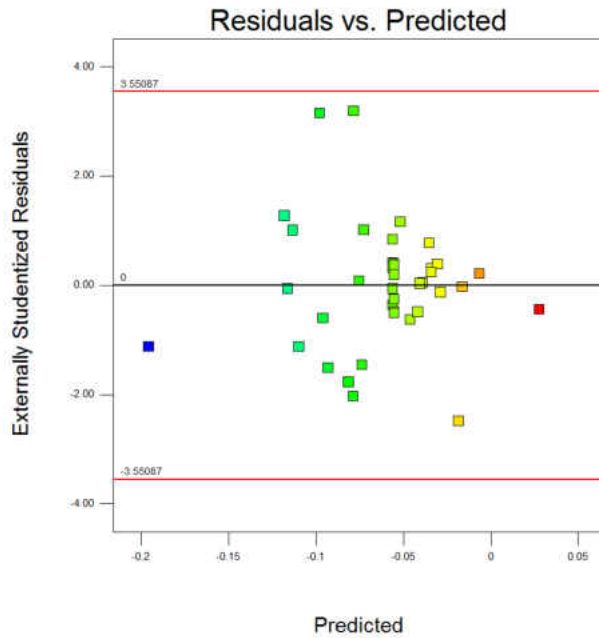
Residual diagnostic results are shown in Figure 52. While some residuals were seen near limits, no problems were cited from the inclusion of all data in the model build.



(a)



(b)



(c)

Figure 52. (a) Normality (b) Independence (c) Constant variance for wing-tip-propellers C_A

The model term coefficients for second order response surface is illustrated in Table 30.

Factor	Coefficient Estimate
Intercept	0.22170
A-A-o-A	-2.92348E-003
B-Velocity	0.049418
C-L1	-8.10142E-005
BC	6.05069E-006
A ²	-8.75809E-004
B ²	-4.82829E-003

Table 30. Model term coefficients for wing-tip-propellers-alone C_A

The final equation in terms of actual factors is given.

$$C_A = 0.22170 - 2.92348 * 10^{-3} * A + 0.049418 * B - 8.10142 * 10^{-5} * C + 6.05069 * 10^{-6} * B * C - 8.75809 * 10^{-4} * A^2 - 4.82829 * 10^{-3} * B^2 \quad (50)$$

The response surface plots for minimum and maximum angle-of-attack levels (0-8) are shown in Figures 53 and 54.

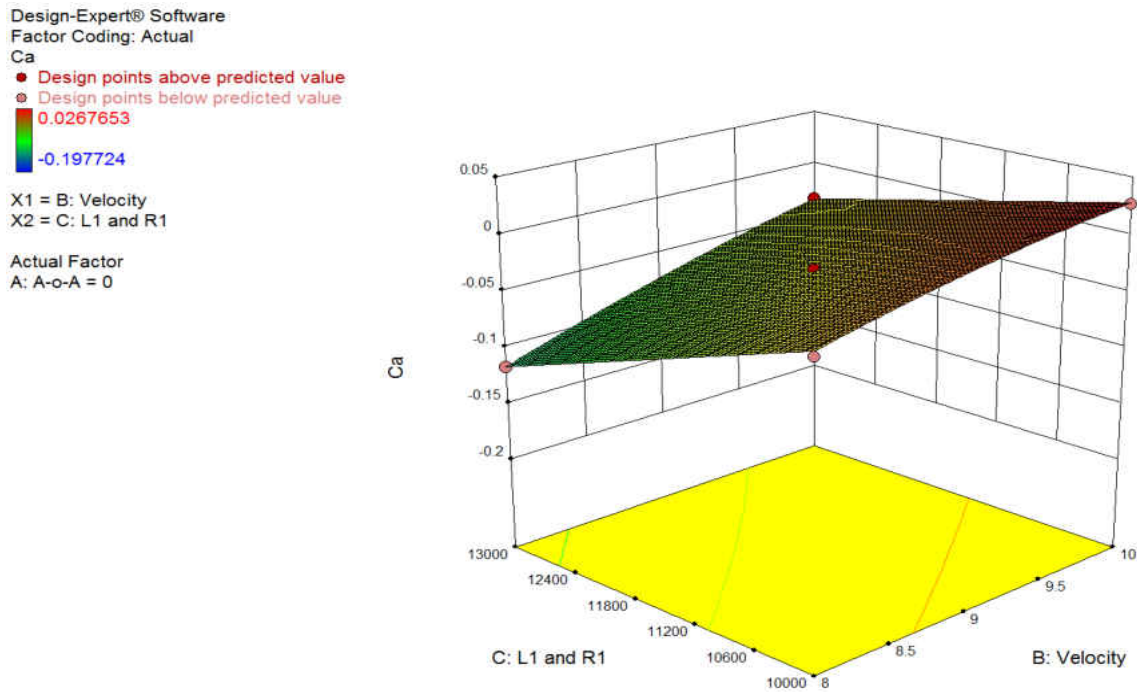


Figure 53. Response surface for wing-tip-propellers-alone C_A at zero angle of attack

Design-Expert® Software
 Factor Coding: Actual
 Ca
 ● Design points above predicted value
 ● Design points below predicted value
 0.0267653
 -0.197724
 X1 = B: Velocity
 X2 = C: L1 and R1
 Actual Factor
 A: A-o-A = 8

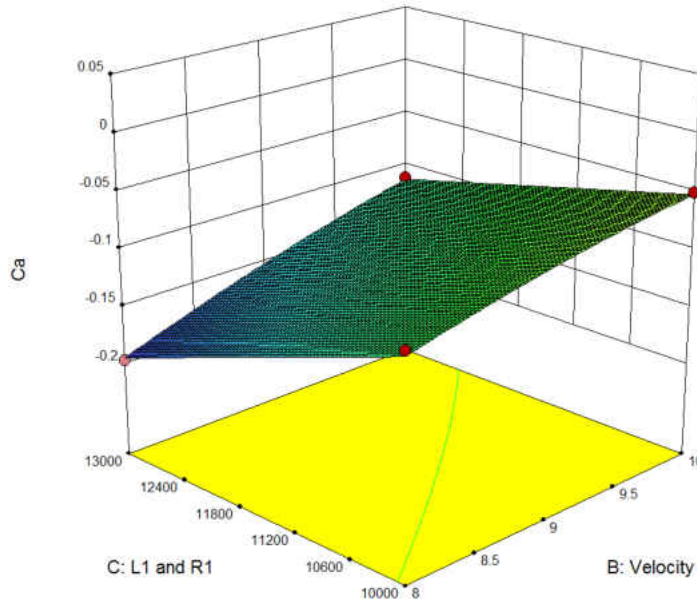


Figure 54. Response surface for wing-tip-propellers-alone C_A at eight angle of attack`

Although the C_N model has no interaction term with L1 and R1, the C_A model has a significant interaction term between velocity and L1 and R1, which is expected due to the induced drag reduction.

Design-Expert® Software
 Factor Coding: Actual
 Ca
 ● Design Points
 — 95% CI Bands
 X1 = B: Velocity
 X2 = C: L1 and R1
 Actual Factor
 A: A-o-A = 4
 C- 10000
 C+ 13000

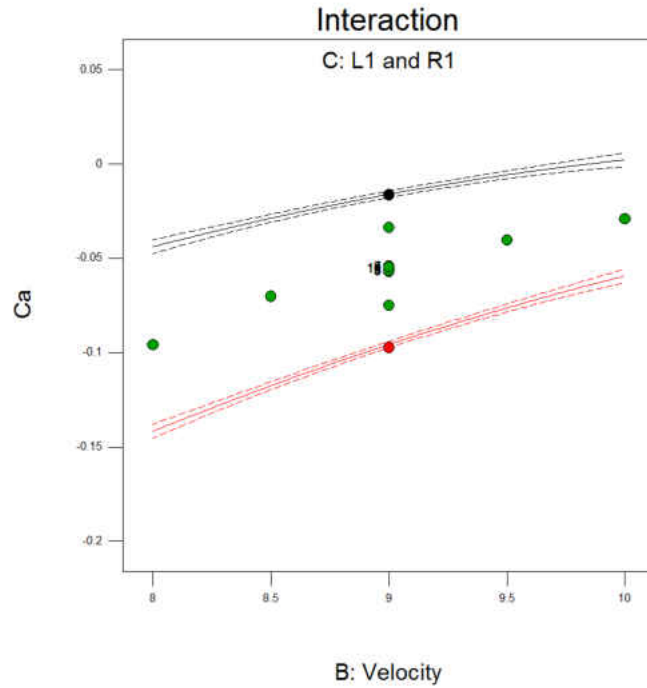


Figure 55. C_A as a function of velocity and L1 and R1 for wing-tip-propellers-alone mode

The results of the confirmation point measurements are shown in Table 31. All confirmation point results fell into the 95% prediction interval. Thus, the model adequately represents the observed data.

Run		95%PI Low	Predicted	Measured	95%PI High
1	C _A	-0.068	-0.062	-0.061	-0.056
2		-0.057	-0.051	-0.052	-0.046
3		-0.138	-0.132	-0.131	-0.126
4		-0.071	-0.066	-0.062	-0.061
5		-0.071	-0.066	-0.066	-0.060
6		-0.097	-0.091	-0.090	-0.085

Table 31. Prediction capability of the wing-tip-propellers-alone C_A model

5.5 Wing-Tip-Propellers-Alone and Two-Inboard-Propellers-Alone Comparison

Experiments were performed on the wing-tip-propellers-alone and two-inboard-propellers-alone modes to observe the effect of the wing-tip-propellers configuration on induced

drag at low Reynolds numbers. Data was taken at 9 m/s free-stream velocity, 11500 rpm level conditions at specified angles-of-attack (2-4-6-8 degrees) with three replicates. Experimental results show that the wing-tip propellers model had low drag with increasing angle of attack at the low Reynolds number of 86000, as seen in the figure below (Snyder, 1967).

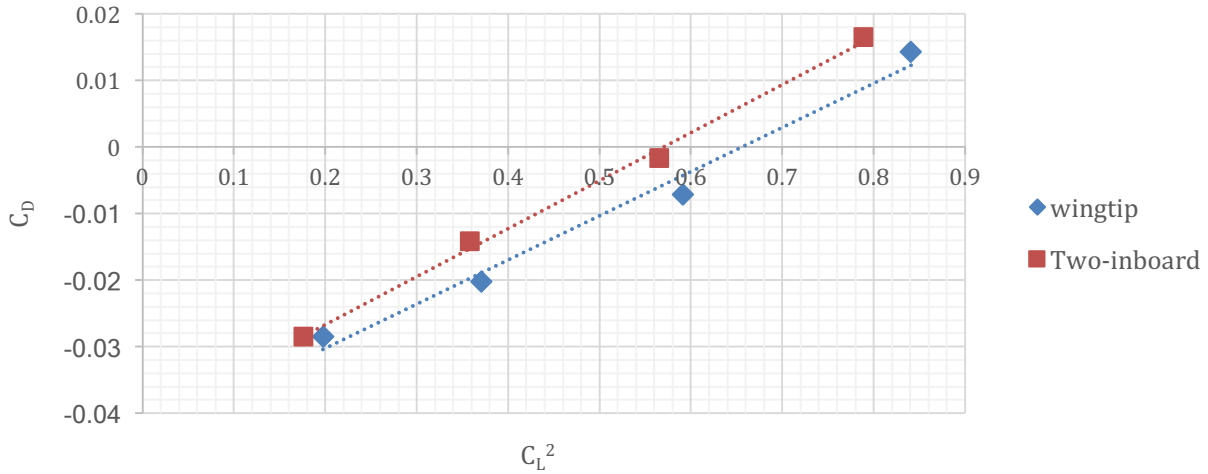


Figure 56. C_D vs C_L^2

Induced drag reduction is separated from total drag by using the equation below (Snyder, 1967),

$$C_D = C_{D_p} + mC_L^2 \quad (51)$$

where C_{D_p} is the parasitic drag term, mC_L^2 is the induced drag term, and m is the slope of the C_D vs C_L^2 plots.

$$m = \frac{dC_D}{dC_L^2} \quad (52)$$

The induced drag contribution to drag reduction is shown in Figure 57. Although the wingtip-propellers mode had lower induced drag with increasing angle of attack, the amount of reduction could be enhanced through the use of larger diameter and optimally designed propellers.

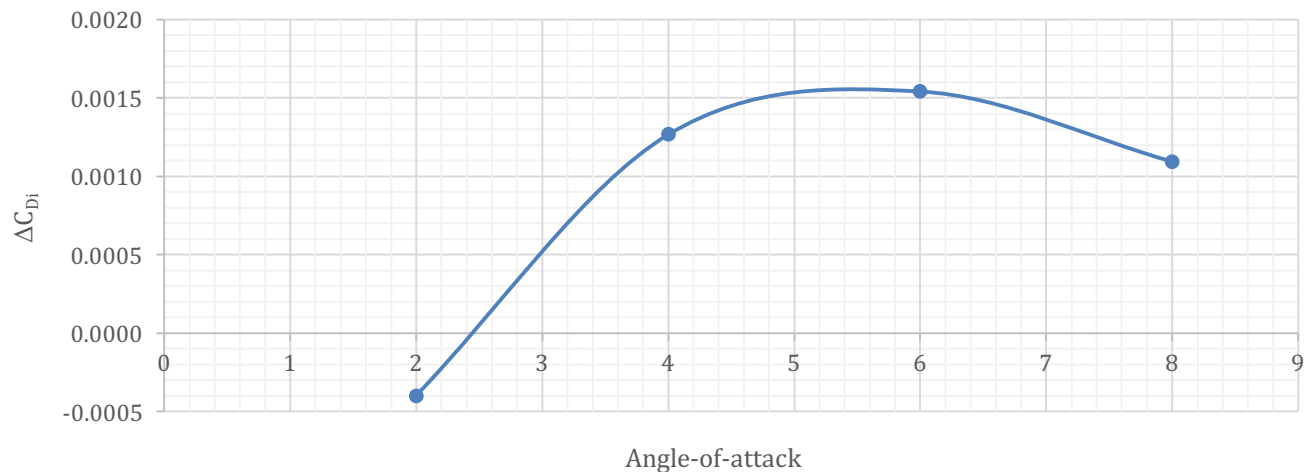


Figure 57. Induced drag difference between two-inboard and wingtip propellers mode

5.6 Single-Tractor Mode

The single-tractor mode was analyzed in the VSPAERO vortex lattice code. This software program includes a propeller thrust feature to analyze different propeller-wing combinations. The actuator disk was used for propeller modelling.

Initially, all-propeller-on and wing-alone configurations were analyzed in this program for validation of numerical results with experimental results. The experimentally determined regression models were used to determine the experimental lift coefficient (C_L) changes at 9 m/s free-stream velocity, 11500 RPM and 0 - 8 degree angle-of-attack flight conditions. Lift coefficient vs. angle of attack was compared. Experimental and computational results demonstrated close agreement and identical trends.

Computational models and experimental results comparison are shown in the figures below.

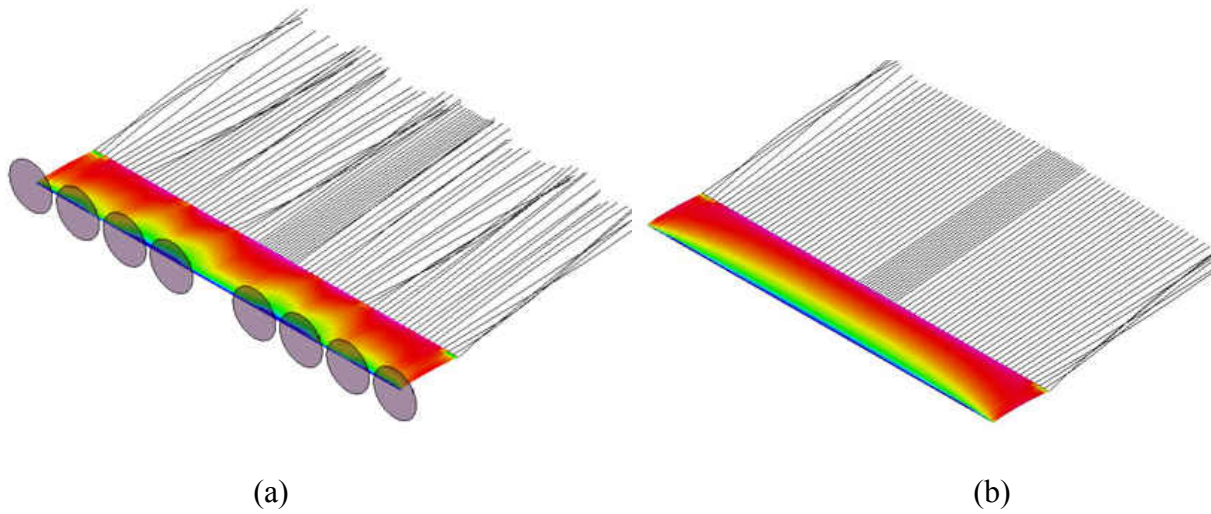


Figure 58. VSPAERO models (a) distributed propulsion (b) wing-alone

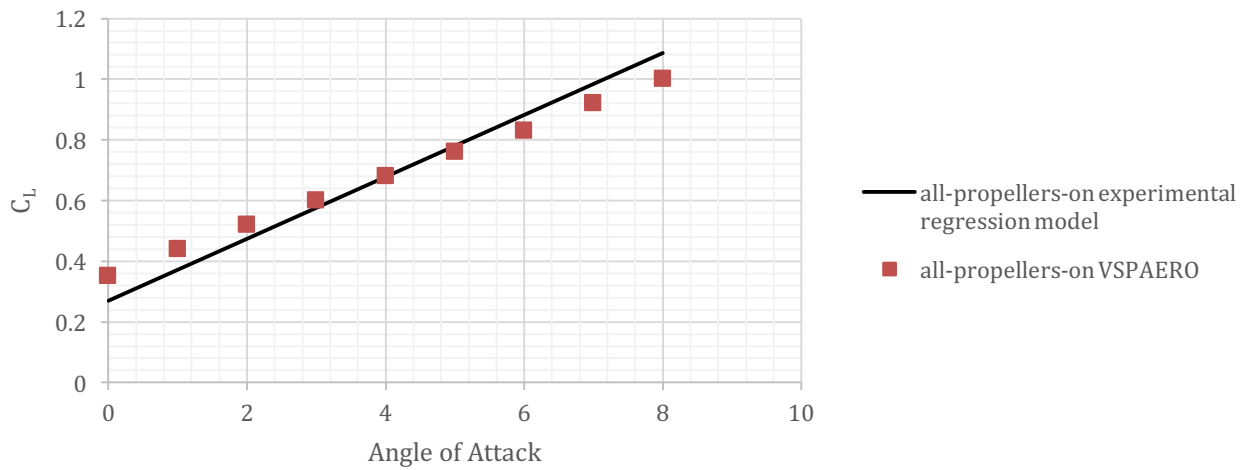


Figure 59. Distributed propulsion VSPAERO and experimental results

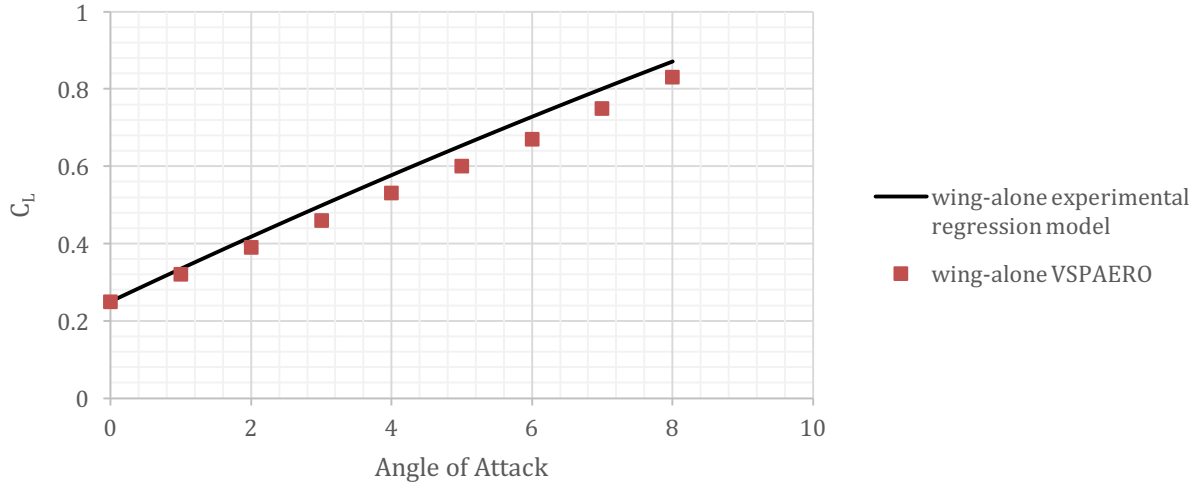


Figure 60. Wing-alone VSPAERO and experimental results

Thrust equality (to the distributed counterpart) was considered for the single-tractor model design at identical flight conditions for each mode of the wind tunnel experiments. Therefore, a GWS 9.0 x 5.0 propeller was chosen from the University of Illinois at Urbana Champaign Propeller Data Base (Deters et al., 2014). The propeller was then modelled with a 9-inch diameter and 0.04 thrust coefficient at 9 m/s free stream velocity in VSPAERO, as shown in Figure 60. Computational results demonstrated close agreement and identical trends with the wing-alone-mode experimental results, as is illustrated in Figure 61. This result supports the use of the wing-alone mode experimental results as a single-tractor mode for making a trade-study between distributed propulsion and single-tractor propulsion concepts.

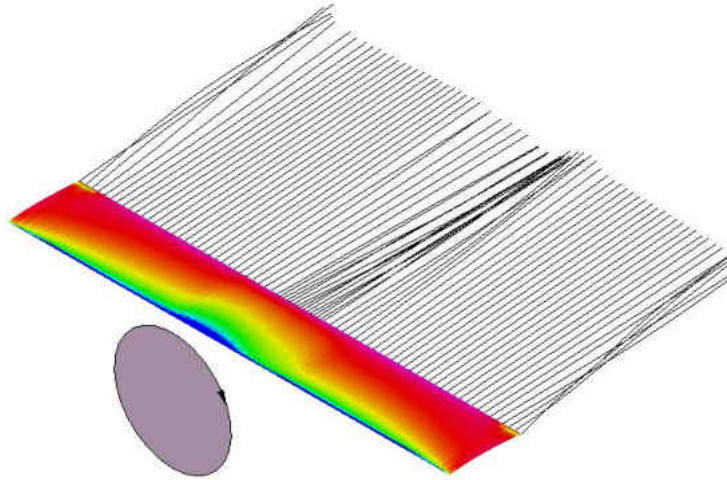


Figure 61. VSPAERO single-tractor

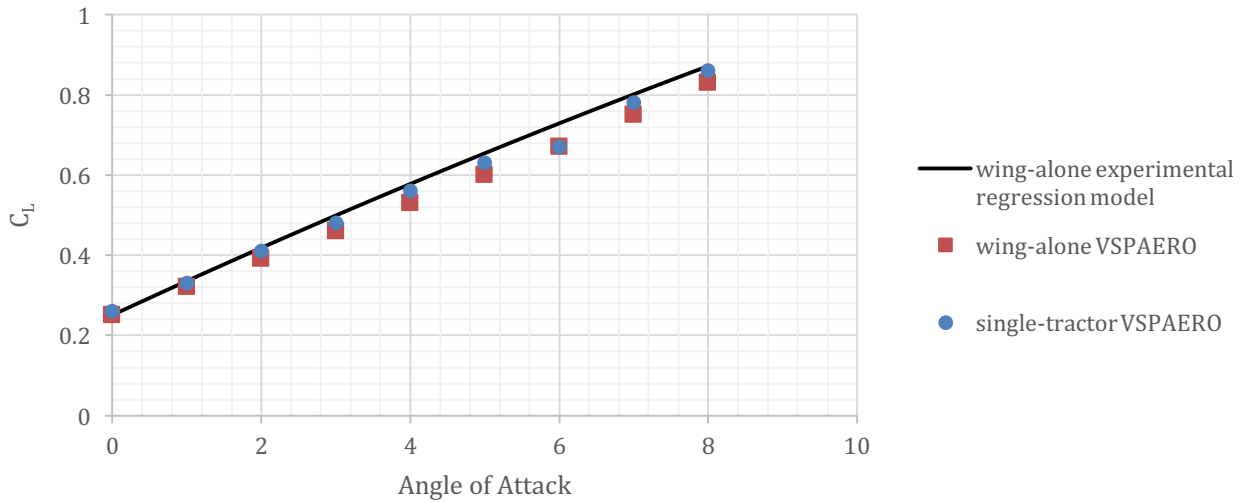


Figure 62. Experimental and VSPAERO results for wing-alone and single-tractor

Experimental results were corrected based on Barlow et al. (1999) as illustrated in the Appendix.

CHAPTER 6

TRADE STUDY

An initial trade study between distributed propulsion and single-tractor concepts was based on the relationship between normal force increment (ΔC_N) due to using distributed propulsion (over single tractor) and weight penalty.

The normal force coefficient increment between these concepts is shown in the tables below for take-off (all-propellers-on vs. single-tractor) and cruise (wing-tip-propellers-alone vs. single-tractor) modes at the maximum RPM level.

ΔC_N Take-Off		
ΔC_N	A-o-A	Velocity
0.068	0	8
0.162	4	8
0.290	8	8
0.045	0	9
0.120	4	9
0.230	8	9
0.022	0	10
0.079	4	10
0.170	8	10

Table 32. C_N increment for take-off

ΔC_N Cruise		
ΔC_N	A-o-A	Velocity
0.026	0	8
0.046	4	8
0.073	8	8
0.023	0	9
0.037	4	9
0.058	8	9
0.020	0	10
0.028	4	10
0.042	8	10

Table 33. C_N increment for cruise

Although the distributed propulsion system has higher normal force for each flight mode, as seen above, the weight penalty vs. normal force was investigated in this study to draw a fair conclusion about the benefits of a distributed propulsion system. The weight of components for both modes is illustrated in Tables 34 and 35. While this accounting is for this specific model, it is felt to be representative and, most likely, conservative.

Distributed Electric Propulsion	
8 motors (Medusa MR-012-030-4000)	112 g
8 propellers (GWS 4.0x2.5)	12 g
8 ESC	64 g
8 prop-adapters	12 g
8 motor mounts	40 g
Wing core	340 g
Total Weight	580 g

Table 34. Distributed propulsion total weight

Single-Tractor Propulsion	
1 motor (Astro 020 Planetary System 803P)	122 g
1 propeller (GWS 9.0x5.0)	10 g
1 ESC	17 g
1 prop-adapter	6.7 g
Wing core	348 g
Total Weight	503.7 g

Table 35. Single-tractor propulsion total weight

Due to the high number of components, the distributed electric propulsion system is heavier than the single-tractor propulsion system. Also, wiring weight was assumed to be the same for both models. To make a comparison between these concepts, the normal force (N) value was calculated for different wing chord based Reynolds numbers at different angles-of-attack and maximum RPM. Then, the ratio of normal force and total weight was plotted versus angle of attack for take-off/landing and cruise modes, as seen in Figures 62 and 63.

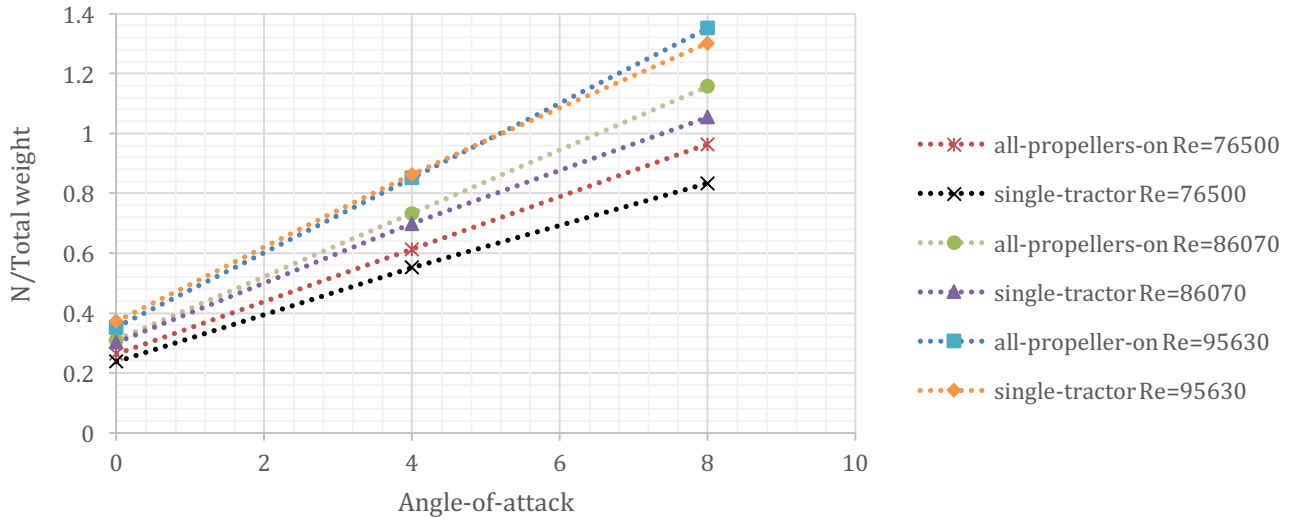


Figure 63. Weight effect on take-off configurations

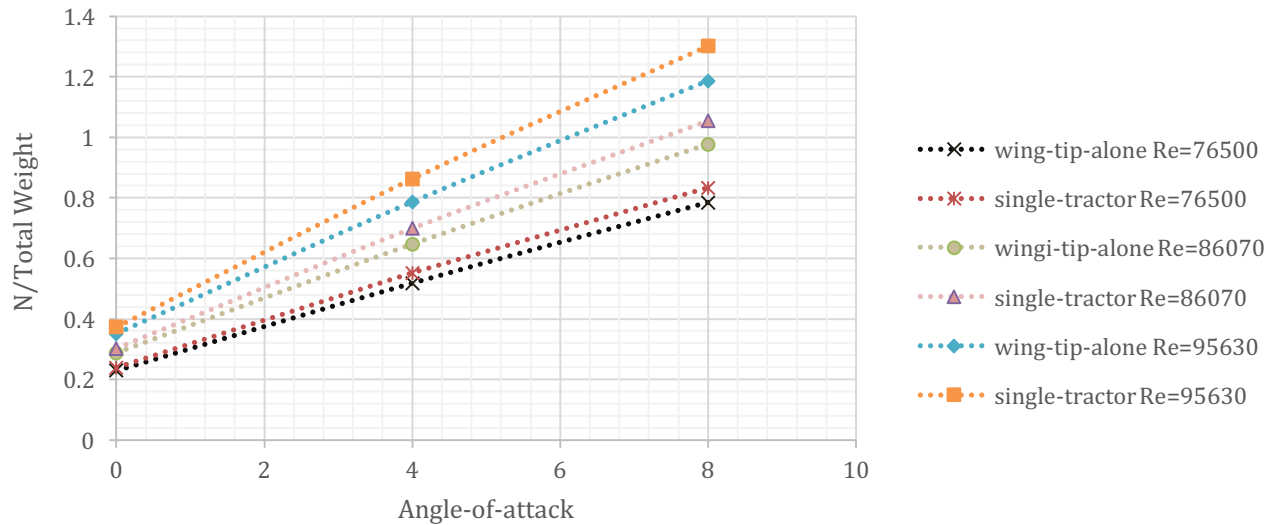


Figure 64. Weight effect on cruise configurations

Results show that distributed propulsion system had a higher normal force to total weight ratio value with increasing angle-of-attack at each Reynolds number for the take-off mode. This ratio difference was reduced with increasing Reynolds numbers. The single-tractor propulsion

system had a higher normal force to total weight ratio value at each Reynolds number for the cruise mode. This ratio difference increased with increasing Reynolds numbers. These results suggest that larger propellers should be used at the wing-tips (Patterson, 2016) and that the normal force to total weight ratio value increased with increasing Reynolds numbers at each flight mode.

Range and endurance performance were compared based on the Breguet equations developed for electric aircraft (Patterson, German, & Moore, 2012). Range and endurance equations are shown in equations (53) and (54).

$$Range = \eta \frac{L}{D} \frac{W_{bat}}{W} \frac{uk}{g} \quad (53)$$

$$Endurance = \frac{\eta}{V} \frac{L}{D} \frac{W_{bat}}{W} \frac{uk}{g} \quad (54)$$

where W_{bat} is a weight of batteries, W is a total weight, u is a battery energy density, k is a measure of the percent charge of the batteries, g is a center of gravity for constant acceleration, η is an overall efficiency of motor-propeller combination and L/D is a lift and drag ratio.

Experimental lift and drag force values were used to compute the L/D ratio for both configurations. Wing-alone mode lift values were used for single-tractor mode as explained in section 5.6. Also, drag was assumed same for both modes, which was experimental wing-alone drag. The L/D ratios are plotted (all-propellers-on mode vs. single tractor) in Figures 65-67 at different Re numbers.

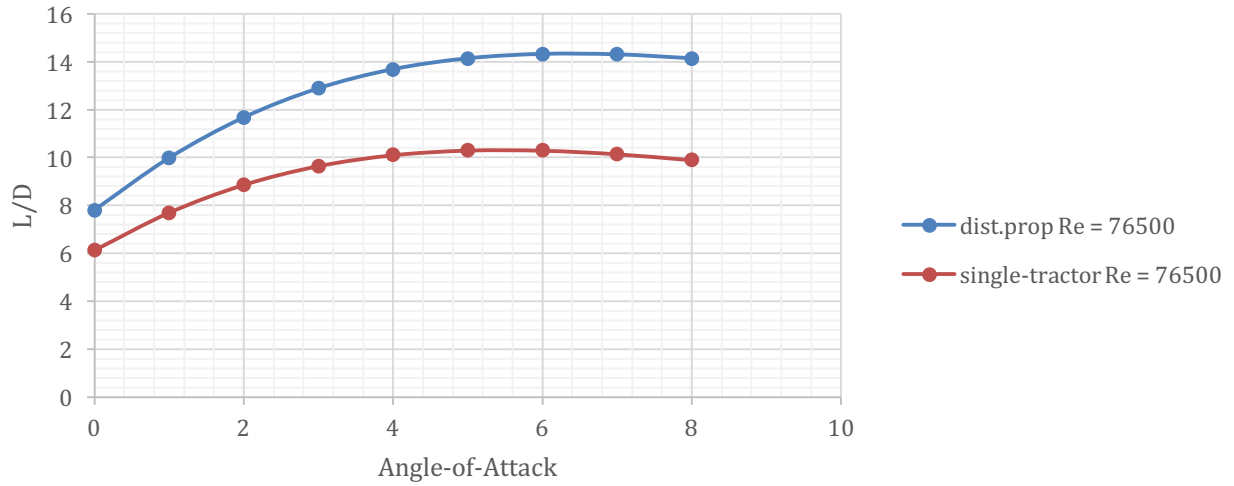


Figure 65. L/D Re = 76500

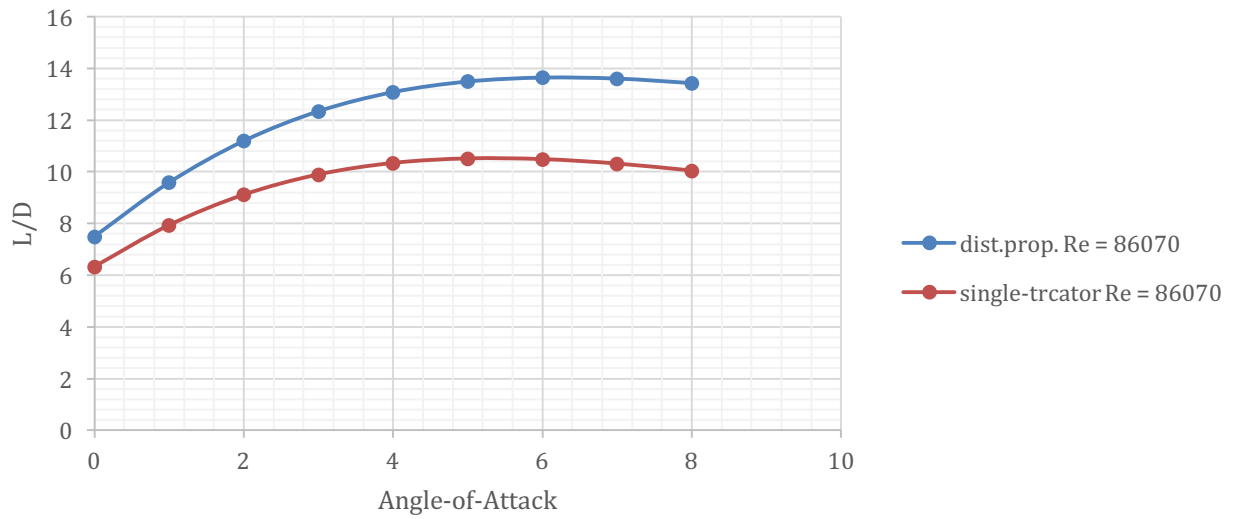


Figure 66. L/D Re = 86070

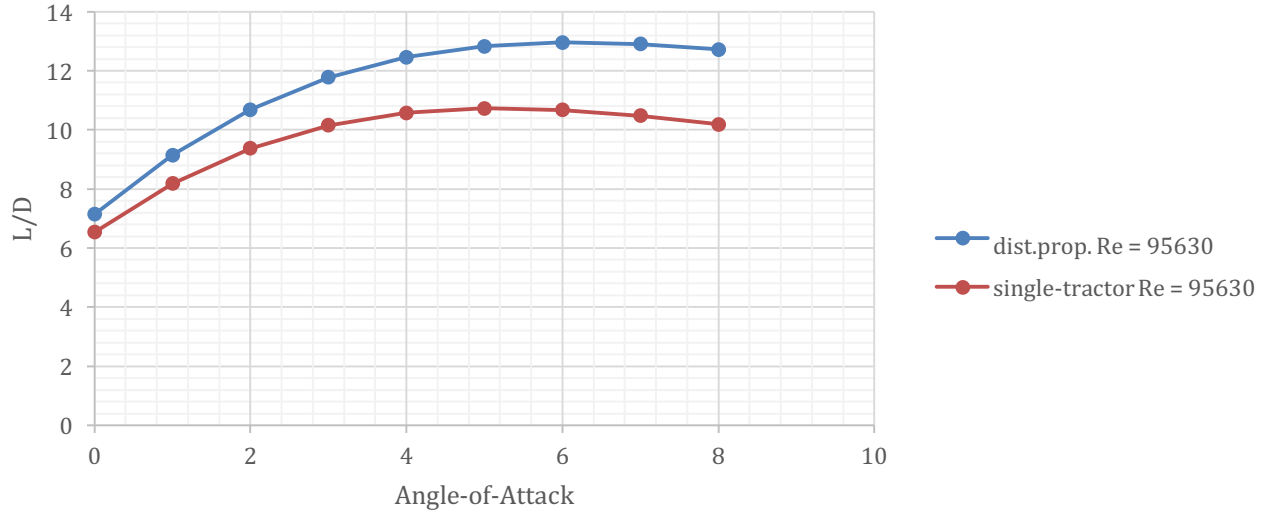


Figure 67. L/D Re = 95630

Also, η was calculated based on motor-propeller efficiency (Deters et al., 2014) at different velocities as shown in Table 36. Propeller efficiency was based on thrust to power ratio and electrical efficiency was based on efficiency of the batteries, motor controller and motor (Patterson et al., 2012). Electrical efficiency was assumed to be the same for both aircraft configurations.

$$\eta = \eta_{prop} \eta_{elec} \quad (55)$$

	Distributed Propulsion			Single Tractor		
	V = 8 m/s	V = 9 m/s	V = 10 m/s	V = 8 m/s	V = 9 m/s	V = 10 m/s
η	0.56	0.6	0.58	0.51	0.56	0.6

Table 36. Overall efficiency

The same battery specifications were used for both configurations.

Finally, range and endurance results were plotted at three different constant velocities and at an angle of attack of three degrees.

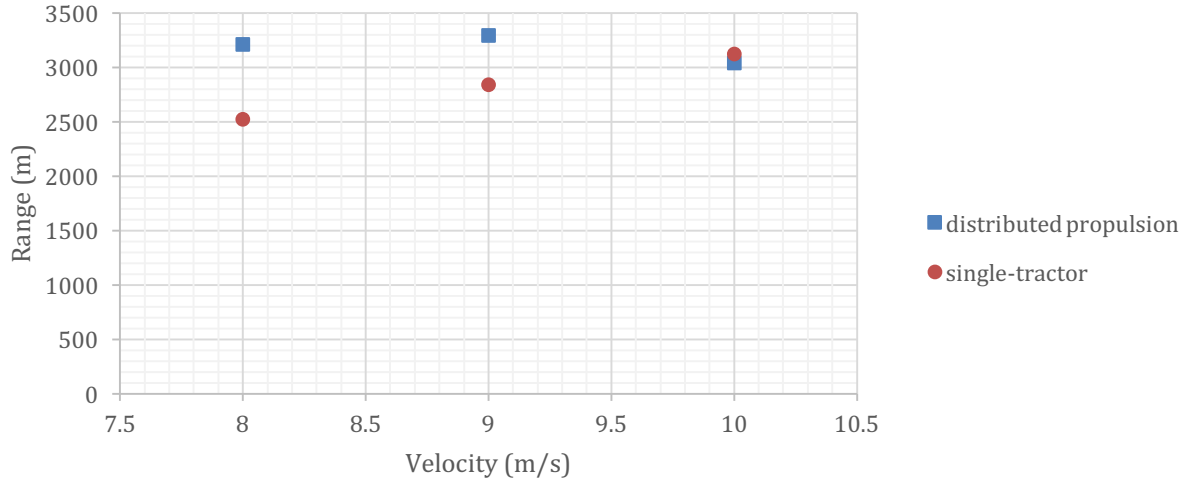


Figure 68. Range

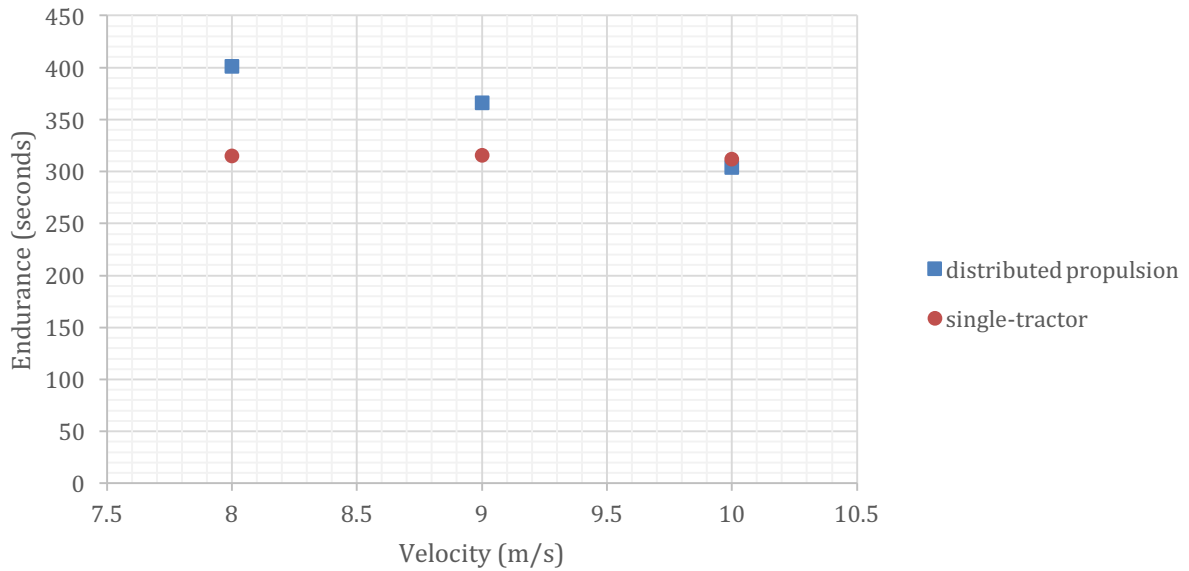


Figure 69. Endurance

CHAPTER 7

CONCLUSIONS

The aerodynamic comparison of a distributed propulsion system and single-tractor propulsion system at low Reynolds numbers was evaluated in this study. Experiments were conducted with DOE methodology for aerodynamic characterization. Additionally, VSPAERO vortex lattice code was used for trade studies. Results demonstrated the potential benefits of the distributed propulsion system at low Reynolds numbers.

The normal force increment and reduction in induced drag was demonstrated as the primary gain afforded due to using a distributed propulsion system. Compared to a single tractor propeller system, assuming that both propulsion systems have equivalent thrust, the distributed propulsion system showed a higher C_N value, presumably due to the higher local dynamic pressure around the wing in the propeller wake. Low chord Reynolds numbers were raised locally due to the increased velocity, which should have provided a further benefit. Wing-tip propellers were shown to reduce induced drag by opposing the wing tip vortex circumferential velocity direction (Miranda & Brennan, 1986). The distributed propulsion system had better range and endurance performance due to the higher L/D ratio when based on the same available power.

The weight penalty appeared to be the main disadvantage for the distributed propulsion system used in this research. However, the specific distributed propulsion system was constructed from off-the-shelf hobby-grade components that were not optimized. Therefore, lightweight materials are recommended in future work. Next, the propellers were not specifically designed for high lift (inboard) or cruise (tip). Large propellers can be used at the

wing tips to provide better aerodynamic performance in the cruise mode (Patterson, 2016). High-lift propellers can be designed for maximum circulation (Patterson, 2016). Additionally, optimal placement of the propellers' position/size and adjacent spacing is a subject for future experiments. The small scale of the model dictated the use of relatively low performance hobby propellers. Also, wing area reduction has been successfully demonstrated in larger scale and could be considered in future small UAV designs to provide important weight and drag reduction (Stoll, Bevirt, Moore, et al., 2014). Despite significant progress in understanding of distributed propulsion aerodynamics, the distributed electric propulsion technology will be more valuable when matched with future battery technology improvements.

REFERENCES

- Bagai, A. (2016). *Vertical takeoff and landing experimental plane (VTOL X-Plane)*. Retrieved from <http://www.darpa.mil/program/vertical-takeoff-and-landing-experimental-plane>
- Barlow, J. B., Rae, W. H., & Pope, A. (1999). *Low-speed wind tunnel testing* (3th ed.). New Jersey, NJ: John Wiley & Sons Inc.
- Barnstorff, K. (2015). *Future aircraft*. Retrieved from <http://www.nasa.gov/langley/ten-engine-electric-plane-completes-successful-flight-test>
- Borer, N. K., Patterson, M. D., Viken, J. K., Moore, M. D., Clarke, S., Redifer, M. E., ... Osterkamp, P. G. (2016). Design and performance of the NASA SCEPTOR distributed electric propulsion flight demonstrator. In *16th AIAA Aviation Technology, Integration, and Operations Conference*.
- Box, G. E. P., & Wilson, K. B. (1951). On the experimental attainment of optimum condition. *Journal of the Royal Statistical Society*, 13, 1-45
- Coleman, H. W., & Steele, W. G. (2009). *Experimentation, validation, and uncertainty analysis for engineers* (3rd ed.). New Jersey, NJ: John Wiley & Sons Inc.
- Deters, R. W., Ananda, G. K., & Selig, M. S. (2014). Reynolds number effects on the performance of small-scale propellers. In *32nd AIAA Applied Aerodynamics Conference, American*.
- Deters, R. W., & Selig, M. S. (2008). Static testing of micro propellers. In *26th AIAA Applied Aerodynamics Conference*.
- Dubois, A., van der Geest, M., Bevirt, J., Clarke, S., Christie, R. J., & Borer, N. K. (2016). Design of an electric propulsion system for SCEPTOR's outboard nacelle. In *16th AIAA Aviation Technology, Integration, and Operations Conference*.

- Fisher, R. A. (1935). *The Design of Experiments* (1st ed.). New York, NY: Hafner Publishing Company.
- Gohardani, A. S. (2013). A synergistic glance at the prospects of distributed propulsion technology and the electric aircraft concept for future unmanned air vehicles and commercial/military aviation. *Progress in Aerospace Sciences*, 57, 25–70.
- Gohardani, A. S., Doulgeris, G., & Singh, R. (2011). Challenges of future aircraft propulsion: A review of distributed propulsion technology and its potential application for the all-electric commercial aircraft. *Progress in Aerospace Sciences*, 47(5), 369–391.
- Jane's All The World's Aircraft Homepage (2016). *All sections search engine*. Retrieved from www.janes.com
- Ko, Y.-Y. A. (2003). *The multidisciplinary design optimization of a distributed propulsion blended-wing-body aircraft*. Virginia Polytechnic Institute and State University, Virginia, VA.
- Kummer, J. (2010). *Propulsive wing aerial utility vehicle development*. Retrieved from <http://www.propulsivewing.com/index.shtml>
- Landman, D., Simpson, J., Mariani, R., Ortiz, F., & Britcher, C. (2007). Hybrid design for aircraft wind-tunnel testing using response surface methodologies. *Journal of Aircraft*, 44(4), 1214–1221.
- Lyon, C. A., Broeren, A. P., Giguere, P., Gopalarathnam, A., & Selig, M. S. (1997). *Summary of low-speed airfoil data* (3th ed.). Virginia, VA: SoarTech Publications.
- Mark D. Moore, Nicholas K. Borer, Bill Frederics, Daniel Palumbo, Steve Rizzi, Doug Nark, ... Brian German. (2014). *Leading Edge Distributed Electric Propulsion Wing Integration for CTOL, STOL and VTOL Missions*. Presented at AIAA Aviation Forum.

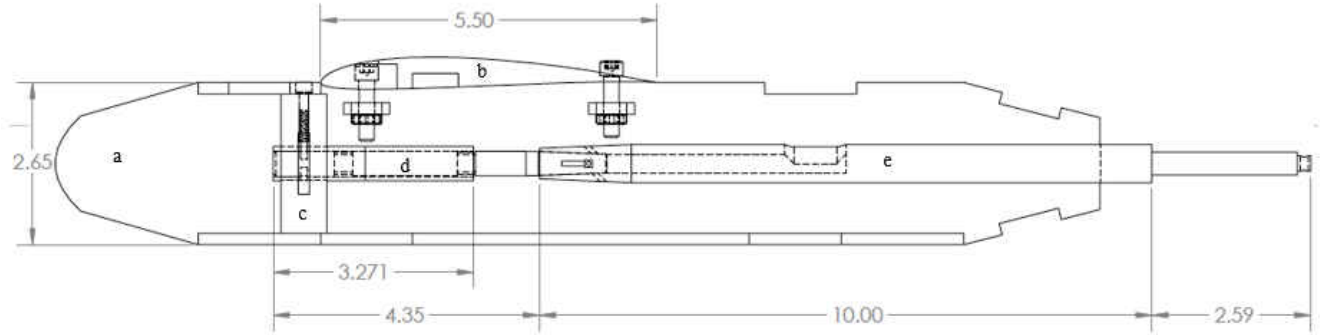
- Miranda, L. R., & Brennan, J. E. (1986). Aerodynamic effects of wingtip-mounted propellers and turbines. In *4th AIAA Applied Aerodynamics Conference*.
- Montgomery, D. C. (2013). *Design and analysis of experiments* (8th ed.). New Jersey, NJ: John Wiley & Sons Inc.
- Moore, M. D., & Fredericks, B. (2014). Misconceptions of electric propulsion aircraft and their emergent aviation markets. In *52nd Aerospace Sciences Meeting*.
- Moore, M. D., Goodrich, K., Viken, J., Smith, J., Fredericks, B., Trani, T.,... Patterson, M. (2013). High-speed mobility through on-demand aviation. In *Aviation Technology, Integration, and Operations Conference*.
- Murphy, P. C., & Landman, D. (2015). Experiment design for complex VTOL aircraft with distributed propulsion and tilt wing. In *AIAA Atmospheric Flight Mechanics Conference*.
- Myers, R. H., Montgomery, D. C., & Anderson-Cook, Christine M. (2009). *Response surface methodology* (3rd ed.). New Jersey, NJ: John Wiley & Sons Inc.
- National Research Council. (2006). *A Review of United States Air Force and Department of Defense Aerospace Propulsion Needs* (1st ed.). Air Force Studies Board. Division on Engineering and Physical Sciences. Washington, DC: National Academies Press.
- Patterson, M. D. (2016). *Conceptual Design of High Lift Propeller Systems for Small Electric Aircraft*. Georgia Institute of Technology, Georgia, GA.
- Patterson, M. D., German, B. J., & Moore, M. D. (2012). Performance analysis and design of on-demand electric aircraft concepts. *12th AIAA Aviation Technology, Integration and Operations Conference*.

- Perry, A. T., Ansell, P. J., Kerho, M., Ananda, G., & D'Urso, S. (2016). Design, analysis, and evaluation of a propulsive wing concept. In *34th AIAA Applied Aerodynamics Conference*.
- Philips, B. D. (2016, June). *Design of Experiments Enhanced Statistical Process Control for Wind Tunnel Check Standard Testing*. Old Dominion University, Virginia, VA.
- Rothhaar, P. M., Murphy, P. C., Bacon Barton, J., Gregory, I. M., Grauer, J. A., Busan, R. C., & Croom, M. A. (2014). NASA Langley distributed propulsion VTOL tilt-wing aircraft testing, modeling, simulation, control, and flight test development. In *14th AIAA Aviation Technology, Integration, and Operations Conference*.
- Schetz, J. A., Hosder, S., Dippold, V., & Walker, J. (2010). Propulsion and aerodynamic performance evaluation of jet-wing distributed propulsion. *Aerospace Science and Technology, 14*(1), 1–10.
- Sehra, A. K., & Whitlow, W. (2004). Propulsion and power for 21st century aviation. *Progress in Aerospace Sciences, 40*(4), 199–235.
- Sheller, C. (2016a). Aurora successfully flies subscale X-Plane aircraft. Retrieved from <http://www.aurora.aero/wp-content/uploads/2016/04/LightningStrike-VTOL-X-Plane-Subscale-Model-First-Flight.pdf>
- Sheller, C. (2016b). Aurora's revolutionary aircraft design includes the first-ever distributed hybrid-electric propulsion system. Retrieved from <http://www.multivu.com/players/English/7617851-aurora-flight-sciences-vtol-xplane-darpa/>
- Snyder, M. H. (1967). *Effects of a Wingtip-Mounted Propeller on Wing Lift, Induced Drag and Shed Vortex Pattern*. Oklahoma State University, Oklahoma, OK.

- Stoll, A. M. (2015). Comparison of CFD and experimental results of the LEAPTech distributed electric propulsion blown wing. In *15th AIAA Aviation Technology, Integration, and Operations Conference*.
- Stoll, A. M., Bevirt, J., Moore, M. D., Fredericks, W. J., & Borer, N. K. (2014). Drag reduction through distributed electric propulsion. In *14th AIAA Aviation Technology, Integration and Operations Conference*.
- Stoll, A. M., Bevirt, J., Pei, P. P., & Stilson, E. V. (2014). Conceptual design of the Joby S2 electric VTOL PAV. In *14th AIAA Aviation Technology, Integration, and Operations Conference*.
- Stoll, A. M., & Mikic, G. V. (2016). Design studies of thin-haul commuter aircraft with distributed electric propulsion. In *16th AIAA Aviation Technology, Integration and Operation Conference*.

APPENDICES

APPENDIX A Model Assembly Technical Drawing



All dimensions are in inches.

a: Fuselage

b: Wing

c: Aluminum bulkhead

d: Balance

e: Balance support

APPENDIX B 2044A Force Balance Specifications

***** N A S A *****
 ***** Langley Research Center *****

STRAIN GAGE BALANCE CALIBRATION RESULTS

FINAL FINAL
 Balance: 2044A Engineer: Tom Stokes
 Calibration Date: 10/19/06

Component	Calibration Load Range		Full Scale Output (mV/V)	Sensitivity Constant		Accuracy % F.S. (95 % Conf.)
	(lb or in-lb)	(N or Nm)		(lb/mV/V) or (in-lb/mV/V)	(N/mV/V) or (Nm/mV/V)	
1 NORMAL	70.0 -70.0	311.376 -311.376	1.664	42.0578	187.0824	0.05
2 AXIAL	15.0 -15.0	66.723 -66.723	1.064	14.0933	62.6901	0.10
3 PITCH	70.0 -70.0	7.909 -7.909	1.761	39.7539	4.4916	0.07
4 ROLL	15.1 -15.1	1.700 -1.700	0.676	22.2690	2.5161	0.61
5 YAW	25.0 -25.0	2.825 -2.825	1.167	21.4279	2.4210	0.18
6 SIDE	25.0 -25.0	111.206 -111.206	1.200	20.8329	92.6693	0.10

MOMENT CENTER = 1.65 INCHES AFT OF FORWARD DOWEL
 BALANCE EXCITATION: 5.000 volts
 DELTA W: 0.0000E+0 lbs
 SPECIAL REMARKS: Man

SVS Calibration. FS RM = 15.05 in-lb.



APPENDIX C All-Propellers-On Mode Actual Text Matrix

Run Number	A-o-A	V(m/s)	L1	L2	L3	L4	C _N	C _A
1	8	10	10000	10000	10000	10000	0.911157	-0.11647
2	0	10	13000	10000	10000	10000	0.238458	-0.09587
3	4	9	11500	11500	11500	11500	0.654903	-0.28065
4	4	9	11500	11500	11500	10000	0.645567	-0.24351
5	4	9	11500	11500	11500	11500	0.66017	-0.27996
6	4	9	11500	11500	11500	11500	0.657927	-0.28161
7	0	8	10000	13000	10000	10000	0.265674	-0.3168
8	8	8	13000	13000	13000	13000	1.16271	-0.67571
9	8	10	10000	13000	13000	13000	1.0128	-0.2856
10	0	8	10000	10000	10000	13000	0.265487	-0.32173
11	4	9	11500	13000	11500	11500	0.662039	-0.31809
12	8	10	13000	10000	13000	10000	0.979245	-0.23296
13	4	9	11500	11500	10000	11500	0.635041	-0.24399
14	0	10	10000	13000	10000	13000	0.229535	-0.15369
15	8	9	11500	11500	11500	11500	1.04078	-0.34448
16	4	9	10000	11500	11500	11500	0.638151	-0.24187
17	4	10	11500	11500	11500	11500	0.61157	-0.17138
18	4	9	11500	11500	13000	11500	0.667781	-0.31377
19	4	9	11500	11500	11500	11500	0.655694	-0.28209
20	4	9	13000	11500	11500	11500	0.669801	-0.31739
21	0	8	13000	10000	13000	13000	0.305131	-0.49528
22	8	8	10000	13000	10000	13000	1.09231	-0.49917
23	4	8	11500	11500	11500	11500	0.705389	-0.44074
24	8	8	10000	13000	13000	10000	1.08805	-0.49413
25	0	10	10000	10000	13000	13000	0.239341	-0.14763
26	0	9	11500	11500	11500	11500	0.265828	-0.25306
27	0	8	13000	13000	13000	10000	0.307527	-0.49071
28	8	10	13000	10000	10000	10000	0.941638	-0.16844
29	8	10	13000	13000	10000	10000	0.965826	-0.22193
30	0	10	13000	13000	13000	13000	0.270489	-0.2438
31	4	9	11500	11500	11500	11500	0.636581	-0.23418
32	4	9	11500	10000	11500	11500	0.654828	-0.25833
33	0	8	13000	13000	10000	13000	0.308678	-0.5101
34	4	9	11500	11500	11500	13000	0.678519	-0.32889
35	8	8	10000	10000	13000	13000	1.10338	-0.51027
36	0	8	10000	10000	13000	10000	0.271153	-0.3329
37	4	9	11500	11500	11500	11500	0.65898	-0.29171

Run Number	A-o-A	V(m/s)	L1	L2	L3	L4	C _N	C _A
38	8	10	13000	10000	10000	13000	0.989024	-0.2456
39	8	8	13000	10000	10000	10000	1.06848	-0.43199
40	0	10	10000	13000	13000	10000	0.243737	-0.15218
41	6	9.5	10750	10750	10750	10750	0.805542	-0.18875
42	2	9.5	12250	10750	10750	10750	0.435889	-0.18403
43	4	9	11500	11500	11500	11500	0.661623	-0.29304
44	4	9	11500	11500	11500	10750	0.652365	-0.2743
45	4	9	11500	11500	11500	11500	0.660209	-0.29103
46	4	9	11500	11500	11500	11500	0.661952	-0.2946
47	2	8.5	10750	12250	10750	10750	0.470297	-0.2991
48	6	8.5	12250	12250	12250	12250	0.903559	-0.45885
49	6	9.5	10750	12250	12250	12250	0.841833	-0.28589
50	2	8.5	10750	10750	10750	12250	0.462189	-0.30049
51	4	9	11500	12250	11500	11500	0.667854	-0.30696
52	6	9.5	12250	10750	12250	10750	0.834241	-0.25771
53	4	9	11500	11500	10750	11500	0.642423	-0.27507
54	2	9.5	10750	12250	10750	12250	0.438511	-0.21394
55	6	9	11500	11500	11500	11500	0.854618	-0.31686
56	4	9	10750	11500	11500	11500	0.655342	-0.2702
57	4	9.5	11500	11500	11500	11500	0.642777	-0.23131
58	4	9	11500	11500	12250	11500	0.666076	-0.31046
59	4	9	11500	11500	11500	11500	0.655105	-0.2891
60	4	9	12250	11500	11500	11500	0.661576	-0.31015
61	2	8.5	12250	10750	12250	12250	0.487622	-0.38133
62	6	8.5	10750	12250	10750	12250	0.875673	-0.38412
63	4	8.5	11500	11500	11500	11500	0.693288	-0.36079
64	6	8.5	10750	12250	12250	10750	0.885375	-0.37902
65	2	9.5	10750	10750	12250	12250	0.443626	-0.20887
66	2	9	11500	11500	11500	11500	0.469742	-0.27354
67	2	8.5	12250	12250	12250	10750	0.487639	-0.37149
68	6	9.5	12250	10750	10750	10750	0.817933	-0.22441
69	6	9.5	12250	12250	10750	10750	0.823863	-0.25953
70	2	9.5	12250	12250	12250	12250	0.467238	-0.27502
71	4	9	11500	11500	11500	11500	0.655949	-0.28695
72	4	9	11500	10750	11500	11500	0.655515	-0.27196
73	2	8.5	12250	12250	10750	12250	0.48682	-0.37836
74	4	9	11500	11500	11500	12250	0.676266	-0.30527
75	6	8.5	10750	10750	12250	12250	0.884032	-0.37874
76	2	8.5	10750	10750	12250	10750	0.465375	-0.29669

Run Number	A-o-A	V(m/s)	L1	L2	L3	L4	C _N	C _A
77	4	9	11500	11500	11500	11500	0.661836	-0.28782
78	6	9.5	12250	10750	10750	12250	0.837175	-0.25636
79	6	8.5	12250	10750	10750	10750	0.866123	-0.35248
80	2	9.5	10750	12250	12250	10750	0.444655	-0.20731

APPENDIX D Wing-Alone Mode Actual Text Matrix

Run Number	A-o-A	V(m/s)	C _N	C _A
1	4	10	0.580754	0.015433
2	0	9	0.24446	0.038629
3	4	9	0.582542	0.017544
4	0	8	0.25667	0.043524
5	4	9	0.579845	0.016238
6	4	9	0.588075	0.019134
7	0	10	0.254011	0.039431
8	4	9	0.578698	0.015075
9	4	8	0.577522	0.017476
10	8	10	0.873249	-0.03599
11	8	9	0.877127	-0.03271
12	8	8	0.871012	-0.03244
13	4	9	0.577462	0.016062
14	4	9.5	0.579107	0.015371
15	2	9	0.419248	0.032096
16	4	9	0.581159	0.017401
17	2	8.5	0.42118	0.031798
18	4	9	0.579618	0.013816
19	4	9	0.578146	0.014333
20	2	9.5	0.415272	0.028723
21	4	9	0.578349	0.013317
22	4	8.5	0.578935	0.013263
23	6	9.5	0.736362	-0.00871
24	6	9	0.734829	-0.00927
25	6	8.5	0.734524	-0.0089
26	4	9	0.571266	0.011979

APPENDIX E Wing-Tip-Propellers-Alone Mode Actual Text Matrix

Run Number	A-o-A	V(m/s)	L1 & R1	C _N	C _A
1	4	9	11500	0.623053	-0.05538
2	8	10	13000	0.934058	-0.11158
3	8	8	10000	0.93423	-0.0929
4	0	10	13000	0.279363	-0.03341
5	0	9	11500	0.274794	-0.02969
6	4	8	11500	0.631025	-0.09598
7	4	9	11500	0.612907	-0.05518
8	8	10	10000	0.891065	-0.04979
9	8	8	13000	0.94087	-0.19772
10	4	9	11500	0.605739	-0.05527
11	4	9	11500	0.599797	-0.0563
12	0	8	13000	0.277246	-0.11639
13	0	10	10000	0.248668	0.026765
14	4	9	11500	0.611355	-0.05421
15	4	10	11500	0.596003	-0.02915
16	4	9	11500	0.604289	-0.057
17	8	9	11500	0.911977	-0.11208
18	0	8	10000	0.248404	-0.02259
19	4	9	13000	0.610632	-0.09735
20	4	9	10000	0.5787	-0.01639
21	4	9	11500	0.599238	-0.05653
22	6	9.5	12250	0.764972	-0.08548
23	6	8.5	10750	0.759139	-0.07708
24	2	9.5	12250	0.426751	-0.04294
25	2	9	11500	0.429846	-0.03889
26	4	8.5	11500	0.610207	-0.07023
27	4	9	11500	0.600563	-0.05489
28	6	9.5	10750	0.748062	-0.04769
29	6	8.5	12250	0.780009	-0.11525
30	4	9	11500	0.598284	-0.05444
31	4	9	11500	0.605593	-0.05439
32	2	8.5	12250	0.443644	-0.07195
33	2	9.5	10750	0.416765	-0.006
34	4	9	11500	0.594774	-0.05659
35	4	9.5	11500	0.591937	-0.04044
36	4	9	11500	0.591076	-0.05598
37	6	9	11500	0.754342	-0.08327

Run Number	A-o-A	V(m/s)	L1 & R1	C _N	C _A
38	2	8.5	10750	0.418349	-0.03351
39	4	9	12250	0.600602	-0.07509
40	4	9	10750	0.591662	-0.03359

APPENDIX F Wing-Tip-Propellers-Alone and Two-Inboard-Propellers-Alone Mode Actual

Text Matrix

Run Number	A-o-A	C_N (L1&R1)	C_A (L1&R1)	C_N (L3&R3)	C_A (L3&R3)
1	2	0.44243	-0.04439	0.422858	-0.04356
2	4	0.608836	-0.06375	0.604334	-0.05725
3	6	0.768302	-0.08863	0.762772	-0.08127
4	8	0.9307	-0.11494	0.899144	-0.10819
5	2	0.446292	-0.04398	0.423123	-0.04235
6	4	0.613023	-0.06167	0.601034	-0.05553
7	6	0.777917	-0.08736	0.759695	-0.08045
8	8	0.928933	-0.1141	0.901081	-0.10987
9	2	0.445822	-0.04354	0.41496	-0.04369
10	4	0.609765	-0.06344	0.596909	-0.05613
11	6	0.776107	-0.08962	0.749228	-0.08236
12	8	0.924996	-0.11898	0.897639	-0.11134

Run Number	A-o-A	C_L (L1&R1)	C_D (L1&R1)	C_L (L3&R3)	C_D (L3&R3)
1	2	0.44213603	-0.0289224	0.42257748	-0.0287759
2	4	0.60715804	-0.0211245	0.60268871	-0.0149543
3	6	0.76331637	-0.007835	0.75788877	-0.0010934
4	8	0.91945265	0.01570699	0.88840853	0.01799956
5	2	0.4459957	-0.0283778	0.42284296	-0.0275574
6	4	0.61134009	-0.0187575	0.59940301	-0.0134687
7	6	0.77288071	-0.005567	0.75483882	-0.0005995
8	8	0.91772383	0.0162929	0.89028992	0.01660548
9	2	0.44552626	-0.0279545	0.41468465	-0.0291815
10	4	0.60808545	-0.0207504	0.59528736	-0.014355
11	6	0.77106158	-0.0080038	0.74442183	-0.0035932
12	8	0.91373683	0.01091247	0.88686079	0.01467076

APPENDIX G Wind Tunnel Data Boundary Corrections

Wing and body properties;

$$S_{ref} = 1.298 \text{ ft}^2 = 0.120 \text{ m}^2$$

$$\text{Wing volume} = 0.036 \text{ ft}^3 = 0.00101 \text{ m}^3$$

$$\text{Body volume} = 0.0668 \text{ ft}^3 = 0.00189 \text{ m}^3$$

$$C = 12 \text{ ft}^2 = 1.114 \text{ m}^2$$

Solid blockage correction;

$$\varepsilon_{sb,w} = \frac{K_1 \tau_1 (\text{wing volume})}{C^{3/2}} \quad (56)$$

$$\varepsilon_{sb,b} = \frac{K_3 \tau_1 (\text{body volume})}{C^{3/2}} \quad (57)$$

where K_1 is 0.98, K_3 is 0.93 and τ_1 is 0.84.

Wake blockage correction;

$$\varepsilon_{wb} = \frac{S_{ref}}{4C} C_{Du} \quad (58)$$

$$\varepsilon_T = \varepsilon_{sb} + \varepsilon_{wb} \quad (59)$$

$$q_c = q_A (1 + \varepsilon_T)^2 \quad (60)$$

$$V_c = V_A (1 + \varepsilon_T) \quad (61)$$

All-Propellers-On							
α	ε_{sb}	ε_{wb}	$1 + \varepsilon_T$	q_A (Pa)	q_c (Pa)	V_A (m/s)	V_c (m/s)
0	0.001968	-0.006842	0.995126	48.6	48.1274	8.9835	8.9398
4	0.001968	-0.006325	0.995643	48.5	48.0783	8.9743	8.9352
8	0.001968	-0.005305	0.996663	48.8	48.4749	9.0020	8.9720

Wing-Along							
α	ε_{sb}	ε_{wb}	$1 + \varepsilon_T$	q_A (Pa)	q_c (Pa)	V_A (m/s)	V_c (m/s)
0	0.001968	0.001027	1.002995	48.7	48.9921	8.9928	9.0197
4	0.001968	0.001568	1.003536	48.7	49.0450	8.9928	9.0246
8	0.001968	0.002406	1.004374	48.6	49.0261	8.9835	9.0228

$$\Delta C_{Dw} = \frac{K_1 \tau_1 (\text{wing volume})}{C^{3/2}} C_{Du} \quad (62)$$

$$\Delta C_{Db} = \frac{K_3 \tau_1 (\text{body volume})}{C^{3/2}} C_{Du} \quad (63)$$

Downwash and streamline curvature corrections;

$$\Delta \alpha_{sc} = \tau_2 \delta \left(\frac{S_{ref}}{C} \right) C_{Lw} \quad (64)$$

where τ_2 is 0.13 and δ is 0.125.

All-Propellers-On						
α	$\Delta \alpha$	α_c	C_{Du}	ΔC_{DT}	C_{Dc}	C_{Lw}
0	0.000467	0.000467	-0.2530	-0.00050	-0.2535	0.266
4	0.001184	4.001184	-0.2339	-0.00046	-0.2344	0.674
8	0.001894	8.001894	-0.1962	-0.00039	-0.1966	1.079

Wing-Along						
α	$\Delta \alpha$	α_c	C_{Du}	ΔC_{DT}	C_{Dc}	C_{Lw}
0	0.000428	0.000428	0.038	0.0000747	0.0381	0.244
4	0.001001	4.001001	0.058	0.0001142	0.0581	0.570
8	0.001529	8.001529	0.089	0.0001752	0.08918	0.870

VITA

Engin Baris
Mechanical and Aerospace Engineering Department
Norfolk, VA 23529

Engin Baris received his Bachelor's Degree in Mechanical Engineering from Sakarya University in 2012. His research interests include experimental aerodynamics and UAV design.